FACULDADE DE ENGENHARIA DA UNIVERSIDADE DO PORTO

Experimental investigation on the thermal performance of additively manufactured geometries

Catarina Silva Queirós Vieira

U.PORTO
FEUP FACULDADE DE ENGENHARIA UNIVERSIDADE DO PORTO

Master in Mechanical Engineering
Fluids & Energy

Supervisor: Prof. Abel Rouboa

Co-Supervisor: Dr. Mats Kinell

Co-Supervisor: Dr. Alessio Bonaldo

December 12, 2025

Experimental investigation on the thermal performance of additively manufactured geometries

Catarina Silva Queirós Vieira

Master in Mechanical Engineering
Fluids & Energy

December 12, 2025

Resumo

A crescente necessidade de melhorar a eficiência das turbinas a gás tem impulsionado o desenvolvimento de tecnologias de arrefecimento avançadas capazes de suportar temperaturas de entrada cada vez mais elevadas. A manufatura aditiva (AM) permite produzir geometrias internas altamente complexas, impossíveis de obter por métodos convencionais, criando novas oportunidades para otimizar o desempenho térmico de componentes. Contudo, a rugosidade superficial e as variações geométricas introduzidas pelo processo de Fusão Seletiva por Laser afetam significativamente a transferência de calor e as perdas de carga, tornando indispensável uma caracterização experimental rigorosa.

Este trabalho apresenta uma investigação experimental sobre o desempenho hidráulico e térmico de mini-canais fabricados por AM, utilizando ar como fluido de trabalho. Foi desenvolvida uma nova metodologia de avaliação para o rig quasi-Steady State Heat Transfer (qSSHT), superando limitações do método anteriormente utilizado e permitindo determinar, com maior precisão, coeficientes de transferência de calor, distribuições locais de HTC e fatores de fricção de Darcy em condições de convecção forçada. O estudo inclui o redesenho e validação do rig experimental, a definição de procedimentos de medição e o desenvolvimento de um solver numérico capaz de capturar variações axiais do HTC ao longo do canal.

Dois objetos de teste em aço inoxidável foram fabricados, caracterizados e testados. Os resultados mostram que a rugosidade típica da AM aumenta significativamente tanto o fator de fricção como o número de Nusselt em comparação com correlações de canais lisos. A análise local de transferência de calor evidencia efeitos de entrada acentuados, incluindo o *thermal-notch* associado a entradas a 90°, bem como a persistência de regimes em desenvolvimento devido à turbulência induzida pela rugosidade e à formação de escoamentos secundários. Os dados experimentais revelam tendências consistentes com a teoria e com correlações da literatura, validando o rig qSSHT redesenhado e a metodologia de avaliação implementada, e fornecendo um enquadramento robusto para a caracterização térmica de canais de arrefecimento fabricados por AM.

Abstract

The increasing demand for higher efficiency in gas turbines has driven the development of advanced cooling technologies capable of withstanding progressively higher turbine inlet temperatures. Additive manufacturing (AM) enables the production of highly complex internal geometries that cannot be fabricated using conventional methods, offering new opportunities to enhance the thermal performance of turbine components. However, the surface roughness and geometric deviations introduced by the Selective Laser Melting (SLM) process significantly affect heat-transfer behaviour and pressure losses, making rigorous experimental characterization essential.

This work presents an experimental investigation focused on the hydraulic and thermal performance of additively manufactured mini-channels using air as the working fluid. A new evaluation methodology for the quasi-Steady State Heat Transfer (qSSHT) rig was developed, addressing limitations of the previously used approach and enabling more accurate determination of heat-transfer coefficients, local HTC distributions, and Darcy friction factors under forced-convection conditions. The study includes the redesign and validation of the experimental rig, the definition of measurement procedures, and the development of a numerical solver capable of capturing axial HTC variations along the channel.

Two stainless-steel test objects (TOs) were manufactured, characterized, and tested. The results show that AM-induced surface roughness substantially increases both the friction factor and the Nusselt number when compared with smooth-channel correlations. Local heat-transfer analysis reveals strong entrance-region effects, including the *thermal-notch* behaviour associated with sharp 90° inlets, as well as the persistence of developing-flow regimes due to roughness-induced turbulence and secondary-flow structures. The experimental data exhibit trends consistent with theoretical expectations and literature correlations, validating both the redesigned qSSHT rig and the implemented evaluation methodology, and providing a robust framework for the thermal characterization of AM-manufactured cooling channels.

Acknowledgements

This thesis was carried out at the Fluid Dynamics Laboratory at Siemens Energy in Finspång, Sweden, as well as at the University of Porto, and I am very grateful to have had this opportunity.

I would like to thank my supervisor at Siemens Energy, Dr. Mats Kinell, for his tireless support throughout these months, and Dr. Alessio Bonaldo for giving me this opportunity. I also extend a special thank you to Dr. Karl Nogenmyr for all the support provided during the development of this work, especially regarding the numerical simulations.

To my friends in the lab who accompanied me throughout these months, Shruti, with whom I worked daily while developing the rig, Mihails, Giorgio, Aaron, Quentin and the new students joining the team, especially Alex, who is continuing my work, thank you. A special thanks to Jacob, who welcomed me into the lab and introduced me to the experimental procedures.

In Portugal, I would like to thank Professor Abel Rouboa for his support throughout these months and for making the connection between FEUP and Siemens Energy possible.

My sincere gratitude to my parents, Susana and Miguel, for their incredible support and encouragement throughout my entire education, for always pushing me to do my best, and for the amazing opportunities they have enabled me to pursue. To my brother, Diogo, thank you as well.

Finally, to my university friends who accompanied me during these long five years at FEUP, Teresa, Mia, Luísa, Filipa, Venâncio, and Ana, it would not have been the same, or even possible, without your support.

Catarina

"Above all, don't fear difficult moments. The best comes from them."

Rita Levi-Montalcini

Contents

List of Figures

List of Tables

List of Acronyms

1D	One-Dimensional
AM	Additive Manufacturing
CAD	Computer-Aided Design
CFD	Computational Fluid Dynamics
CHT	Conjugate Heat Transfer
D_h	Hydraulic Diameter
f_D	Darcy Friction Factor
Haynes 282	Haynes 282 Superalloy
HTC	Heat Transfer Coefficient
IN939	Inconel 939 Superalloy
Nu	Nusselt Number
PBF	Powder Bed Fusion
Pr	Prandtl Number
PT100	Platinum Resistance Temperature Sensor
qSSHT	quasi-Steady State Heat Transfer
Re	Reynolds Number
SLM	Selective Laser Melting
SLS	Selective Laser Sintering
SS	Stainless Steel
STAR-CCM+	Siemens STAR-CCM+
TO	Test Object

Chapter 1

Introduction

1.1 Motivation

Global energy consumption has more than doubled over the past four decades, driven mainly by population growth and improved living standards. Without significant advances in energy efficiency, both energy demand and consumption are expected to continue increasing steadily. At present, fossil fuels still account for more than 80% of the world's primary energy supply, resulting in substantial emissions of greenhouse gases and nitrogen oxides, with severe environmental impacts [1].

In response, and in line with the European Union's goal of reaching carbon neutrality by 2050, there is an urgent need to expand the role of renewable energy sources. However, despite rapid growth in the 21st century, renewables alone cannot yet support a fully decarbonised industrial system. Many renewable technologies are inherently non-dispatchable, meaning their power output cannot be adjusted on demand to meet grid requirements [2]. As a result, gas turbines remain among the most reliable and flexible power-generation technologies. They currently supply more than 20% of global electricity and play a vital role in stabilising electrical grids, as illustrated in Figure 1.1 [3].

Siemens Energy AB in Finspång manufactures a wide range of gas turbines and plays an important role in the ongoing energy transition. The company aims to provide reliable, efficient, and long-lasting power generation solutions by making turbines operate more effectively and making it simpler to use renewable energy sources. Figure 1.2 shows the SGT-750 industrial gas turbine, which is an example of the types of sophisticated equipment that have been made to make the energy system cleaner and more resilient.

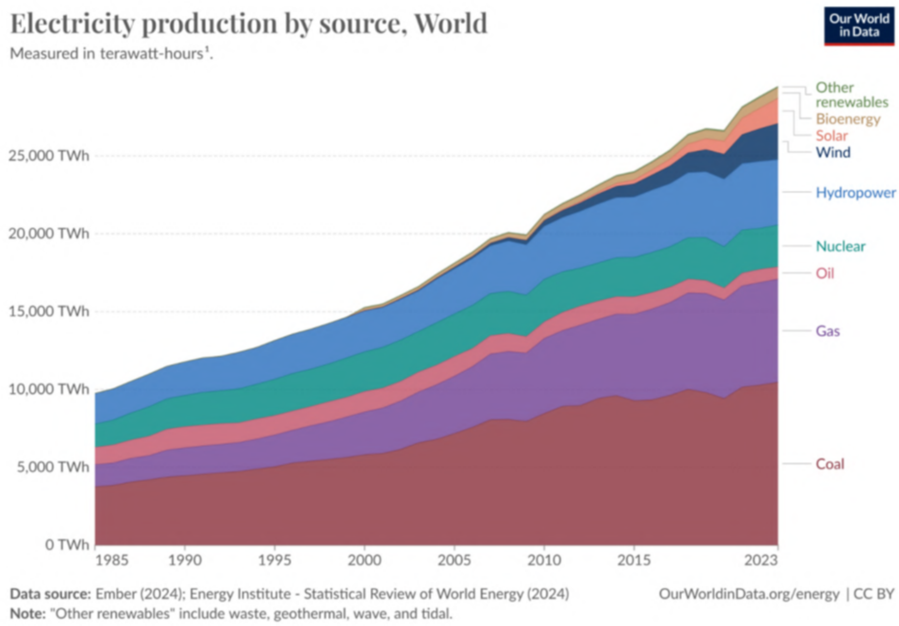

Figure 1.1: Global electricity consumption [3].

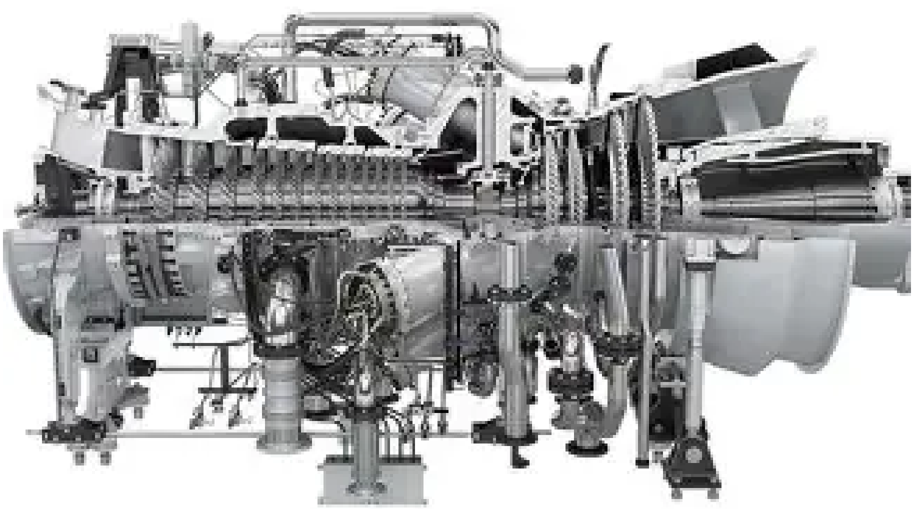

Figure 1.2: Siemens Energy SGT-750 industrial gas turbine [4].

1.2 Background

A gas turbine is an internal-combustion engine that converts chemical or thermal energy into mechanical power. It consists in three primary components: an upstream compressor, a combustor and a downstream turbine, as illustrated in Figure 1.3a. Gas turbines operate following the Brayton cycle, shown in Figure 1.3b. In an ideal Brayton cycle, the thermal efficiency depends strongly on the Turbine Inlet Temperature (TIT). For a fixed pressure ratio, higher TIT increases the net work output and therefore improves turbine efficiency.

subcaption

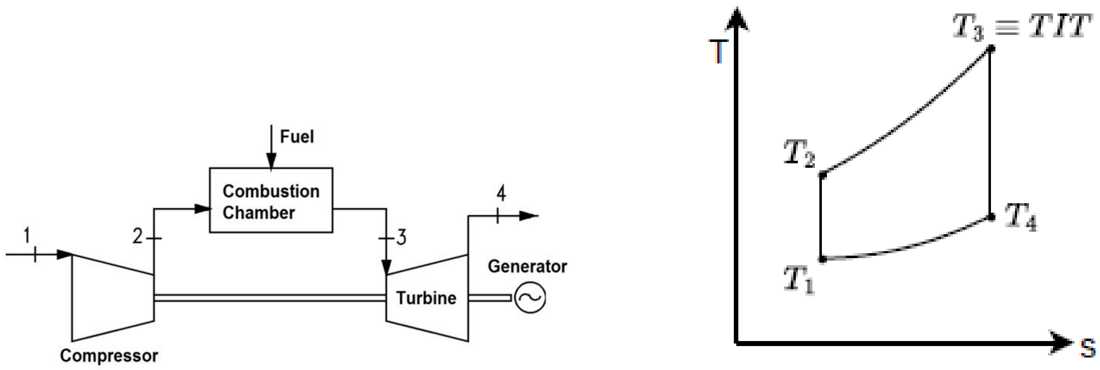

(a) Gas turbine scheme. (b) Ideal Brayton cycle.

Figure 1.3: Brayton cycle.

At high speeds, modern industrial gas turbines can reach TIT values of up to 1700 K. But the materials can't handle these high temperatures without advanced cooling systems [5]. Efficient use of cooling air is therefore crucial: providing excessive amounts of compressed air to cooling reduces power output, and higher cooling pressure increases compressor work. Thus, the development of advanced cooling techniques, especially in combination with innovative manufacturing technologies, has become a central research topic in turbine design [6].

Internal cooling performance can be improved by increasing effective surface area and promoting turbulence. Various cooling enhancements have been investigated, including rib turbulators, pin fins, dimples, surface protrusions, swirl chambers and roughened surfaces [7, 8]. Reducing the cross-sectional area of cooling channels can also enhance convective heat transfer. However, surface roughness, particularly that arising from manufacturing processes, may significantly affect the friction factor and heat-transfer coefficient [9]. As illustrated in Figure 1.4, modern gas turbine blades incorporate complex internal cooling systems to take advantage of these enhancement mechanisms.

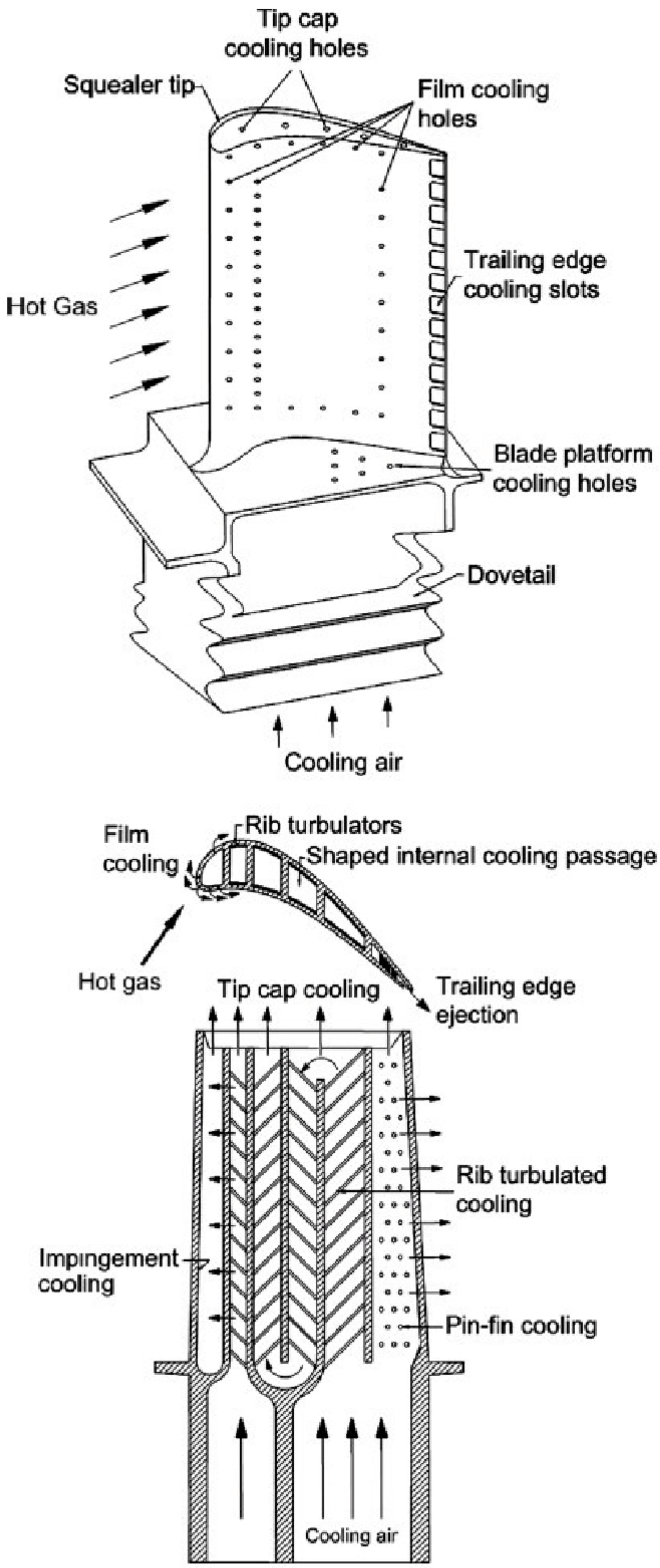

Figure 1.4: Internal cooling system of a modern gas turbine blade [10].

Additive manufacturing (AM) has enabled the development of complex cooling geometries previously impossible to fabricate with conventional methods. AM reduces geometric constraints, shortens production time and can lower manufacturing cost. However, sintering-based AM processes produce characteristic microstructures and porosity that may reduce mechanical strength. For this reason, AM components are most suitable for stationary or semi-stationary turbine components, such as guide vanes and combustor parts.

Moreover, the surface roughness inherent to AM processes has a decisive impact on pressure losses and heat-transfer performance in narrow cooling channels. Therefore, experimental studies using real AM materials and geometries are essential for understanding these effects [11].

1.3 Goals

The primary motivation for this work is the need to develop a reliable correlation capable of predicting both the convective heat-transfer coefficient and the Darcy friction factor for additively manufactured cooling channels used in Siemens Energy turbine components. The study evaluates the influence of AM-induced roughness on the thermal and hydraulic performance of mini-channels.

A major objective of the work is the development of a new evaluation methodology for the qSSHT rig when operating with air, overcoming the limitations of previous procedures and enabling accurate heat-transfer measurements under gaseous conditions.

1.4 Limitations

The main limitations of this work are the following:

- A new testing methodology had to be developed and validated for air, requiring substantial preparation time and limiting the number of test cases that could be completed.
- The total duration of the project was seven months, including a one-month overlap with the previous student. This limited the number of test objects (TOs) that could be manufactured, characterised and tested.
- The hydraulic diameter of each TO was estimated from microscope images of the inlet and outlet sections. This method does not capture internal geometric variations introduced by the SLM process.
- Only two test objects were evaluated experimentally, limiting the statistical robustness of the findings and the generality of the conclusions.
- The study is mainly experimental. No computational fluid dynamics (CFD) simulations were performed.

1.5 Methodology and Dissertation Structure

The methodology followed in this work is summarised in the schematic of Figure 1.5. As this is an experimental study, it requires repeated testing and continuous refinement of the test rig to ensure accuracy, stability, and reproducibility of the measurements.

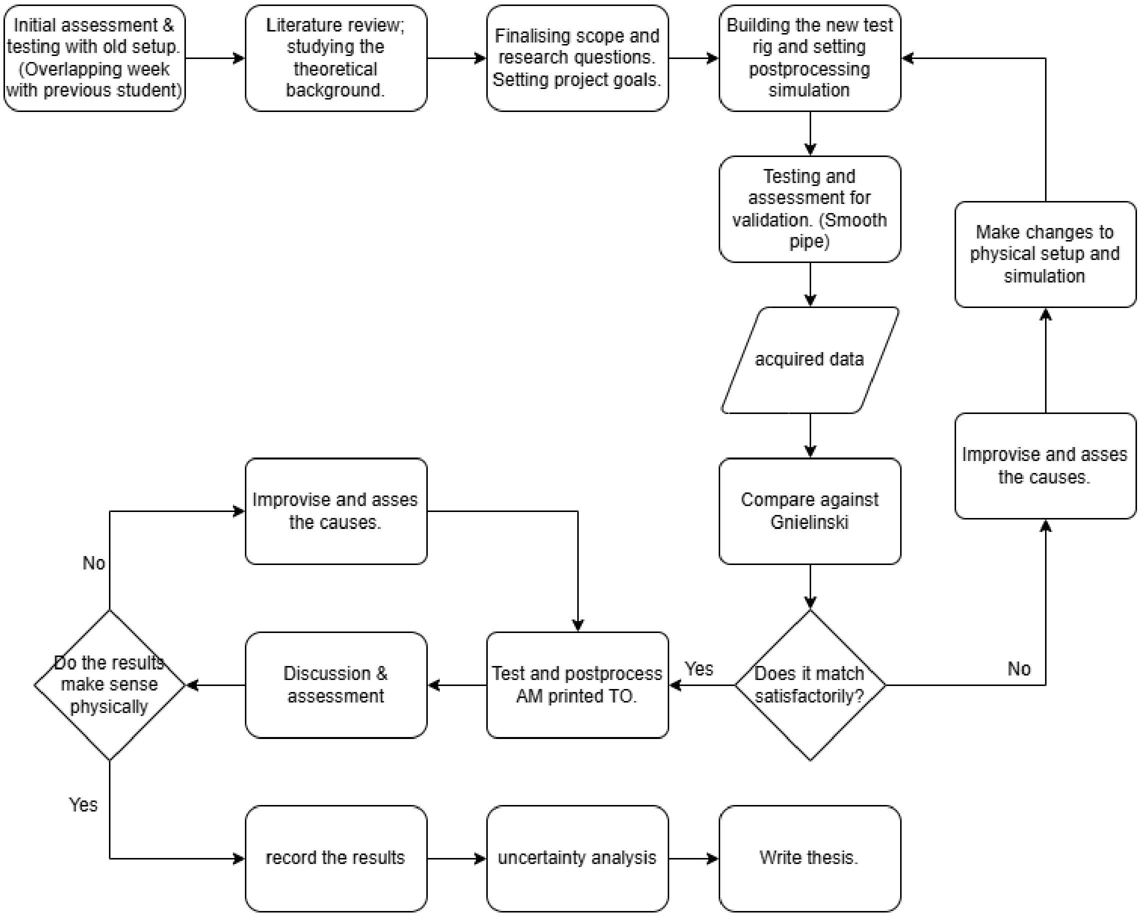

Figure 1.5: Methodology.

This dissertation is structured into three main stages. The first stage provides the theoretical background and state of the art relevant to the study, and introduces the existing qSSHT rig (see Chapters 2 and 3). The second stage describes the experimental methodology, including the design of the test rig, the measurement procedures, the execution of the friction-factor and heat-transfer tests, as well as the numerical framework (Chapters 4 and 5). Finally, the third stage presents the resulting analysis, comparing the experimental outcomes with theoretical models, followed by a sensitivity analysis (Chapters 6 and 7), and concludes with the key findings and recommendations for future work (Chapter 8).

Chapter 2

Theoretical Background

2.1 Fluid Mechanics

2.1.1 Flow Regime

The flow regime can be classified either by observing the behaviour of the flow streamlines or, more formally, through the dimensionless Reynolds number (Re). Depending on the balance between inertial and viscous forces, the flow may be laminar, transitional, or turbulent.

In a *laminar* flow regime, the fluid motion is highly organised and predictable, with smooth, parallel streamlines and negligible velocity fluctuations. This regime typically occurs at relatively low velocities or in flows dominated by viscous effects. In contrast, a *turbulent* flow regime is characterised by strong velocity fluctuations, three-dimensional mixing, and chaotic motion, and it generally appears at higher velocities where inertial forces dominate. [12]

The transition between laminar and turbulent flow is not abrupt; Instead, it happens over a transition region whose start and end depend on multiple factors. These include surface geometry, pressure gradients, surface temperature, free-stream turbulence, and surface roughness. Favourable pressure gradients and cooling of the walls tend to stabilize the boundary layer, which slows down the transition. On the other hand, surface roughness or disturbances can make the laminar boundary layer less stable and cause it to change to turbulence sooner. Such effects are particularly relevant for additively manufactured channels, where wall roughness is inherently higher and may induce premature turbulence development. [13]

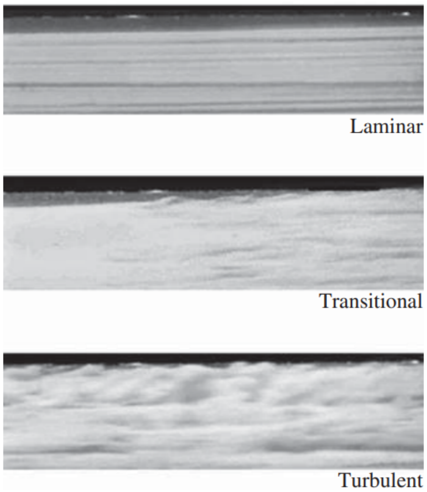

Figure 2.1: Laminar, transitional, and turbulent flows over a flat plate. [12]

2.1.2 Boundary Layer

The boundary layer is a thin region near a solid surface where viscous effects dominate over inertial forces.

Prandtl first came up with this idea in 1904, and it is essential for understanding how to assess both frictional losses and heat transfer in internal flows. The no-slip and no-temperature-jump conditions at the wall cause strong velocity and temperature gradients inside the boundary layer [14].

Outside the boundary layer, viscosity effects become negligible, and the velocity gradients normal to the flow are relatively small [15]. Given that friction and heat transfer occur primarily inside the boundary layer—and that the present thesis investigates how surface roughness affects both—understanding boundary-layer behaviour is essential.

2.1.2.1 Velocity Boundary Layer

When a fluid flows over a solid surface, viscous effects impose the no-slip condition, forcing the fluid velocity at the wall to be zero, i.e. at $y = 0$, $u = 0$. As the fluid moves away from the wall, viscous influence weakens, and the velocity gradually increases until it approaches the free-stream value u_e. The region in which viscous effects remain significant and prevent the velocity from reaching u_e is defined as the *velocity boundary layer* [16].

The boundary-layer thickness, δ, is commonly defined as the distance from the wall at which the velocity reaches 99% of the free-stream velocity:

$$\delta = y \quad \text{such that} \quad u = 0.99\,u_e. \tag{2.1}$$

At the wall, the steep velocity gradient generates a non-zero shear stress. For Newtonian fluids, the wall shear stress is given by:

$$\tau_w = \mu \left(\frac{\partial u}{\partial y} \right)_w, \tag{2.2}$$

representing the transfer of momentum from the moving fluid to the stationary surface.

As shown in Figure 2.2, the velocity boundary layer thickens along the flow direction x as viscous diffusion propagates into the fluid. In laminar flow, this growth is smooth and orderly, while in turbulent flow the enhanced mixing produces a fuller velocity profile and a much thinner viscous sublayer. The development of the velocity boundary layer strongly influences frictional losses, pressure drop, and overall channel performance [17].

2.1.3 Thermal Boundary Layer

The thermal boundary layer develops simultaneously with the velocity boundary layer, but its growth depends on thermal—rather than momentum—diffusion. At the wall, the fluid temperature immediately assumes the wall temperature due to the no-temperature-jump condition, $T(x,0) = T_w$. Moving away from the wall, the temperature gradually approaches the free-stream temperature T_e.

The thermal boundary-layer thickness, δ_T, is defined as the distance from the wall at which the fluid temperature reaches 99% of the free-stream value:

$$\delta_T = y \quad \text{such that} \quad T = 0.99\,T_e. \tag{2.3}$$

The temperature gradient at the wall generates heat flux according to Fourier's law:

$$\dot{q}_w = -k\left(\frac{\partial T}{\partial y}\right)_w. \tag{2.4}$$

The relative thickness of the thermal and velocity boundary layers depends on the Prandtl number, $Pr = \nu/\alpha$. For $Pr < 1$, as in the case of gases such as air, thermal diffusion is faster than momentum diffusion, leading to a thicker thermal boundary layer. Conversely, for $Pr > 1$ (e.g. oils), thermal diffusion is slower, and $\delta_T < \delta$.

Figure 2.2 illustrates the classical development of velocity and thermal boundary layers in an external flow over a flat plate. In this configuration, the fluid approaches the surface with uniform velocity and temperature, and the boundary layers grow only from one side. This simplified representation is fundamental for introducing boundary-layer concepts and forms the basis for understanding the more complex internal-flow behaviour.

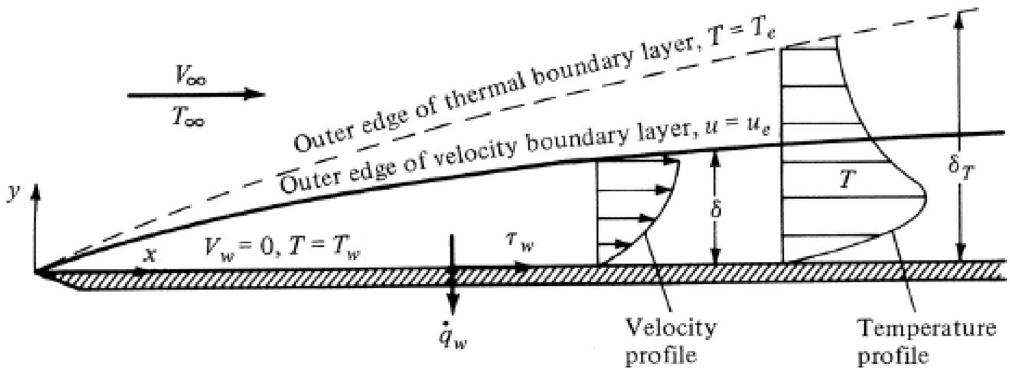

Figure 2.2: Development of the velocity and thermal boundary layers over a flat plate (external flow) [17].

2.1.4 Reynolds Number and Flow Development

The Reynolds number is one of the most important dimensionless groups in fluid mechanics, characterizing the balance between inertial and viscous forces in an internal flow. It governs not only the transition between laminar and turbulent regimes, but also the manner in which velocity profiles and boundary layers evolve along the channel length. According to White [18], the Reynolds number for internal flows is defined as:

$$\mathrm{Re} = \frac{\rho V L}{\mu} = \frac{V L}{\nu}, \tag{2.5}$$

where V is the mean flow velocity, L a characteristic length scale (typically the hydraulic diameter in ducts), and μ and ν are the dynamic and kinematic viscosities, respectively.

When a uniform flow enters a duct, the velocity field undergoes a development process driven by the growth of the hydrodynamic boundary layer along the channel walls. Initially, the velocity profile is uniform, but viscous diffusion gradually thickens the boundary layer until it occupies the entire cross-section. The axial distance required for this to occur is known as the hydrodynamic entry length, $x_{fd,h}$. As discussed by White [18], this entry length is strongly dependent on the flow regime: it is proportional to the Reynolds number in laminar flow, whereas in turbulent flow it is significantly shorter and only weakly dependent on Reynolds number.

Figure 2.3 shows the simultaneous hydrodynamic and thermal development inside an internal duct, which is directly relevant to the mini-channels investigated in this work. In internal flows, boundary layers grow from all walls and eventually merge at the duct centreline. This creates a pronounced entrance region, where both the friction factor and the heat-transfer coefficient vary strongly with axial position. Only after the complete merging of the boundary layers does the flow reach the fully developed regime. Understanding this evolution is essential for interpreting the friction-factor and heat-transfer behaviour of additively manufactured channels, where roughness and geometric deviations can significantly delay boundary-layer growth.

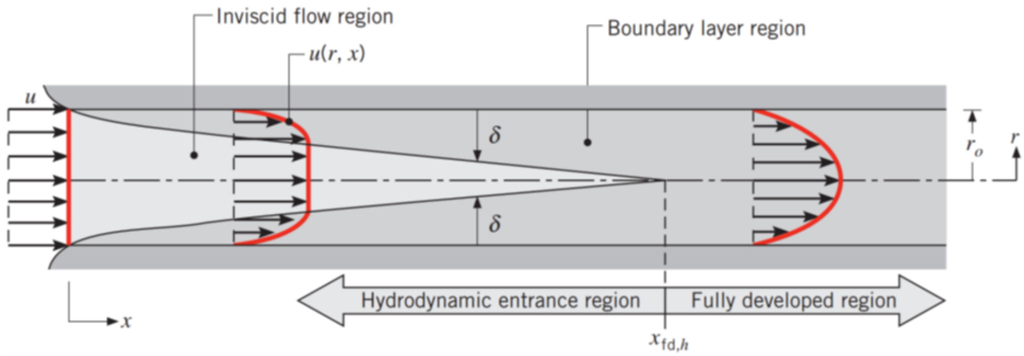

Figure 2.3: Hydrodynamic and thermal development inside an internal duct (internal flow). Adapted from [19].

For laminar flow, the hydrodynamic entry length can be estimated using Eq. 2.13. For turbulent flow, the entry region is much shorter, and a fully developed regime is typically reached after a distance of approximately 10 hydraulic diameters, Eq. 2.7.

$$\left(\frac{x_{fd,h}}{D_h}\right)_{\text{lam}} \approx 0.05\,\text{Re} \tag{2.6}$$

$$\left(\frac{x_{fd,h}}{D_h}\right)_{\text{turb}} > 10 \tag{2.7}$$

2.1.5 Entrance Effects

When a uniform flow enters a duct, both the hydrodynamic and thermal boundary layers begin to develop from the inlet, creating a region in which the velocity and temperature profiles vary significantly with the axial position. This region is known as the *entrance region*. Only after the boundary layers completely merge at the duct centreline does the flow reach its fully developed state. As you move through the hydrodynamic entrance region, the velocity profile changes from a uniform inlet distribution to a parabolic (laminar) or fuller (turbulent) shape. The wall shear stress is higher during this process than it is in the fully developed regime. This causes higher friction factors as well as increased pressure losses [12]. This effect is especially relevant in short channels, where the entrance region may occupy a significant fraction of the total duct length.

A similar phenomenon occurs for the thermal field. When the wall temperature differs from the bulk fluid temperature, the thermal boundary layer begins to grow at the inlet, resulting in a heat-transfer coefficient that is substantially higher than the asymptotic fully developed value. As the thermal boundary layer thickens along the duct, the local heat-transfer coefficient decreases until it eventually reaches the fully developed regime.

Although entrance effects in conventional smooth circular tubes are typically confined to a relatively short portion of the duct, their influence becomes more pronounced in mini-channels and non-circular passages. In additively manufactured channels, the combination of surface roughness, geometric deviations and secondary flows can further delay the merging of the boundary layers, extending the entrance region considerably and increasing both friction and heat transfer beyond the classical correlations for smooth ducts.

Understanding these entrance-region characteristics is essential for the analysis of the present experimental work, as the short additively manufactured channels under investigation may not reach fully developed hydrodynamic or thermal conditions over their entire length [20, 21].

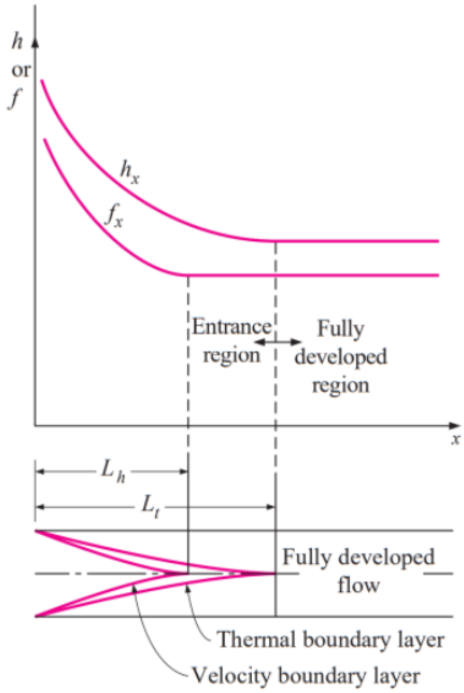

Figure 2.4: Variation of the friction factor and the convection heat transfer coefficient (Pr>1) [22].

2.1.6 Pressure Losses

The analysis conducted in this work considers only contraction and expansion pressure losses, as well as frictional pressure losses. Other losses—typically small—originating from fittings, connectors, valves or hoses were neglected, since their contribution is insignificant compared to the dominant mechanisms under investigation.

2.1.6.1 Contraction and Expansion Pressure Losses

Sudden changes in cross-sectional area inside a channel, particularly in pipes with sharp 90-degree edges, generate localized pressure losses. These losses can be estimated using correlations for sudden contractions and sudden expansions, as documented in Idelchik's *Handbook of Hydraulic Resistance* [23].

For a sudden contraction, illustrated in Figure 2.5, the loss coefficient depends on F_0, F_1, the cross-sectional area ratio and the Reynolds number. The following correlations are valid in the range $10 \leq Re \leq 10\,000$:

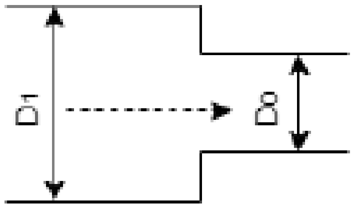

Figure 2.5: Sudden contraction in a pipe.

$$\zeta_{\text{loc}} = A \cdot B \left(1 - \frac{F_0}{F_1}\right) \tag{2.8}$$

$$A = \sum_{i=0}^{7} a_i \, (\log Re)^i \tag{2.9}$$

$$B = \sum_{i=0}^{2} \left[\left(\sum_{j=0}^{2} a_{ij} \left(\frac{F_0}{F_1}\right)^j \right) (\log Re)^i \right] \tag{2.10}$$

The coefficients a_i and a_{ij} are defined as:

$a_0 = -25.12458,\quad a_1 = 118.5076,\quad a_2 = -170.4147,\quad a_3 = 118.1949,$

$a_4 = -44.4214,\quad a_5 = 9.09524,\quad a_6 = -0.9244027,\quad a_7 = 0.03408265.$

For a sudden expansion, illustrated in Figure 2.6, the loss coefficient is likewise a function of F_0, F_1 and the Reynolds number, as expressed by:

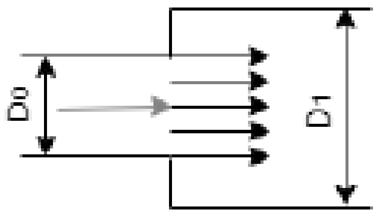

Figure 2.6: Sudden expansion in a pipe.

$$\begin{aligned}\zeta_{\text{loc}} = & -8.44556 - 26.163\left(1-\frac{F_0}{F_1}\right)^2 - 5.38086\left(1-\frac{F_0}{F_1}\right)^4 \\ & + \log Re\left[6.007 + 18.5372\left(1-\frac{F_0}{F_1}\right)^2 + 3.9978\left(1-\frac{F_0}{F_1}\right)^4\right] \\ & + (\log Re)^2\left[-1.02318 - 3.091691\left(1-\frac{F_0}{F_1}\right)^2 - 0.680943\left(1-\frac{F_0}{F_1}\right)^4\right].\end{aligned} \tag{2.11}$$

2.1.6.2 Friction Pressure Loss

Pressure losses due to wall friction in internal flows—both laminar and turbulent—are described by the general Darcy–Weisbach equation [24]:

$$\Delta p = f_D \frac{L}{D_h}\frac{\rho u^2}{2} \tag{2.12}$$

The hydraulic diameter is defined as $D_h = 4A/P$, where A is the cross-sectional area and P the wetted perimeter.

For fully developed laminar flow in circular channels, the friction factor is given by Eq. 2.13, depending solely on the Reynolds number and not influenced by surface roughness. In fully developed turbulent flow, the Darcy friction factor is determined by the Colebrook–White equation [25], which incorporates the relative roughness ε/D_h:

$$f_D = \frac{64}{Re} \tag{2.13}$$

$$\frac{1}{\sqrt{f_D}} = -2\log_{10}\left(\frac{\varepsilon}{3.7D_h} + \frac{2.51}{Re\sqrt{f_D}}\right) \tag{2.14}$$

The Moody chart, shown in Figure 2.7, presents the Darcy friction factor for channels with varying Reynolds numbers and relative roughness. It combines the laminar-flow relationship, the Colebrook–White equation and experimental data, providing a practical tool for estimating the friction factor in both smooth and rough pipes.

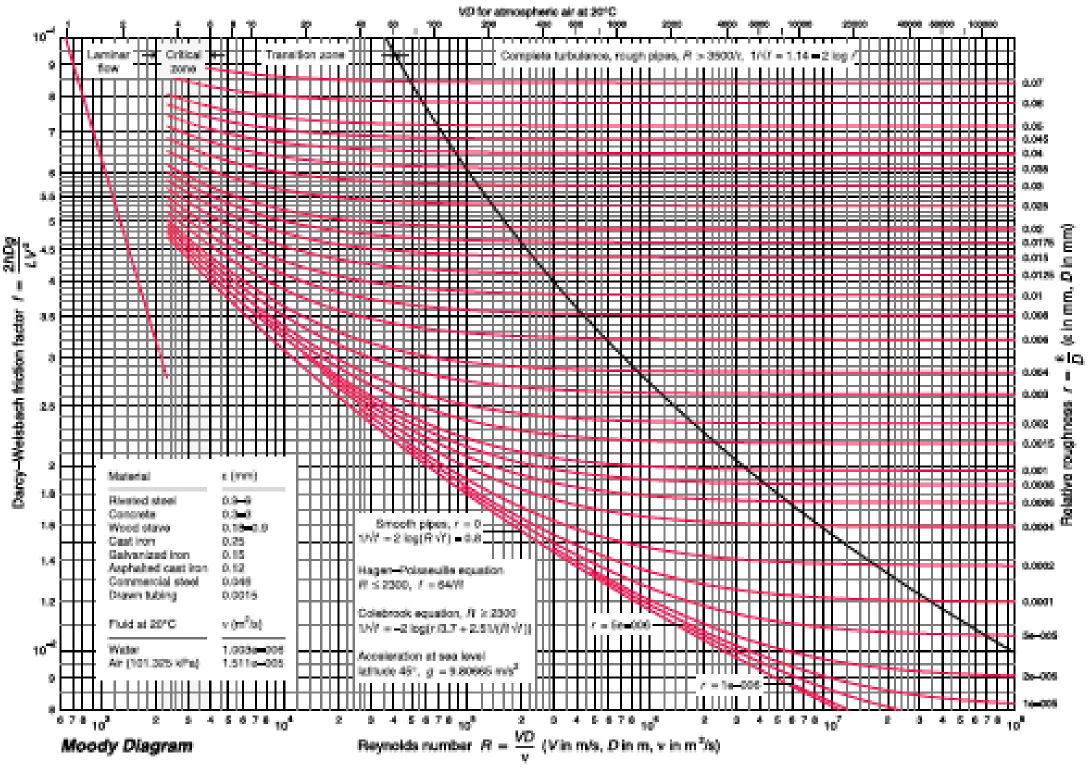

Figure 2.7: Moody chart [26].

2.1.7 The Thermal Notch Effect

The heat-transfer behaviour near the inlet of a duct is strongly influenced by the local geometry. When a fluid enters a sharp-edged or sudden-contraction inlet, the hydrodynamic and thermal boundary layers are reset to zero thickness, producing a very steep temperature gradient at the wall. This generates a pronounced local amplification of the heat-transfer coefficient known as the *thermal-notch effect*. As first documented by Mills [27], this effect arises because the incoming fluid undergoes a rapid geometric contraction (vena contracta), which increases local velocity gradients, enhances wall shear stress, and produces a large, short-lived peak in the heat-transfer coefficient before the flow enters the classical thermal entrance region.

Figure 2.8 illustrates this behaviour: for all Reynolds numbers, the heat-transfer coefficient exhibits a strong maximum around $x/D \approx 0.5$–1.0, followed by a monotonic decay as the thermal boundary layer grows downstream. Notably, the magnitude of this peak increases with Reynolds number because higher inertial forces delay boundary-layer thickening and prolong the developing-flow region.

It is important to distinguish the thermal-notch effect from the conventional thermal entrance region mentioned in Section 2.1.5. In the entrance region, the heat-transfer coefficient is elevated because the thermal boundary layer has not yet reached its asymptotic fully developed thickness. The thermal notch, however, is specifically caused by the sharp inlet geometry and occurs *before* the onset of the classical entrance regime. Mills showed that the notch behaviour is superimposed on the entrance-region development, producing a characteristic spike in heat transfer that can be several times larger than the fully developed value.

The rig used in this work features a 90° sharp inlet edge, which inherently generates the type of notch behaviour described by Mills. This effect is especially relevant for short test objects, where the thermal-notch region may represent a substantial fraction of the total heated length and must therefore be accounted for in the interpretation of Nusselt number data.

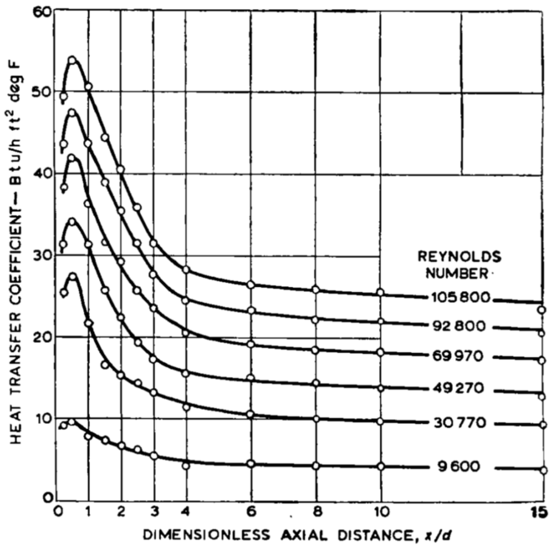

Figure 2.8: Local heat-transfer coefficients for a 90° sharp-edged inlet [27].

2.2 Heat Transfer

Heat transfer occurs whenever a temperature gradient exists, either within a material or between different media. There are three fundamental modes of heat transfer: conduction, convection and radiation. Conduction is the transfer of energy through a medium that doesn't move. Convection happens when a fluid moves and comes into contact with a surface that is at a different temperature. Radiation is the release of heat in the form of electromagnetic waves, which don't need a physical medium [19].

In the present work, thermal radiation is considered negligible due to the relatively small temperature differences involved and the low emissivity of metallic surfaces. Therefore, only conduction and convection are discussed in the following subsections.

2.2.1 Conduction

Conduction arises when a temperature gradient exists within a solid or a stationary fluid. This mechanism is driven by molecular agitation: high-energy molecules in warmer regions transfer energy to neighbouring lower-energy molecules through collisions. As a result, heat always flows in the direction of decreasing temperature [19].

This behaviour is described mathematically by Fourier's law, Eq. 2.15:

$$Q = -kA\frac{dT}{dx} \tag{2.15}$$

where k is the thermal conductivity of the material. The negative sign indicates that heat flows from regions of higher to lower temperature.

2.2.2 Convection

Convection heat transfer results from the combined effect of random molecular motion (as in conduction) and bulk fluid motion. It occurs whenever a moving fluid interacts with a bounding surface at a different temperature. The convective heat flux is expressed using Newton's law of cooling, Eq. 2.16:

$$Q = hA\Delta T = hA(T_\infty - T_{\text{wall}}) \tag{2.16}$$

where h is the convection heat transfer coefficient. A positive heat flux corresponds to heat transfer from the wall to the fluid ($T_{\text{wall}} > T_\infty$), while a negative flux indicates heat transfer from the fluid to the surface [19].

Convection may occur as:

- *forced convection*, when the fluid motion is induced by external means (e.g., a pump),
- *natural convection*, when motion is driven by buoyancy forces caused by density variations.

2.2.3 Nusselt Number

According to White [18], the Nusselt number is the dimensionless representation of the convection heat transfer coefficient. It is defined as the ratio of convective to conductive heat transfer under identical thermal conditions. For internal flows it is given by:

$$Nu = \frac{hL}{k} \tag{2.17}$$

It quantifies how effectively convection enhances heat transfer relative to pure thermal conduction and is generally expressed as a function of the Reynolds and Prandtl numbers.

2.2.4 Heat Transfer Correlations

Determining the heat transfer coefficient h directly is often difficult; therefore, empirical correlations are widely used to estimate the Nusselt number in internal flows.

For fully developed laminar flow in circular tubes, surface roughness effects are negligible, and the Nusselt number becomes constant. For constant wall temperature, $Nu = 3.66$, while for constant heat flux, $Nu = 4.36$ [19].

Turbulent flows are more complex and require empirical correlations. The widely used Dittus–Boelter correlation applies to smooth channels with small-to-moderate wall-to-fluid temperature differences with an accuracy of 20%:

$$Nu = 0.023 Re^{4/5} Pr^{0.4} \tag{2.18}$$

valid for:

$$\begin{cases} 0.7 \le Pr \le 160, \\ Re \ge 10^4, \\ L/D_h \ge 10. \end{cases}$$

To improve accuracy and cover part of the transitional regime, the Gnielinski correlation is commonly used. It incorporates the friction factor (typically obtained from the Moody diagram) and reduces the prediction error to below 20% [19]:

$$Nu = \frac{\left(\frac{f_D}{8}\right)(Re - 1000)Pr}{1 + 12.7\left(\frac{f_D}{8}\right)^{1/2}(Pr^{2/3} - 1)} \quad \text{for} \quad \begin{cases} 0.5 \le Pr \le 2000, \\ 3 \cdot 10^3 \le Re \le 5 \cdot 10^6. \end{cases} \tag{2.19}$$

For short channels (low L/D_h), entrance effects become significant due to flow acceleration at the inlet (vena contracta) and thermal boundary-layer development. Mills proposed a correction for the entrance region in smooth channels, comparing the local Nusselt number Nu_x to the fully developed value Nu_∞ [27]:

$$\frac{Nu_x}{Nu_\infty} = 1 + \frac{8.7}{L/D_h + 5}. \tag{2.20}$$

2.2.5 Flow Properties

The following thermodynamic relations were used to compute air properties in this work.

Assuming air behaves as an ideal gas:

$$p = \rho RT, \qquad R = 287.05\, J/kgK \tag{2.21}$$

The air dynamic viscosity is evaluated using Sutherland's law [28]:

$$\frac{\mu}{\mu_0} = \left(\frac{T}{T_0}\right)^{3/2} \frac{T_0 + S_\mu}{T + S_\mu} \tag{2.22}$$

where $\mu_0 = 1.716 \times 10^{-5}\,\mathrm{N{\cdot}s/m^2}$, $T_0 = 273.15\,\mathrm{K}$, and $S_\mu = 110.56\,\mathrm{K}$.

The Prandtl number is:

$$\mathrm{Pr} = \frac{\mu c_p}{k}, \tag{2.23}$$

and in the present work a constant value $Pr = 0.71$ is used due to the limited temperature range of the experiments [19].

The thermal conductivity of air is computed using the modified Eucken equation [29]:

$$k_{\text{air}} = \mu c_v \left(1.32 + \frac{1.77R}{c_v}\right), \qquad c_v = 720\,\text{J/(kg·K)} \tag{2.24}$$

2.3 Additive Manufacturing

Additive Manufacturing (AM) is a process in which components are produced directly from three-dimensional computer models through the layer-by-layer deposition of material. This contrasts sharply with traditional subtractive manufacturing methods such as casting or machining, where components are shaped by removing material from a solid block.

AM processes do not require dedicated tooling to fabricate a part. Instead, by building components in successive layers, AM enables the production of highly complex geometries and significantly facilitates rapid prototyping.

Although AM was initially developed for prototyping, it is rapidly expanding and transforming manufacturing practices across multiple sectors, including aerospace, automotive, product development, and biomedical engineering [30, 31].

Many different kinds of technologies, materials, and processing strategies fall under the general term of additive manufacturing. To choose the best solution for a specific application, it is necessary to know the pros and cons of each technique. This is considering that different applications have different needs, such as material compatibility, resolution, mechanical performance, cost, and production speed. The main AM processes are summarised in Figure 2.9.

In the present work, the manufactured test objects were produced using a selective laser melting/sintering (SLM/SLS) technique, with different materials and machines as detailed below.

2.3.1 Powder Bed Fusion

Selective Laser Melting (SLM) and Selective Laser Sintering (SLS) belong to the Powder Bed Fusion (PBF) family of AM processes. In these techniques, a thin layer of powder is spread across the build platform, and a laser selectively melts (SLM) or sinters (SLS) the material according to the cross-section of the digital model. After each layer is processed, a new layer of powder is deposited and the process repeats until the full component is formed. The general concept of SLM is shown in Figure 2.10.

Powder Bed Fusion presents limitations in surface roughness and fatigue strength when compared to machined parts. The quality of the surface of additively manufactured parts is greatly affected by the accumulation of heat during the build process. This can cause the surrounding powder to partially melt, which can make unwanted particles stick to the surface [33].

This happens for several reasons related to the process. The placement of the part on the build platform is important because parts that are too close together may transfer heat through

Process	Acronyms	Feedstock	Material	Bonding and join
Extrusion (or fused filament fabrication or fused deposition modeling)	FFF, FDM	Filament, rod, pellets	Polymer	Fused with heat
Photopolymerization (or stereolithography)	SLA	Liquid	Photopolymer, metal, ceramics, composite	Cured with laser, projector, UV light
Material Jetting (or Binder Jetting)	MJ (BJ)	Powder, liquid	Ceramic, wax, polymer, metal, sand	Cured with UV light, heat
Laminated Object Manufacturing (or Sheet Lamination)	LOM	Sheet	Paper, metal, polymer	Joined with agent, heat and pressure
Selective Laser Melting	SLM	Powder	Metal	Fused with laser and electron beam
Directed Energy Deposition	DED, EBM	Wire, powder	Metal	Fused with laser and electron beam

Figure 2.9: Additive manufacturing processes [31].

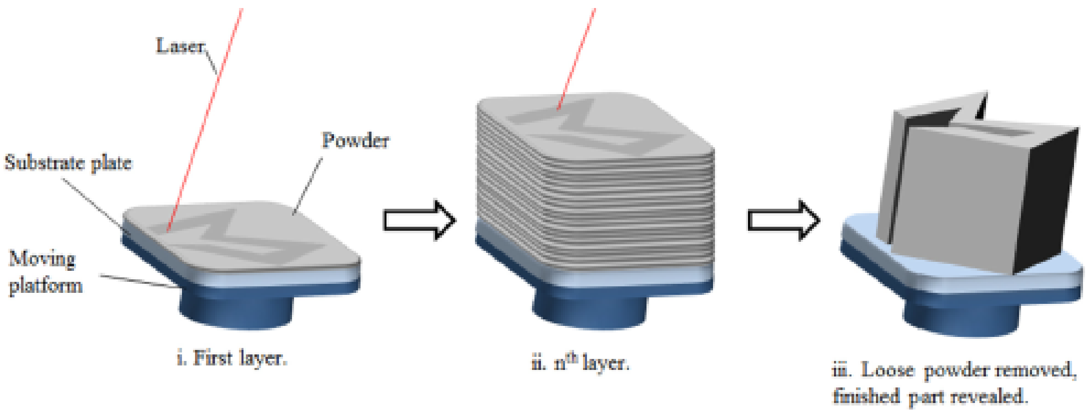

Figure 2.10: Concept of the SLM process [32].

the powder around them, which could cause local overheating and block small features like cooling channels. The angle of the surface in relation to the build plate also affects roughness since different angles cause different amounts of layer overlap.

Likewise, the printing direction (upskin vs. downskin) influences surface quality: downskin surfaces usually exhibit poorer quality because heat tends to accumulate in the thinner underlying layer, leading to local overheating and enhanced powder adhesion [32].

The uniformity of the powder layer is another important factor. Irregular powder spreading by the recoater (wiper blade or roller) can create heterogeneous regions with local variations in roughness. Finally, the direction of the inert gas flow (typically argon) affects the deposition of spatter and oxide particles. Surfaces located on the downstream side of the gas flow tend to accumulate redeposited material and therefore exhibit higher roughness [34].

2.4 Surface Roughness

Surface roughness quantifies the deviation of a real surface from its ideal or nominal geometry, expressed through the presence of microscopic peaks and valleys. The roughness pattern depends strongly on the manufacturing process used and can be evaluated using a 2D contact profilometer, as illustrated in Figure 2.11, or through more advanced 3D optical scanning techniques.

The surface profile is commonly characterised using statistical parameters defined in ISO 4287 [35]. The most frequently used parameters are summarised in Table 2.1. Among these, the arithmetic average roughness (R_a) is the most widely adopted descriptor for general applications. However, the mean roughness depth (R_z) is more comparable to the parameter employed by Nikuradse in his classical investigation of flow in rough pipes [36]. For this reason, R_z is used in the present work as the primary roughness evaluation metric.

Table 2.1: Surface roughness parameter definitions according to ISO 4287 [37]

Parameter	Formula	Definition
R_a	$R_a = \frac{1}{L}\int_0^L \lvert z(x)\rvert\, dx$	Arithmetic average roughness; arithmetic mean of profile height deviations from the mean line.
R_v	$R_v = \frac{1}{n}\sum_{i=1}^{n} \min_x(z)$	Mean roughness valley; average of the maximum valley depths below the mean line.
R_p	$R_p = \frac{1}{n}\sum_{i=1}^{n} \max_x(z)$	Mean roughness peak; average of the maximum peak heights above the mean line.
R_z	$R_z = R_v + R_p$	Mean roughness depth; average value of single roughness depths of five individual measuring lengths in sequence.

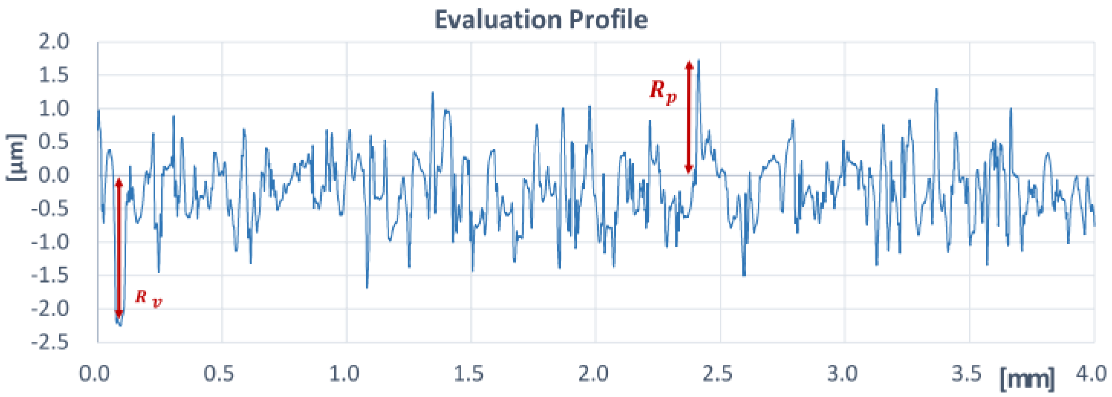

Figure 2.11: Rough profile evaluation for the aluminum sample [38].

2.5 Joule Heating

Joule heating, also known as resistive or ohmic heating, is the physical effect by which an electric current flowing through a conductor is converted into thermal energy. This energy manifests as a temperature rise within the material, hence the term "heating" [39].

In the metallic test object (TO) used in this work, heat generation results directly from the Joule effect, where electrical energy is transformed into heat. The electrical power supplied to the conductor is given by:

$$P_{el} = VI \tag{2.25}$$

Voltage and current are related by Ohm's law:

$$V = RI \tag{2.26}$$

and combining these two expressions yields the well-known relation for instantaneous power dissipation in a resistive element:

$$P = I^2 R \tag{2.27}$$

The total thermal energy generated in the conductor during a time interval t is:

$$Q = Pt \tag{2.28}$$

Assuming spatially uniform material properties and negligible heat losses, the resulting temperature rise can be estimated as:

$$T = \frac{Q}{cm} \tag{2.29}$$

where c is the specific heat of the material and m is the mass of the conductor.

In the test rig employed in this study, the circuit is voltage-regulated. Under such conditions, the total electrical power supplied can be rewritten using Ohm's law as:

$$P_{el} = \frac{V^2}{R} \tag{2.30}$$

The power supply in the experimental setup delivers alternating current (AC). Under AC excitation, the previous expressions represent instantaneous quantities, and the relation $Q = Pt$ cannot be directly applied to determine accumulated heat. To obtain meaningful time-averaged thermal quantities, the *root-mean-square* (RMS) values of voltage and current must be used. The average electrical power dissipated over one AC cycle in a purely resistive load is therefore:

$$P_{\text{avg}} = \frac{V_{\text{rms}}^2}{R}. \tag{2.31}$$

2.6 Uncertainty Analysis

Given the experimental nature of this work, all measured variables are subject to inaccuracies. Systematic errors remain relatively constant or vary in a predictable manner and can therefore be reduced through proper calibration of the measurement instruments. In contrast, random errors are associated with unknown or uncontrollable factors and may fluctuate unpredictably, meaning they cannot be eliminated but only minimized through repeated measurements and good experimental practice, as illustrated in Figure 2.12 [40].

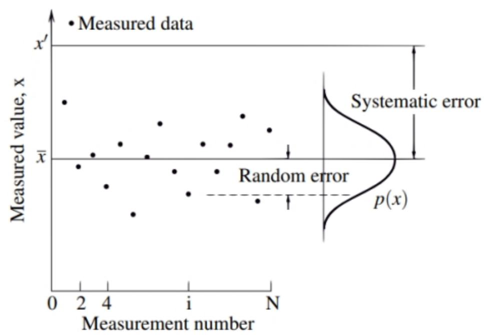

Figure 2.12: Types of errors accounted for in the uncertainty analysis.

Within the context of a single measured variable, both types of uncertainty propagate through the data-reduction equation (DRE) and contribute to the uncertainty of the final result. Experimental results are therefore reported with a combined standard uncertainty, computed using Taylor-series uncertainty propagation [41]. For a result $Y = f(X_1, \ldots, X_n)$ with independent, normally distributed input variables, the combined uncertainty is given by:

$$u^2(Y) = \sum_{i=1}^{n} \left(\frac{\partial Y}{\partial X_i} u(X_i) \right)^2, \tag{2.32}$$

Where $u(X_i)$ is the standard uncertainty associated with input variable X_i, typically obtained from calibration certificates or manufacturer specifications.

To express uncertainty with a specified confidence level, the combined standard uncertainty is multiplied by a *coverage factor* k, yielding the expanded uncertainty U_Y. For a 95% confidence level and normally distributed data, $k \approx 2$:

$$U_Y = k \cdot u(Y). \tag{2.33}$$

Chapter 3

State of Research

In this chapter, the main findings from previous research carried out by former students on topics closely related to the present work are reviewed. Although the earlier studies were performed using a different experimental rig and a different numerical solver, the results obtained provided a valuable foundation and context for the development of the current project.

3.1 Quasi Steady-State Heat Transfer Rig

Figure 3.1 shows the disassembled qSSHT rig used in the previous studies. The system consists of two main sections: an inlet and an outlet module, both fabricated from Polyamide-12 using Selective Laser Sintering (SLS). These modules house the pressure and temperature measurement devices. Between the two sections, a copper block is mounted, into which the test object (TO) is inserted. Thermal paste is applied between the TO and the copper block to ensure good thermal contact and reduce interfacial resistance. Two electric heaters are attached to the external surface of the copper block in order to impose a constant wall-temperature boundary condition during operation.

Before entering the test section, the air temperature and pressure are measured at the rig inlet. Inside the copper block, two temperature sensors are installed at different radial positions to monitor the internal temperature distribution. After passing through the test object, the fluid temperature and pressure are measured again at the outlet. A schematic representation of the full setup is shown in Figure 3.2.

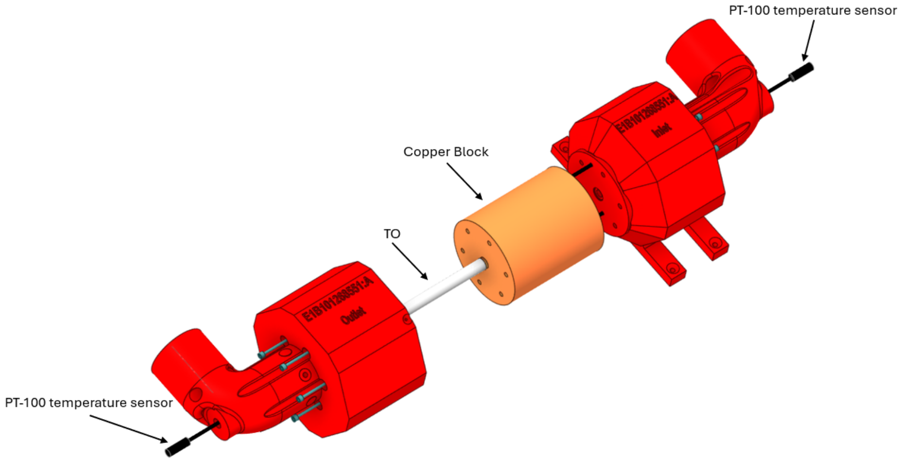

Figure 3.1: CAD model of the qSSHT rig [42].

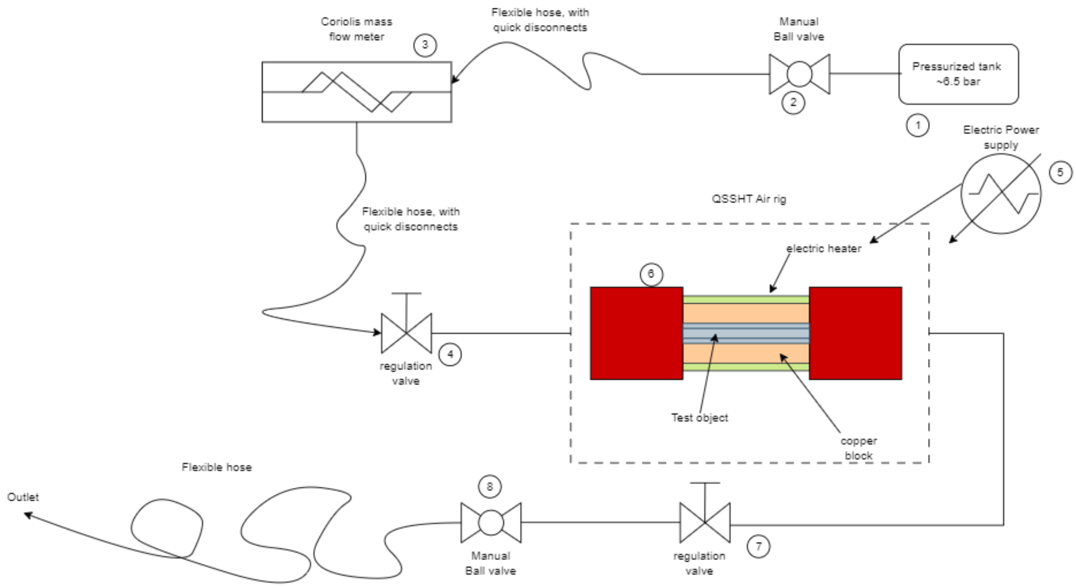

Figure 3.2: Experimental setup of the qSSHT rig [42].

3.1.1 Post-Processing Solver

The experimental data obtained from the qSSHT rig were post-processed using two different solvers, since the complete procedure consists of two independent tests.

3.1.1.1 Darcy Friction Factor Test

The post-processing of the friction-factor test is performed using Python and MATLAB scripts previously developed in the laboratory. The Python script processes the raw experimental data to compute the pressure losses inside the channel using the Darcy friction factor, as defined by Eq. 3.1. The MATLAB script then plots the resulting friction factors against a Moody chart for comparison.

$$f_D = \Delta p \frac{D_h}{L} \frac{2}{\rho u^2} \tag{3.1}$$

Air is assumed to behave as a perfect gas; therefore, its density is computed using the ideal-gas relation (Eq. 3.2). The mean velocity in the conduit is then obtained using the continuity equation (Eq. 3.3), treating the flow as compressible. For this purpose, the tests are conducted such that the Mach number remains below 0.3, ensuring that compressibility effects remain small and manageable.

$$\rho = \frac{P}{RT} \tag{3.2}$$

$$u = \frac{\dot{m}}{\rho A} \tag{3.3}$$

The geometric dimensions of the TO play a crucial role in the evaluation. As shown in Eq. 3.4, the Darcy friction factor is proportional to D_h^5, making the accurate determination of the hydraulic diameter essential. Even small deviations in channel dimensions may therefore have a significant impact on the computed friction factor.

$$f_D = 2\frac{D_h}{L}\rho\frac{A^2 \Delta p}{\dot{m}^2} \quad \Longrightarrow \quad A = \frac{\pi}{4}D_h^2 \quad \Longrightarrow \quad f_D = \frac{\pi D_h^5 \rho \Delta p}{8 L \dot{m}^2} \tag{3.4}$$

The Darcy friction factor accounts only for frictional losses within the conduit. Therefore, pressure losses associated with sudden expansions and contractions must be subtracted from the measured differential pressure, as expressed in Eq. 3.5.

Figure 3.3 shows the configuration of the pressure taps. These are intentionally positioned far from the inlet and outlet sections to avoid recirculation zones and local disturbances that could bias the measurement.

It is important to note that the pressure sensors installed in the rig measure exclusively the static pressure, since they are flush-mounted on the wall and do not stagnate the flow. As a consequence, the dynamic pressure is not directly measured but must be computed from the mean flow velocity using $p_{\text{dyn}} = \frac{1}{2}\rho u^2$. The total pressure difference used in the evaluation is therefore obtained as the sum of the static and dynamic components. This distinction is essential for correctly removing the inlet and outlet losses, which depend solely on the dynamic pressure.

Finally, the friction-related pressure drop is computed using Eq. 3.6, where the coefficients c_{in} and c_{out} are given in Table 3.1 and were previously discussed in Section 2.1.6.1. After determining Δp_f, the Darcy friction factor is calculated using Eq. 3.1.

$$\Delta p = \Delta p_{tot} - p_{in,loss} - p_{out,loss} \qquad \text{with} \qquad \Delta p_{tot} = p_{stat} + p_{dyn} \tag{3.5}$$

$$\Delta p_f = \Delta p_{tot} - c_{in} p_{in,dyn} - c_{out} p_{out,dyn} \tag{3.6}$$

Table 3.1: Inlet and outlet loss coefficients [23]

Coefficient	**Laminar**	**Turbulent**
c_1	0.5	0.5
c_2	2.0	1.0

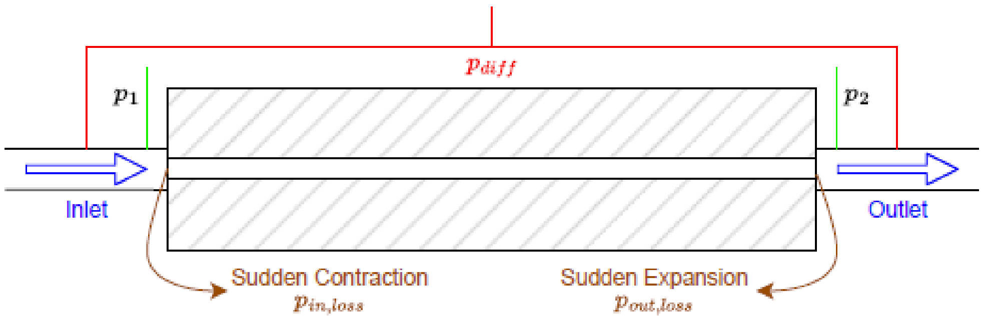

Figure 3.3: Sketch of pressure-tap locations.

3.1.1.2 Heat Transfer Test

The heat-transfer model used in the previous studies was developed under the following assumptions:

- **Quasi-steady-state:** The thermal evaluation is performed under conditions that vary slowly in time. The copper block heats up gradually, with a typical rate of approximately $1\,°\mathrm{C/h}$, allowing each acquisition step to be treated as nearly steady.
- **Cylindrical conduit geometry:** For axisymmetric test objects, an axisymmetric radial-conduction model is applied.
- **Uniform convective coefficient:** The convective heat-transfer coefficient h is assumed constant along the channel, meaning that local axial variations (e.g. entrance effects) are not included in the model.

Figure 3.4 illustrates the radial thermal-resistance network considered in the model. The top section represents the contact resistance associated with the thermal paste; the central section corresponds to radial conduction within the test object (TO); and the bottom section represents the forced-convection thermal resistance of the airflow.

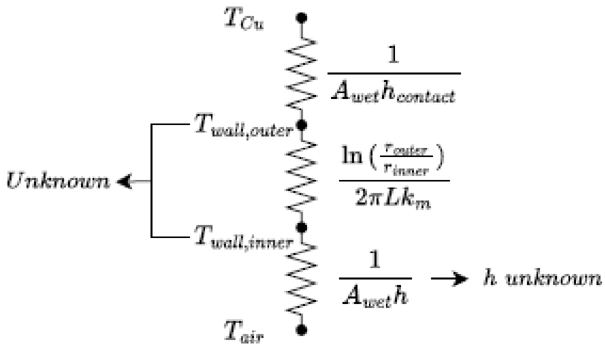

Figure 3.4: Radial thermal-resistance scheme.

Because several quantities in the system are unknown, a discretization procedure is used to determine the heat-transfer coefficient h. The test object is divided into infinitesimal axial elements, as shown in Figure 3.5, and the radial scheme of Figure 3.4 is applied to each segment. The thermal contact conductance between the copper block and the TO is assumed to be $h_{\text{contact}} = 10^4\,\text{W}/(\text{m}^2\,\text{K})$.

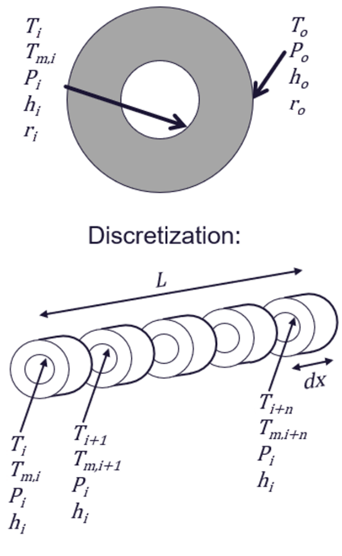

Figure 3.5: Axial discretisation of the test object.

The heat flux per unit length in each segment is computed using Eq. 3.7, starting from the inlet temperature T_{in} and marching downstream from $i = 1$ to 200. For each segment, the local heat balance determines the outlet air temperature T_{i+1}, which is passed to the next segment.

$$\dot{q}_i = \frac{T_{Cu} - T_i}{\dfrac{1}{Ph} + \dfrac{\ln\left(\frac{D_o}{D_i}\right)}{2\pi k_m} + \dfrac{1}{nD_{o,\text{contact}}}}, \qquad T_{i+1} = T_i + \frac{\dot{q}_i\,dx}{\dot{m}c_p} \tag{3.7}$$

The convective heat-transfer coefficient h is assumed uniform along the axial direction and is computed using the iterative procedure shown in Figure 3.6. In each iteration, h is adjusted until the model-predicted outlet temperature matches the measured temperature T_{out}. The thermophysical properties of air are evaluated at the average temperature between inlet and outlet.

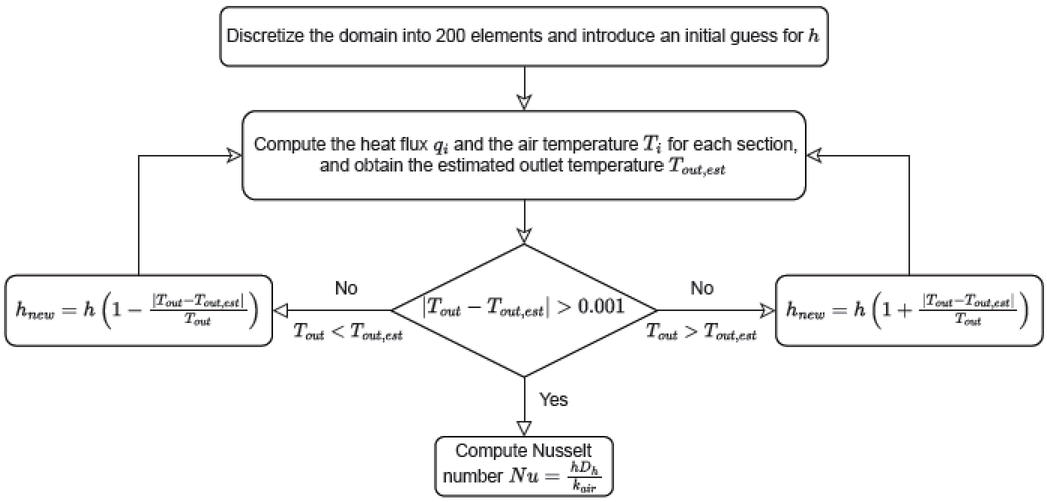

Figure 3.6: Iteration scheme used to compute the Nusselt number for each Reynolds number.

The approach described above assumes an axisymmetric cylindrical geometry for the TO, allowing the use of the analytical radial-conduction model. For non-axisymmetric test objects, however, the internal solid conduction cannot be represented by the cylindrical model. In such cases, the same iterative procedure is followed, but the conduction inside the solid is computed using the actual CAD geometry in the C3D finite-element solver (Siemens Energy in-house tool). The FEM solution for the conduction field is combined with the iterative matching of the outlet temperature to determine the global average heat-transfer coefficient h. Figure 3.7 shows an example of a C3D thermal model.

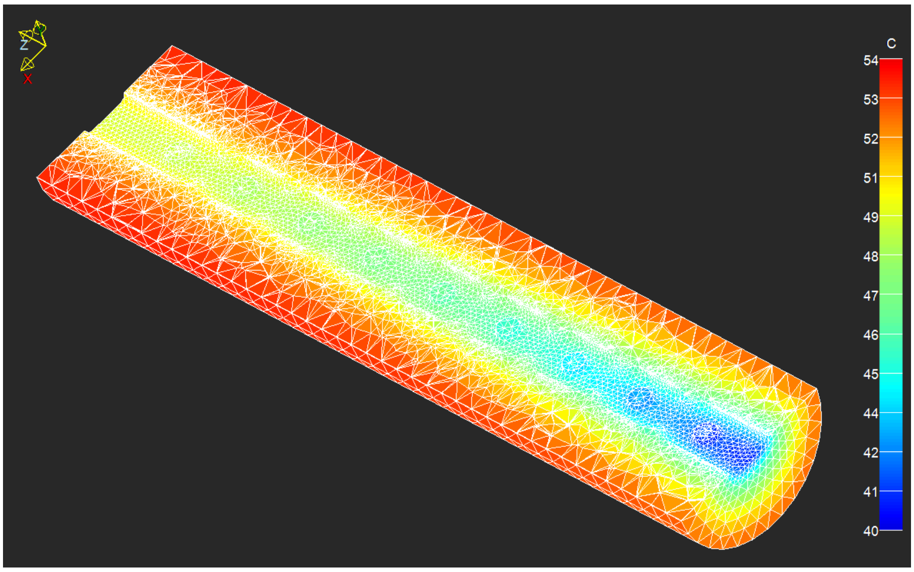

Figure 3.7: C3D thermal model of a pin-fin test object at 700 °C metal temperature.

3.1.2 Limitations of the Setup

- **Uncertainty associated with the thermal-paste layer:** The amount of thermal paste applied to the TO surface is difficult to control and quantify. This layer introduces an additional thermal resistance that strongly affects the measured heat flux, particularly at higher Reynolds numbers. Figure 3.8, based on results from previous work, shows a clear dependency of the measured heat transfer on the thickness of the thermal-paste layer. Because this thickness cannot be accurately measured or reproduced, it represents one of the dominant sources of uncertainty in the rig.

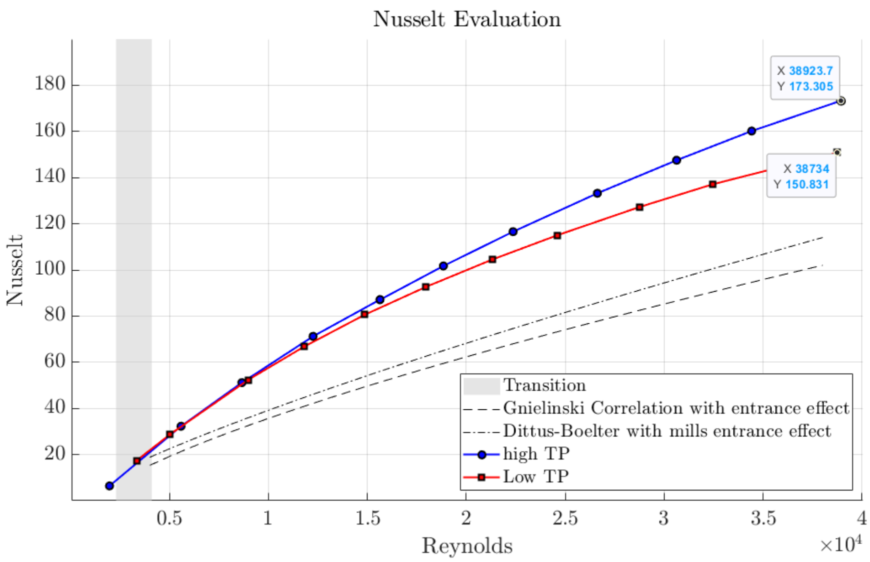

Figure 3.8: Influence of thermal-paste thickness on measured heat transfer [42].

- **Inaccessibility of the TO surface for local measurements:** The TO is mounted inside the copper bar, which makes its external surface inaccessible during testing. As a result, it is not possible to measure local temperature distributions or local heat-transfer coefficients directly along the TO surface. The analysis is thus restricted to global, integrated quantities rather than detailed local heat-transfer phenomena.
- **Thermal behaviour of plastic inlet and outlet components during long-duration tests:** The inlet and outlet sections of the rig are made of plastic and are assumed adiabatic in the Nusselt-number evaluation. However, each test lasts for one or more days, which makes this assumption questionable. Over such long durations, heat losses through the plastic components may become non-negligible, especially as the copper-bar temperature increases. Without a detailed thermal characterisation of these components, it is not possible to accurately evaluate the magnitude of these losses or their influence on the measured heat transfer.

Chapter 4

Experimental Setup and Methodology

This chapter describes the physical setup used to acquire the experimental data and the procedures followed to operate the test rig.

4.1 Quasi Steady-State Heat Transfer Rig

The qSSHT (quasi-Steady-State Heat Transfer) rig is designed to heat the test object (TO) using Joule heating while a controlled air stream flows through its internal passage. The electrical current generates heat within the TO, which is then transferred to the airflow. By measuring the temperature rise between inlet and outlet, together with the pressure drop across the channel, both heat-transfer and flow characteristics can be determined.

The main elements of the test section are:

- **Test object (TO):** A straight cylindrical tube clamped between two copper bars, through which the air flows.
- **Scanivalve:** A pneumatic scanning valve allowing a single pressure transducer to sequentially sample multiple pressure taps. This enables accurate pressure-drop measurements using one high-precision sensor.
- **Parker T-connectors for pressure measurement:** The first set of Parker T-connectors, installed at the inlet and outlet of the TO, provides the interface between the pressure taps and the Scanivalve system. Small probe elements extend into the flow to measure static pressure, while the T-connectors ensure a compact and organised routing of the tubing. This configuration allows rapid switching between different pressure ports without modifying the main piping, improving repeatability.
- **Parker T-connectors for the air loop:** A second set of T-connectors routes compressed air into and out of the TO, completing the pneumatic circuit and ensuring stable flow conditions during operation.

- **PT100 sensors:** Long PT100 resistance thermometers are installed at both ends of the rig to measure the bulk air temperature at the inlet and outlet. Their placement ensures accurate readings while maintaining mechanical protection.
- **Copper bars:** Two massive copper bars mechanically and electrically clamp the TO. They conduct the high electric current required for Joule heating while maintaining a limited temperature rise due to their large cross-section and auxiliary cooling.

For clarity, Figure 4.1 provides a CAD representation of the complete qSSHT rig, while Figure 4.2 illustrates the configuration specifically used for the Darcy friction-factor measurements. Figure 4.3 shows the physical test section, and Figure 4.4 presents the same assembly covered with a thick neoprene insulating layer to minimise environmental heat losses.

During the friction-factor tests, the PT100 sensors mounted at the tail section of the rig are removed to avoid disturbing the airflow. Moreover, the inlet and outlet tubes used in this configuration are intentionally longer, functioning as calming sections to promote a fully developed flow before the air enters the TO, as seen in Figure 4.2.

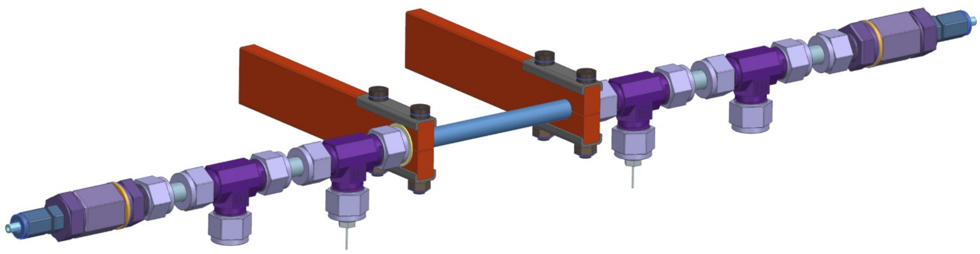

Figure 4.1: CAD design of the new qSSHT rig [43].

Figure 4.2: CAD design of the friction-factor test configuration [43].

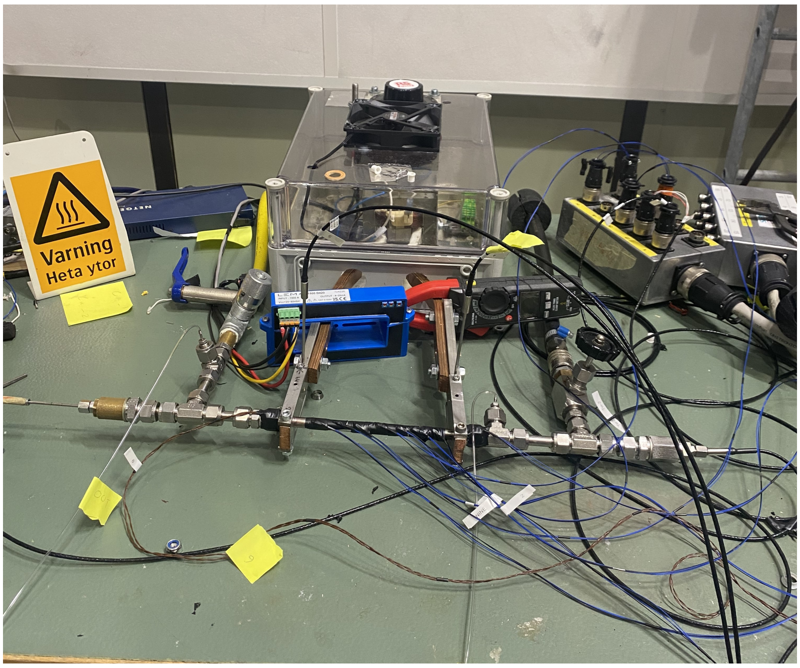

Figure 4.3: Physical qSSHT Joule-heating rig.

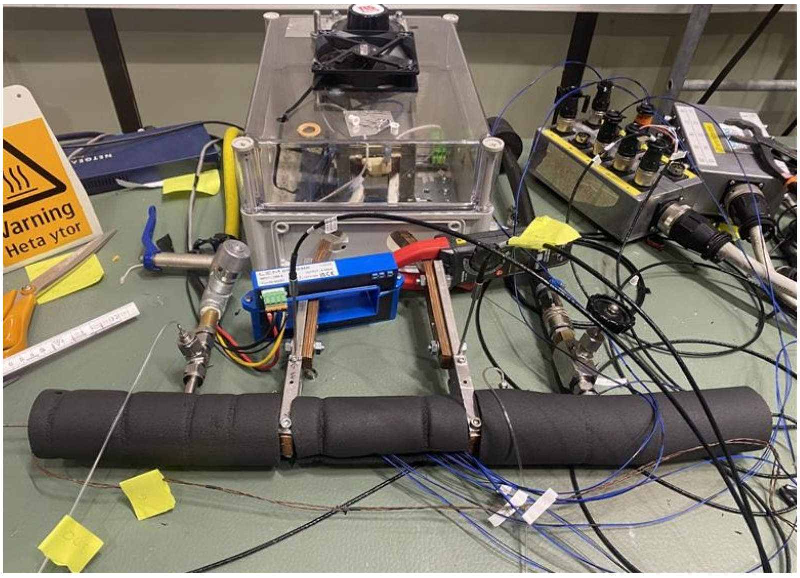

Figure 4.4: qSSHT rig with neoprene insulation layer.

4.1.1 Air Loop

The qSSHT rig is supplied by a pressurised air tank operating at approximately 6.5 bar, which delivers air to the test line through flexible hoses. At the inlet, a manual ball valve provides coarse control of the mass-flow rate, while a regulating valve positioned downstream allows fine tuning of the pressure level inside the test section. This dual-valve arrangement ensures stable operating conditions and enables the flow to be adjusted such that the Mach number remains below 0.3 during all tests, thereby preventing compressibility effects and ensuring the validity of incompressible-flow correlations.

Figure 4.5 shows a schematic representation of the air-supply line, highlighting the main flow-control components and the path followed by the compressed air as it enters, passes through, and exits the qSSHT rig.

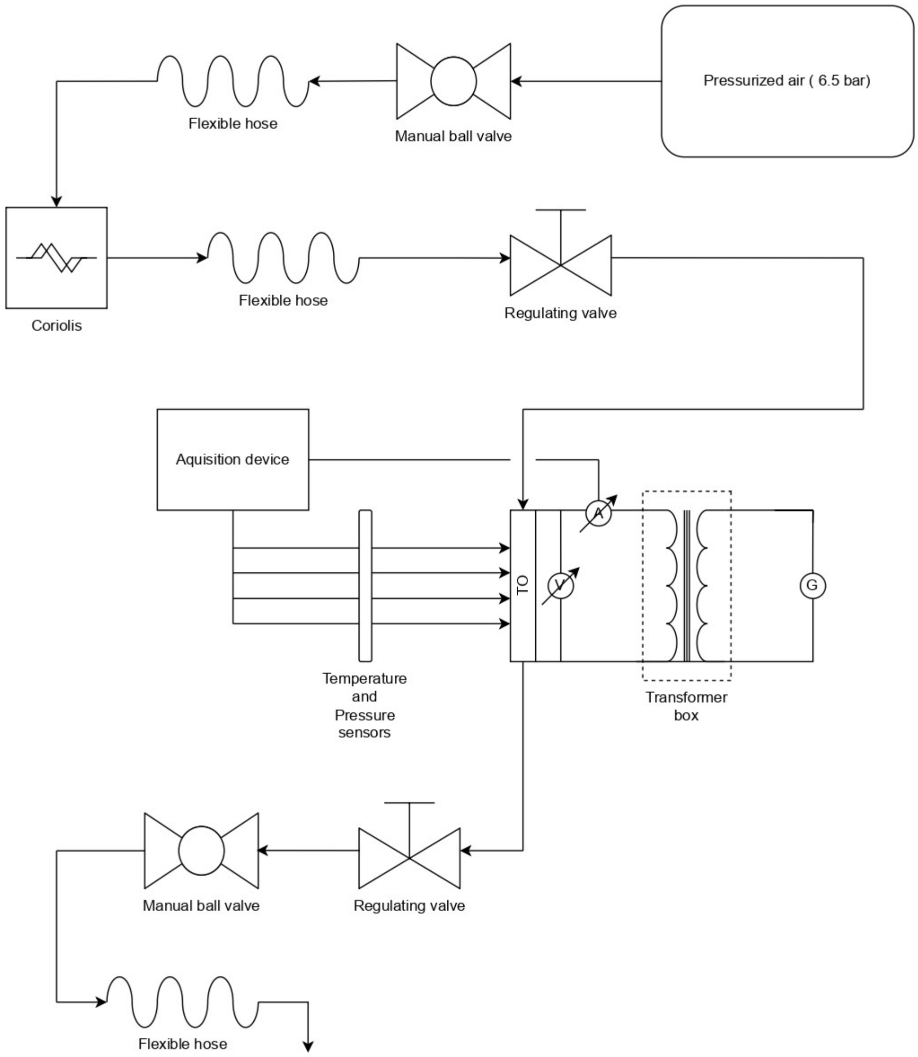

Figure 4.5: Schematic of the qSSHT air-supply system.

4.1.2 Electrical Loop

The electrical loop provides controlled Joule heating to the test object (TO) using an alternating current at the mains frequency (50 Hz AC). The system, shown in Figure 4.6, is designed to deliver high currents at very low voltages while ensuring safe and stable operation of both the specimen and the power electronics. The main elements of the electrical loop are:

- **Autotransformer:** A variable autotransformer is used to adjust the input voltage from 0 to the mains level of 230 V. Its output can be continuously regulated by varying the number of active secondary windings. The unit is rated for up to 8 A on the secondary side, and an upstream circuit breaker provides protection against overloads, ensuring safe operation.

- **Fixed Transformer:** Downstream of the autotransformer, a custom low-voltage, high-current transformer supplies the power required for Joule heating.

  The original transformer configuration consisted of approximately 230 turns on the primary side and a single copper bar on the secondary, producing a transformation ratio of about 230:1 and a secondary voltage close to 1 V.

  In the present configuration, the secondary consists of a 35 mm^2 copper cable wound twice around the core, resulting in an effective ratio of 230:2 and a maximum secondary voltage close to 2 V. The transformer is designed for continuous operation at 240 A, and currents up to approximately 340 A can be reached when active cooling is applied.

  The ability to modify the number of secondary turns provides flexibility to adapt the output current to test objects with different electrical resistivities.

- **Copper bars:** The low-voltage, high-current output of the transformer is delivered to the TO through two copper bars with a cross-section of 10×30 mm^2. These bars offer a very low electrical resistance while securely clamping the test object in place. Due to their large cross-section, the copper bars exhibit minimal self-heating even at high currents, ensuring electrical stability throughout the tests.

- **Induction Ammeter:** The current supplied to the TO is monitored using an induction ammeter based on the current-transformer (CT) principle. A ferromagnetic core is placed around the conductor carrying the primary current, and a secondary winding is connected to the data-acquisition system. The time-varying magnetic field produced by the AC primary current induces a proportional secondary current, enabling accurate and galvanically isolated current measurement.

- **Power Supply and Cooling Fans:** An AC–DC converter delivers 12 V DC from the 230 V mains supply to power the forced-convection cooling system. One 120 mm fan directs airflow across both the transformer and the copper clamps, enhancing heat dissipation. This additional cooling capacity allows the electrical system to operate safely closer to its upper current limit without excessive component temperatures.

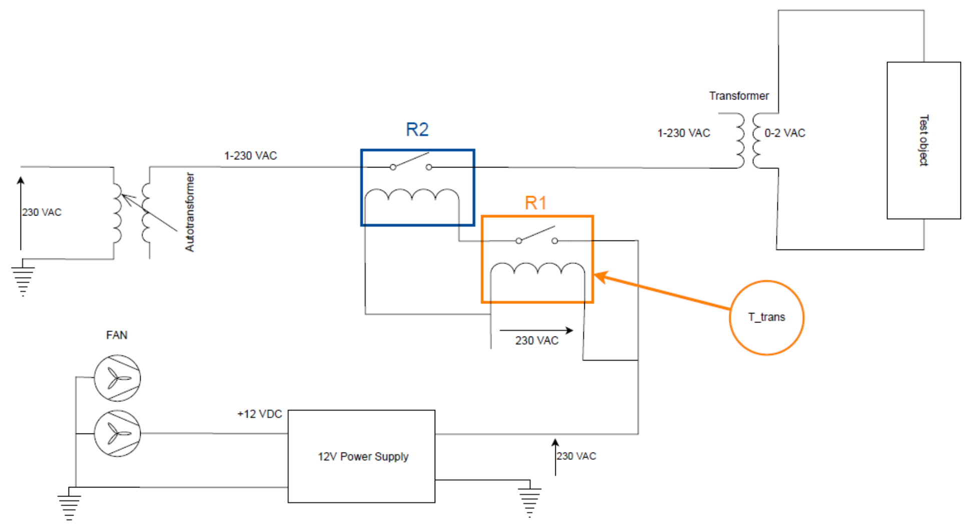

Figure 4.6: Electrical loop of the qSSHT rig.

4.1.3 Measurement Instrumentation and Data Acquisition

To extract meaningful information from the experiments, several measurement devices are required, and their accuracy directly affects the reliability of the results. Table 4.1 summarises the instruments used to characterise the hydraulic and thermal behaviour of the test object (TO). The following quantities are measured: static pressure difference between inlet and outlet (ΔP), mass flow rate ($\dot{m}$), air temperatures at the inlet (T_{in}) and outlet (T_{out}), surface temperatures along the TO ($T_{meas,1}$ to $T_{meas,N}$), temperature of the fittings ($T_{fittingIn}$, $T_{fittingOut}$) and temperature of the copper bars ($T_{busbarIn}$, $T_{busbarOut}$).

Table 4.1: Measurement devices, ranges and uncertainties

Parameter	Device	Range	Uncertainty	Unit
Mass flow ($\dot{m}$)	Coriolis	0.01–6 g/s	0.56%	g/s
Static pressure (p_{in}, p_{out})	PSI 9116	0–689 kPa	0.015%	kPa
Atmospheric pressure (p_{atm})	Rosemount 3051CA1	80–200 kPa	0.015%	kPa
In/Out air temperature (T_{in}, T_{out})	PT100 (sheathed)	0–200°C	0.05°C	°C
Copper temperature ($T_{\text{busbar,In}}$, $T_{\text{busbar,Out}}$)	PT100 (sheathed)	0–200°C	0.05°C	°C
External surface temperature ($T_{meas,1}$-$T_{meas,N}$)	PT100 (unsheathed)	0–500°C	0.15°C	°C
Fittings temperature ($T_{fittingIn}$,$T_{fittingOut}$)	PT100 (unsheathed)	0–500°C	0.15°C	°C

Each measurement device used in the rig is briefly described below.

Temperature probes

Two types of PT100 temperature sensors are employed:

- **Sheathed PT100 sensors** integrated in the inlet, outlet caps, and copper bars to measure bulk air temperatures close to the entrance and exit of the TO and to measure copper temperatures.

Figure 4.7: Pentronic PT100 sensor used for air inlet/outlet temperature.

- **Small unsheathed PT100 sensors** attached directly to the outer wall of the test object and the parker connections to obtain an approximate axial wall-temperature profile.

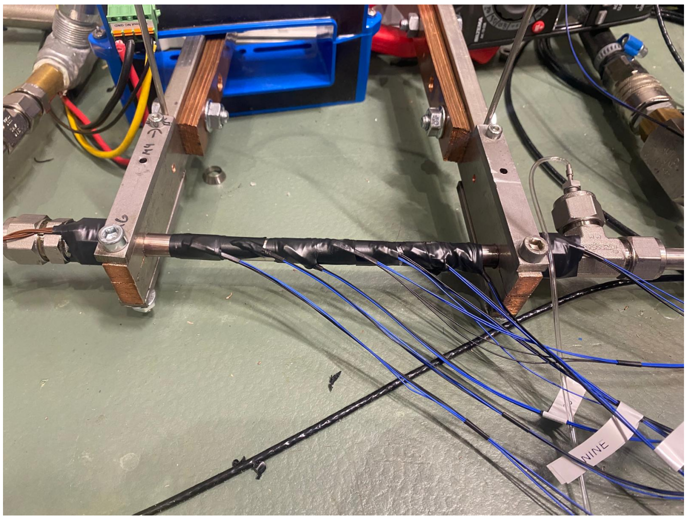

Figure 4.8: Unsheathed PT100 sensors attached in the wall of the TO and the parker connections.

Coriolis mass-flow meters

Two Coriolis meters are available: #10 and #21. Coriolis #10 offers better accuracy at low mass flows but becomes less reliable above 0.95 g/s. Coriolis #21 is suited for higher flows but inaccurate below 1 g/s. Both instruments are shown schematically in Figure 4.9.

Pressure transducers

Pressure measurements use two types of transducers:

- **Rosemount 3051CA1** (absolute transducer), used to measure atmospheric pressure.
- **NetScanner 9116** (differential transducer), used to measure the pressure drop between inlet and outlet of the TO.

Pressure transducers typically consist of a diaphragm membrane that deflects under pressure difference. Absolute sensors reference atmospheric pressure or an internal vacuum chamber, whereas differential sensors measure the difference between two connections, which is essential for the Darcy friction-factor evaluation.

Data acquisition from all sensors is carried out using the RigView internal software developed at Siemens Energy. RigView reads the raw signals from the hardware, performs calibration conversions, and provides real-time monitoring of temperatures, pressures, voltages, currents and mass flow. Figure 4.10 shows the software interface during operation.

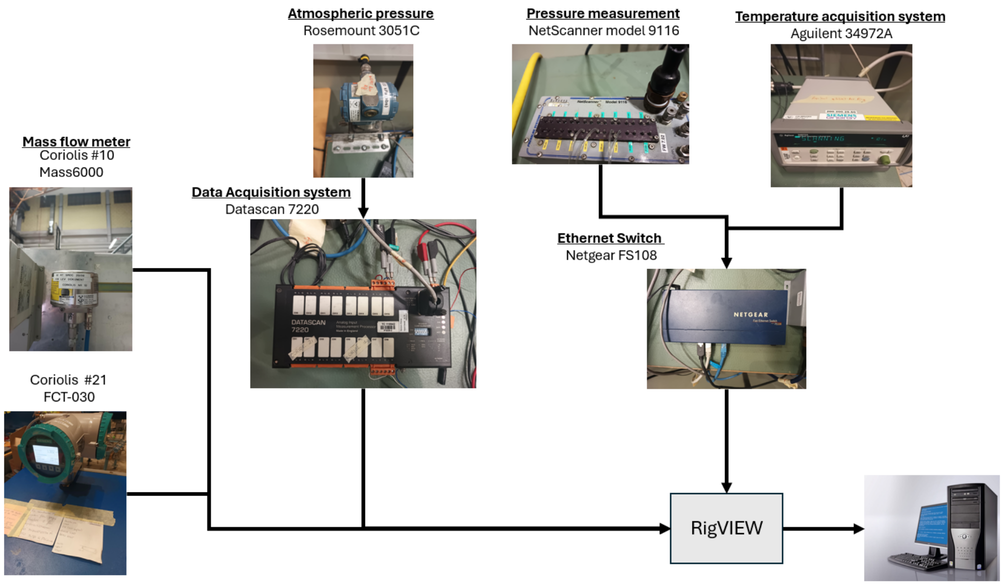

Figure 4.9: Visual representation of the measurement devices used in the qSSHT rig.

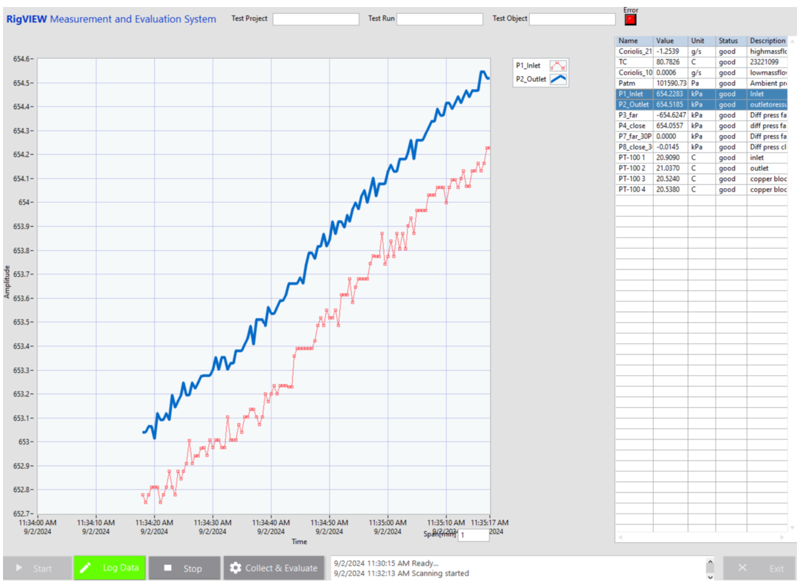

Figure 4.10: RigView interface during a test.

4.1.4 Test Objects

The test objects (TOs) investigated in this study are designed to replicate the internal cooling channels found in turbine blades. In real components, these passages are typically narrow ducts through which cooling air flows. To emulate such geometries, the additively manufactured (AM) test objects used in this work were produced with different internal cross-section shapes, dimensions and lengths.

To enable effective Joule heating during qSSHT operation, the outer surface of each printed test object was machined after manufacturing. By reducing the wall thickness—and therefore the conductive cross-sectional area—the electrical resistance increases, allowing a higher heat generation for a given current, according to:

$$P_{\mathrm{el}} = I^2 R. \tag{4.1}$$

The same principle motivated the selection of the smooth stainless-steel pipe used for thermal-performance validation. The pipe has an outer diameter of 10 mm and an inner diameter of 8 mm, resulting in a wall thickness of 1 mm. This thin wall increases the electrical resistance sufficiently to enable heating while minimising surface roughness effects, allowing the pipe to behave as an almost perfect hydraulically smooth reference.

Another reason why heat is generated predominantly within the test object and not in the copper clamps is the large difference in electrical resistivity between the materials. Copper has a very low resistivity ($\rho_{\mathrm{Cu}} \approx 1.7 \times 10^{-8}\,\Omega{\cdot}\mathrm{m}$), whereas stainless steel is one to two orders of magnitude higher ($\rho_{\mathrm{SS}} \approx 7\text{–}8 \times 10^{-7}\,\Omega{\cdot}\mathrm{m}$). Given that electrical resistance is defined as

$$R = \rho \frac{L}{A}, \tag{4.2}$$

the stainless-steel TO dissipates the majority of the electrical power. The copper clamps, which combine extremely low resistivity with a much larger cross-sectional area, contribute negligibly to the overall resistance and thus remain essentially unheated.

As a result, the Joule heating occurs almost entirely inside the test object, while the copper bars act as low-resistance electrical conduits that support the TO mechanically and electrically without significant self-heating.

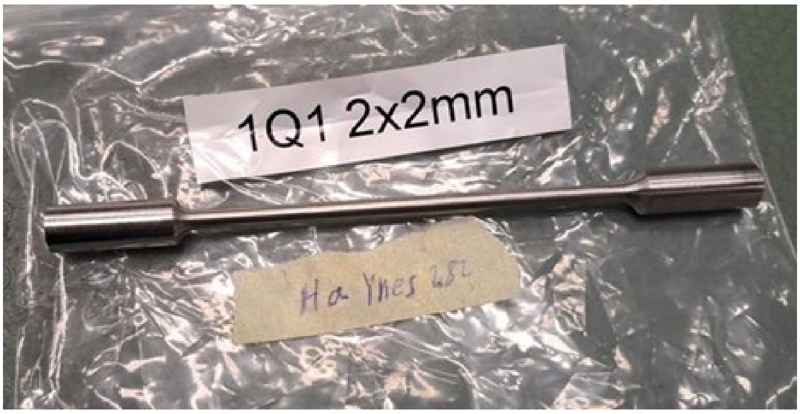

Figure 4.11: Machined test object: Haynes 282, 2 mm × 2 mm square channel.

4.1.4.1 Dimensions and Relative Roughness

Table 4.2 summarises the geometric dimensions of the two test objects. The hydraulic diameter was estimated from microscope images of the inlet and outlet sections, as will ne described in detail in Section 4.4.1. Both test objects are made of stainless steel, and surface characterization performed with a profilometer yielded an average roughness of $R_a = 10.08\,\mu$m and a peak-to-valley roughness of $R_z = 66.83\,\mu$m [44].

The relative roughness of each channel is computed from the peak-to-valley roughness using:

$$\varepsilon = \frac{R_z}{D_h}. \tag{4.3}$$

Using this expression, the relative roughness of each test object was determined and is reported together with the geometric parameters in Table 4.2.

Table 4.2: Dimensions and relative roughness of the test objects

Name	Material	D_h [mm]	A [mm^2]	Length [mm]	Relative Roughness ε
Haynes 2×2 mm square	Stainless Steel	2.097	4.40	150	0.0319
SS 4 mm circular	Stainless Steel	3.89	11.885	170	0.0172

4.1.4.2 Electrical and Thermal Conductivity

Since the heat-transfer experiments take place between approximately 20 ºC and 100 ºC, the material properties of the test object vary significantly over this temperature range. While the thermal conductivity was provided by the manufacturer, the electrical conductivity had to be determined experimentally. For this purpose, an electrical resistivity test was conducted as described below.

Figure 4.12 shows the experimental setup. The test object (TO) was connected to the power supply through the copper busbars and operated without air flow, ensuring that Joule heating was the sole source of temperature rise. Several surface-mounted PT100 sensors were distributed along the outer wall of the TO to capture the temperature distribution. The test section was wrapped with an insulation layer to minimise heat losses and promote a uniform, quasi-steady thermal field.

For each imposed voltage level, the following quantities were recorded:

- the electrical current flowing through the test object,
- the surface temperatures measured by each PT100 sensor,
- the electrical power supplied to the test object, computed as $P = VI$.

By gradually increasing the applied voltage and allowing the test object to reach steady state at each step, a consistent set of (V, I, T) data points was obtained. These measurements formed the basis for determining the temperature-dependent electrical resistivity of the material.

Because the first and last sections of the TO include additional material interfaces (Parker fitting and copper contact), their thermal mass is higher. Consequently, the temperatures measured by the first and last PT100 sensors were assigned greater weights in the calculation of the effective electrical temperature, denoted T_{weighted}:

$$T_{\text{weighted}} = w_1 T_1 + \sum_{i=2}^{n-1} w_n T_i + w_n T_n. \tag{4.4}$$

The electrical resistance corresponding to each voltage step was then calculated as:

$$R(T_{\text{weighted}}) = \frac{V}{I}. \tag{4.5}$$

The electrical resistivity was obtained from:

$$\rho(T_{\text{weighted}}) = R(T_{\text{weighted}}) \frac{A}{L}, \tag{4.6}$$

where A is the cross-sectional area and L is the effective conductor length.

Finally, the electrical conductivity was computed as:

$$\sigma(T_{\text{weighted}}) = \frac{1}{\rho(T_{\text{weighted}})}. \tag{4.7}$$

Table 4.3 presents the electrical and thermal conductivity values obtained from the resistivity test carried out on the stainless-steel test object.

Table 4.3: Electrical and thermal conductivity as a function of temperature (stainless steel)

T (ºC)	**Electrical Conductivity (S/m)**	**Thermal Conductivity (W/m·K)**
21	1 315 789	16.200
93	1 219 512	17.970
204	1 111 111	20.369

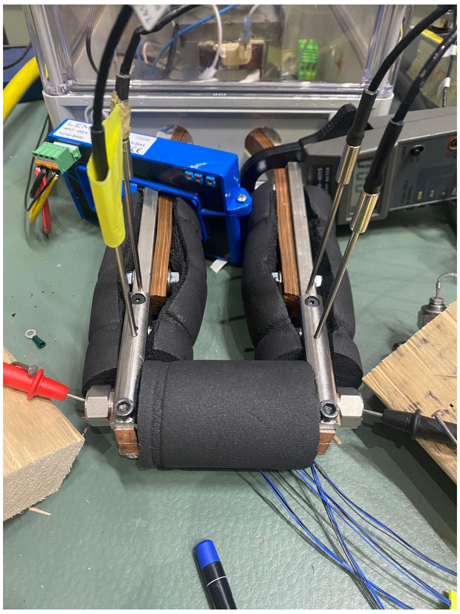

Figure 4.12: Experimental setup used for the electrical resistivity test.

4.2 Limitations of the qSSHT Rig

Heat Losses

A fundamental limitation of the qSSHT rig when operating with air as the working fluid is the high proportion of thermal losses relative to the useful heat transferred to the flow. Because air has a low specific heat capacity and the mass flow rates achievable in small internal channels are inherently limited, the thermal power absorbed by the air becomes comparable to the heat lost through the busbars, clamps and surrounding hardware.

This creates a challenging energy-balance problem: the electrical input power must be partitioned between the useful heat transferred to the fluid, $\dot{q}_{\text{fluid}}$, and the parasitic heat losses, $\dot{q}_{\text{loss}}$. Under these conditions, the inverse method becomes highly sensitive to uncertainties in the thermal boundary conditions imposed on non-adiabatic surfaces. Even small errors in estimating contact resistances, ambient convection or heat spreading through the copper busbars can noticeably affect the computed heat-transfer coefficient.

To better understand where the thermal losses occur, a complementary rough calculation was performed. Using handheld multimeter readings taken both at the copper–Parker interface and directly across the copper clamps, the heat absorbed by the air was estimated from the energy balance $q = \dot{m}c_p(T_{\text{out}} - T_{\text{in}})$ and compared with the electrical power inferred from the voltage drop across the busbars and the TO.

These calculations show that the Parker fittings contribute only a negligible fraction of the total losses. For the smooth TO and for three representative operating points (Re = 19 900–22 500), the fraction of power lost in the Parker fittings remains below 0.35%, as indicated by the very small difference between the measured inlet and outlet voltages (V_{in} and V_{out}).

In contrast, the voltage drops measured directly across the copper clamps indicate that between 14% and 23% of the supplied electrical power is dissipated before reaching the airflow. This clearly shows that the dominant losses originate from the **copper–test-object contact interface**, where contact resistance, imperfect clamping pressure and small geometric misalignments cause additional Joule heating.

These findings confirm that the main limitation of the rig is not associated with the tubing or fittings, but rather with the thermal–electrical coupling at the copper–TO interface. Improvements in mechanical clamping force, surface preparation, and interface geometry are therefore essential to reducing losses and improving the reliability of the Nusselt number evaluation.

Wall temperature measurement

Wall temperatures are obtained from the PT100 sensors mounted on the outer surface of the test object. Although these sensors provide stable and repeatable readings, several factors introduce local errors in the estimation of the true wall temperature. Contact resistance between the sensor and the metal surface, local heat spreading through the sensor body, and circumferential variations in wall thickness all contribute to deviations between the measured and actual internal wall temperature.

A further source of uncertainty arises at the first and last measurement locations (Points 1 and 5), where steep temperature gradients occur near the inlet and outlet. As shown in Figure 4.13, the wall temperature may change by several degrees over only a few millimetres. Because the PT100 surface sensors have an active sensing area of roughly 2 mm and must be positioned manually, even a small axial misalignment of 1–2 mm during installation may place the sensor in a region with significantly different temperature. Consequently, the measured wall temperature at the first and last points may not correspond exactly to the intended axial position, leading to an over- or underestimation of the local heat-transfer coefficient.

This effect is particularly pronounced in these two segments, where thermal gradients are strongest; hence, small positional deviations translate into disproportionately large measurement errors. For this reason, the HTC computed at Points 1 and 5 must be interpreted with caution, and greater emphasis is placed on the central measurement locations, where the temperature field is smoother and the measurement uncertainty is lower.

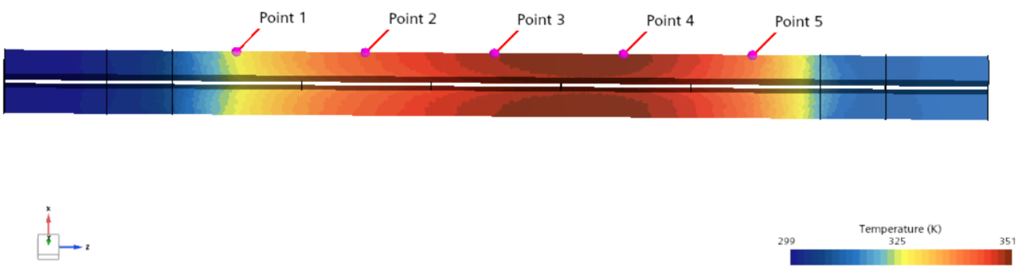

Figure 4.13: Temperature gradients along the TO wall (Star-CCM+ simulation).

4.3 Soldered Solution

As discussed in the previous section, heat losses at the contact surface between the copper bars and the TO constitute one of the main limitations of the setup. In an attempt to minimize these losses, one potential solution considered was to solder the TO to the copper bars using a silver-based solder. Silver was selected due to its exceptionally high thermal conductivity, which allows for a much more efficient heat transfer across the interface and a significantly reduced contact resistance. According to Eq. 4.1, this reduction in resistance would decrease the parasitic heat generation associated with the thermal contact. However, implementing this solution requires extensive workshop involvement and is therefore not the most practical option.

As an alternative to soldering, the TOs were machined in the outer surface, as discussed in Section 4.1.4, reducing the cross-sectional area of the TO increases the heat generation within the material. Both approaches—silver soldering and precision machining—were evaluated and compared. A sensitivity analysis was carried out in Section 7.6, and the results showed that both methods lead to nearly identical outcomes in terms of measured heat transfer. Therefore, soldering does not offer sufficient benefit to justify its implementation, and the machined solution was adopted.

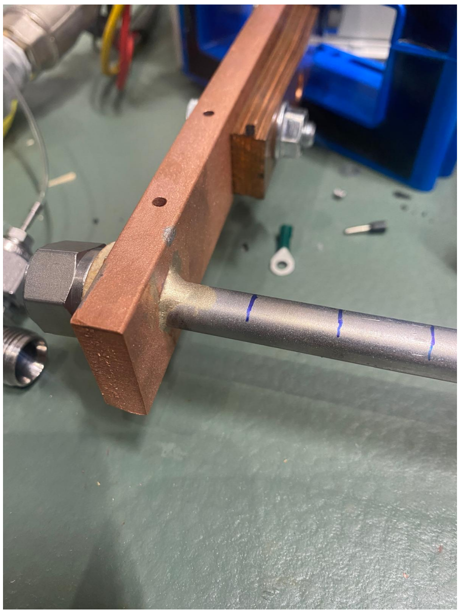

Figure 4.14: Soldered contact between copper bar and test object.

4.4 Pre-Processing

Before the execution of each experiment, a pre-processing phase is performed to ensure that all test conditions are properly defined and that the rig operates under controlled and repeatable conditions. This stage is essential because small geometric deviations in the test objects (TOs), assembly imperfections, or undetected leaks in the rig can significantly affect the measured pressure drop, heat transfer, and flow characteristics.

4.4.1 Microscope Pictures and Geometric Evaluation

The nominal dimensions of the test objects are known from the manufacturer; however, due to fabrication tolerances, it is necessary to determine the actual internal geometry of each TO to obtain accurate channel dimensions.

As a first step, a microscope is used to acquire high-resolution images of both the inlet and outlet sections of each TO (Figure 4.15a). The inlet face is selected as the reference for all geometric computations to remain consistent with previous evaluations. The outlet region is partially machined for electrical contact, which may alter its geometry; therefore, the inlet section provides a more reliable representation of the true internal cross-section.

For each TO, two microscope images of the inlet (at different magnifications) and one of the outlet are taken to minimise possible measurement errors.

After image acquisition, a dedicated MATLAB script is used to extract the geometry. The user manually selects points along the rough internal boundary, allowing the code to generate a smooth averaged curve that avoids local asperity peaks caused by surface roughness. This process is illustrated in Figure 4.15b.

Once the contour is defined and the image scale is calibrated, the script computes the cross-sectional area and perimeter. The hydraulic diameter is then calculated using:

$$D_h = \frac{4A}{P} \tag{4.8}$$

Each picture is analysed three times in order to reduce uncertainty. Therefore, a total of nine measurements are obtained per TO. A second MATLAB script computes the average dimensions, which are saved to a text file and later used in the post-processing of the experimental results.

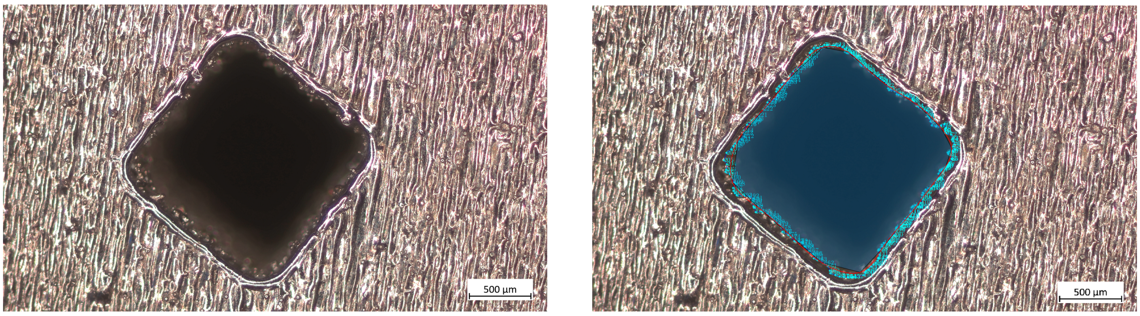

(a) Microscope picture. (b) Manual point selection.

Figure 4.15: Inlet section of the IN939 90° 90×1.5×1.5 test object.

4.4.2 Leakage Test

Before starting a test, the rig must be checked for air leakage. Any mass-flow loss introduces errors in the evaluation of both hydraulic and thermal performance.

The leakage test is performed in two phases. In the first phase, the outlet valve is fully closed while the inlet valve is opened, allowing the system to reach its maximum internal pressure. A soap–water mixture is then applied to critical locations, such as pressure taps and pneumatic connectors. The presence of bubbles, as shown in Figure 4.16, indicates a leak.

In the second phase, once the system is fully pressurised, the inlet valve is also closed. The inlet and outlet pressure traces are monitored in RigView. The pressure drop should not exceed 3 kPa per minute, and the inlet pressure must always remain higher than the outlet pressure. If these conditions are met, the rig is considered sealed and ready for testing. Otherwise, the system must be disassembled, inspected, and reassembled until the leakage criteria are satisfied.

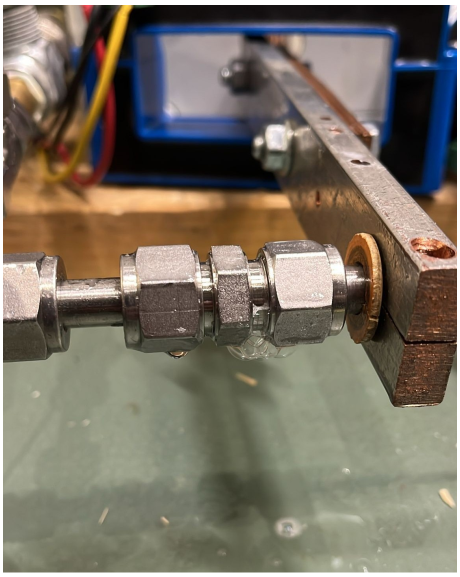

Figure 4.16: Leak detected in a connector using soap–water solution.

4.5 Test Procedures

Two tests were performed for each test object (TO) to evaluate its hydraulic and thermal behaviour: the Darcy friction-factor test and the heat-transfer test. Both procedures are described below.

4.5.1 Darcy Friction Factor Test

The objective of the Darcy friction-factor test is to characterise the flow behaviour inside the TO by measuring the pressure loss along its length.

This test is carried out at ambient temperature, starting from a low mass flow rate of approximately 0.005 g/s and progressively increasing it to the maximum value achievable with the available supply pressure. To avoid compressible-flow effects, the inlet and outlet valves are continuously adjusted so that the Mach number remains below 0.3 throughout the entire test. This condition ensures that the air can be treated as incompressible and prevents errors in the pressure-drop evaluation.

Because the friction factor depends strongly on the measured pressure difference, achieving high accuracy is essential. To minimise pressure-measurement errors, two differential pressure sensors with different ranges are used, as summarised in Table 4.4. Once the upper limit of the low-range sensor is reached, the test is paused to switch the connections to the higher-range sensor, after which the test continues.

Table 4.4: Specifications of differential pressure sensors

Sensor	**Range [kPa]**
Tab 9	≤ 101
Tab 6	> 101

Table 4.5: Friction-factor test procedure

Step	**Action**
1	Check hoses and device connections.
2	Perform zero adjustment of pressure and mass-flow instruments.
3	Turn on the mass flow, close the outlet valve, and open the inlet valve to pressurise the system.
4	Perform leakage test.
5	Fully open the outlet valve and adjust the inlet valve to reach the desired mass flow rate; wait until the operating point becomes stable.
6	Record the point in RigView once the differential-pressure signal becomes stable.
7	When the Mach number approaches 0.2, fully open the inlet valve and regulate the flow with the outlet valve to avoid compressibility effects.
8	Repeat Steps 5–7 until enough operating points are collected.
9	Turn off the main flow and depressurise the rig.

4.5.2 Heat-Transfer Test

The heat-transfer test is performed by activating the electrical heater and gradually reducing the mass flow rate from its maximum achievable value. To avoid thermal damage to both the TO and the copper clamps, the outer-surface temperature is limited to approximately 90 °C.

Operating at higher mass-flow rates in the initial phase helps the system reach steady conditions more rapidly. Data points are collected only when the inlet/outlet temperatures, pressure drop, and electrical current reach quasi-steady-state values.

During the test, the voltage is reduced slowly while the electrical current and wall temperatures are closely monitored to prevent overheating of the TO or copper bars.

Table 4.6: Heat-transfer test procedure

Step	**Action**
1	Check hoses and device connections.
2	Perform zero adjustment of pressure and mass-flow instruments.
3	Turn on the mass flow, close the outlet valve, and open the inlet valve to pressurise the system.
4	Perform leakage test.
5	Close the main flow, open both valves, and turn on the heating system.
6	Once the TO surface temperature reaches approximately 75–85 °C, open the mass flow with both inlet and outlet valves fully open.
7	Record the operating point when T_{in}, T_{out}, pressure drop, and current reach quasi-steady behaviour.
8	Slightly close the outlet valve and wait for a new stable point before collecting the next measurement.
9	Turn off the heater and allow the rig to cool down.
10	Turn off the mass flow.

Chapter 5

Pseudo-code of the Numerical Solver

This chapter describes the numerical methodology developed to identify the local heat-transfer coefficient (HTC) distribution inside the cooling channel of the test object (TO). The workflow combines a steady-state conjugate heat-transfer simulation with temperature-dependent electromagnetic heating, implemented in Star-CCM+ and driven by a custom Java macro.

5.1 Model Setup

5.1.1 Geometry and Regions

The TO geometry is imported into Star-CCM+ from a CAD file or created directly using the 3D-CAD environment. The following requirements are imposed:

- the flow enters at $z = 0$ and proceeds in the positive z-direction;
- external and internal surfaces are subdivided using curves to allow consistent assignment of thermal and electrical boundary conditions.

Surface segmentation is performed using the *Divide Face* and *Split by Part Curves* tools. The resulting named surfaces include:

- internal-channel walls (channel_1, channel_2, ..., channel_N), each segment centred between two wall-temperature measurement locations;
- Parker fitting contact surfaces (FittingIn, FittingOut);
- busbar contact surfaces (BusbarIn, BusbarOut);
- external surfaces that remain adiabatic within the effective heat-transfer length of the TO (i.e. surfaces between the two busbars).

All surfaces are assigned to a single region, with each named surface becoming an independent boundary.

The mesh is generated using the automated polyhedral mesher in Star-CCM+, with a base cell size of 1.5–2 mm. The polyhedral mesher applies local refinement automatically around curved surfaces and small geometric features. An example of the mesh distribution is shown in Figure 5.1.

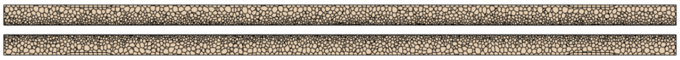

Figure 5.1: Mesh distribution on the test object.

5.1.2 Physics Models and Material Properties

The continuum for the solid region includes the following physics models:

- **Steady-State Solid Energy Equation**: Although the simulation is steady-state, "pseudo-transients" appear because the Java macro updates material properties and boundary conditions between solver calls.

  The steady-state heat-conduction equation in the solid reads:

  $$0 = \nabla \cdot (k(T)\nabla T) + q_{\text{gen}}, \tag{5.1}$$

  where $k(T)$ is the temperature-dependent thermal conductivity and q_{gen} is the volumetric Joule heat generation.

- **Electric Potential Equation**: Electric conduction inside the solid follows Ohm's law:

  $$\mathbf{J} = \sigma(T)\mathbf{E}, \tag{5.2}$$

  where $\sigma(T)$ is the temperature-dependent electrical conductivity.

  The corresponding volumetric Joule heating is:

  $$q_{\text{gen}} = \mathbf{J} \cdot \mathbf{E}. \tag{5.3}$$

- **Contact Resistance and Boundary Heat Generation.** Electrical losses at the busbar–TO interface are imposed as a boundary heat flux:

  $$q''_{\text{contact}} = J_n^2 R^{\text{User}}, \tag{5.4}$$

  where J_n is the normal current density and R^{User} is the user-specified electrical contact resistance.

Temperature-dependent thermal and electrical conductivities are imported from a tabulated data file using a *File Table*. The table is linked to the solid material model and updated automatically during the macro iterations. Section 4.1.4.2 describes the experimental procedure used to obtain these property curves.

5.1.3 Boundary Conditions

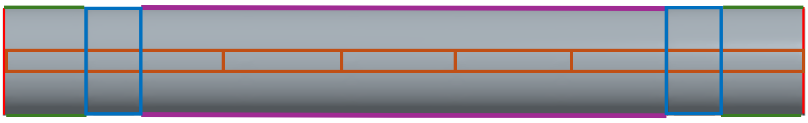

Figure 5.2: Boundary condition distribution on the test object.

Figure 5.2 illustrates the boundary conditions applied in the numerical model. Each coloured surface corresponds to a different thermal or electrical constraint, described in detail below:

- **Copper busbars (blue)**
  - *Thermal:* imposed external temperature (T_{busbarIn}, $T_{\text{busbarOut}}$) and a fixed convection coefficient (see Section 7.4).

$$h_{\text{busbar}} = 10\,000 \text{ W}/(\text{m}^2\,\text{K}),$$

  - *Electrical:* Joule heating due to contact resistance, applied as a boundary heat flux:

$$q''_{\text{busbar}} = J_n^2 R_{\text{contact}}, \tag{5.5}$$

    where J_n is the normal current density and R_{contact} is the experimentally fitted contact resistance.

- **External walls within busbars (purple)**
  - Adiabatic (zero heat flux). These surfaces lie within the effective heat-transfer length and are thermally shielded from the ambient.

- **Fittings (green)**
  - Forced convection with a fixed heat-transfer coefficient

$$h_{\text{fitting}} = 400 \text{ W}/(\text{m}^2\,\text{K}),$$

    and measured surface temperature ($T_{\text{fittingIn}}$, $T_{\text{fittingOut}}$). The choice of 400 $\text{W}/\text{m}^2\text{K}$ is justified by the sensitivity study presented in Section 7.5.

- **Inlet and outlet faces (red)**
  - Adiabatic for thermal analysis;
  - Ideal electrical contact (zero electrical resistance).
- **Internal channel walls (orange)**
  - Convective boundary condition exchanged with the internal flow:

$$q_i'' = h_i\,(T_{\text{wall},i} - T_{\text{fl},i}),$$

where the local heat-transfer coefficients $h_1, \ldots, h_N$ are the unknowns of the inverse problem and $T_{\text{fl},i}$ is the local bulk-fluid temperature obtained from 1D energy integration.

Axial Discretisation of the Internal HTC

The axial HTC distribution is discretised according to the number of surface temperature sensors installed along the test object. Each PT100 is positioned at the geometric midpoint of its corresponding channel section. Only the first and last segments extend to the physical extremities of the test object, resulting in slightly longer upstream and downstream cells.

To ensure a one-to-one correspondence between HTC unknowns and wall-temperature constraints, the internal surface is divided into N segments (one per sensor). The boundaries between segments are placed halfway between adjacent PT100 locations, so that:

- each HTC_i corresponds to exactly one measured wall temperature;
- all central segments have equal length;
- only segments 1 and N extend to the inlet and outlet ends.

Figure 5.3 shows the distribution of surface sensors used in the inversion procedure.

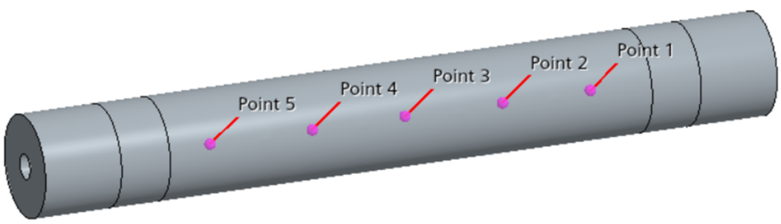

Figure 5.3: Surface temperature measurement locations (PT100 sensors).

The external HTC values (busbars, fittings) remain constant throughout the simulation. Sensitivity analyses in Sections 7.4 and 7.5 show that variations in these parameters have negligible influence on the evaluated internal HTC distribution.

5.1.4 Initial Parameters

All initial parameters of the numerical procedure are defined directly inside the Java macro. These include the thermophysical properties of the cooling air (specific heat, viscosity, Prandtl number, thermal conductivity, molecular weight), the hydraulic diameter of each test object, the number of discretised channel segments (equal to the number of surface temperature sensors, N), the electrical contact resistances at the inlet and outlet busbars, and the fixed HTC values applied to the fittings and copper clamps.

5.2 Solver Loops

Figure 5.4 presents the overall flow chart of the electromagnetic–thermal inverse solver implemented in Star-CCM+ through a Java macro. The numerical procedure relies on two nested iterative loops:

- an **outer loop**, which adjusts the global heat-transfer level until the simulated outlet temperature matches the experimentally measured one for each test point;
- an **inner loop**, which enforces consistency between the wall temperatures, the local HTC distribution, and the Joule heat generation for a fixed flow condition.

Outer Loop

For each experimental test point, the outer loop seeks the HTC distribution that makes the simulated fluid outlet temperature equal to the measured value. The initial guess for the HTC is obtained from the Dittus–Boelter correlation, Eq. (2.18). For the first test point, 60 iterations are executed to stabilise the solution before proceeding with the inverse matching procedure.

At each outer-loop iteration, the inner loop updates the current, the local HTC values and the fluid temperature field until all wall-temperature constraints are satisfied. If the convergence criteria are not met, the solver returns to the inner loop; otherwise, it proceeds to the next Reynolds-number test point.

Inner Loop

For each outer-loop iteration, the inner loop performs the following steps:

1. **Initialisation:** Initialise the temperature field using the current estimate of the HTC distribution.
2. **Update electrical current:** The electrical current is updated so that the total Joule power equals the sum of the heat absorbed by the air and the thermal losses, minus the heat dissipated through the busbar contacts:

$$I^2 R_{\text{eff}} = q_{\text{fluid}} + q_{\text{loss}} - q_{\text{busbarIn}} - q_{\text{busbarOut}}, \tag{5.6}$$

which gives:

$$I = \sqrt{\frac{q_{\text{fluid}} + q_{\text{loss}} - q_{\text{busbarIn}} - q_{\text{busbarOut}}}{R_{\text{eff}}}}. \tag{5.7}$$

Here, R_{eff} is the temperature-dependent electrical resistance of the test object.

3. **Update HTC values:** For each axial segment, the HTC is adjusted to minimise the difference between simulated and measured wall temperatures:

$$HTC_i^{(k+1)} = HTC_i^{(k)} + \alpha \left(T_{\text{wall,meas},i} - T_{\text{wall,num},i}\right),$$

where α is an under-relaxation factor.

4. **Update fluid temperature:** The fluid temperature field is computed sequentially along the channel using a 1D energy balance. For the j-th channel segment:

$$T_{fl,out} = (T_{fl,in} - T_w) \exp\left(-\frac{hA_{ch}}{\dot{m}C_p}\right) + T_w, \tag{5.8}$$

After computing the outlet temperature of each channel segment, the fluid temperature imposed as a boundary condition in the simulation is obtained using the Log Mean Temperature Difference (LMTD) formulation. In this inverse method, the LMTD gives the *mean temperature difference* between the wall and the fluid along the segment, and the absolute fluid temperature is then recovered by adding the wall temperature. The exact expression implemented in the Java code is:

$$T_{fl} = \frac{T_{fl,out} - T_{fl,in}}{\ln\left(\frac{T_{fl,out} - T_w}{T_{fl,in} - T_w}\right)} + T_w. \tag{5.9}$$

Here, $T_{fl,in}$ and $T_{fl,out}$ are the inlet and outlet fluid temperatures for the segment, and T_w is the average wall temperature computed by the solver for that same segment.

The outlet temperature of segment j becomes the inlet for segment $j+1$.

5. **Solve thermal–electrical fields:** The finite-volume solver updates the solid temperature and electric potential fields using the updated current, HTC values and fluid temperatures.

6. **Convergence check:** If the wall-temperature residuals or the energy balance are outside the tolerance, return to Step 2; otherwise, the inner loop converges.

Outer Loop Finalisation

Once the inner-loop converges for all segments, the resulting outlet temperature is compared to the measured one. If the difference is within the prescribed tolerance, the point is accepted; otherwise, the HTC distribution is globally scaled and the outer loop repeats. Figure 5.5 shows an example of the matching process in Star-CCM+.

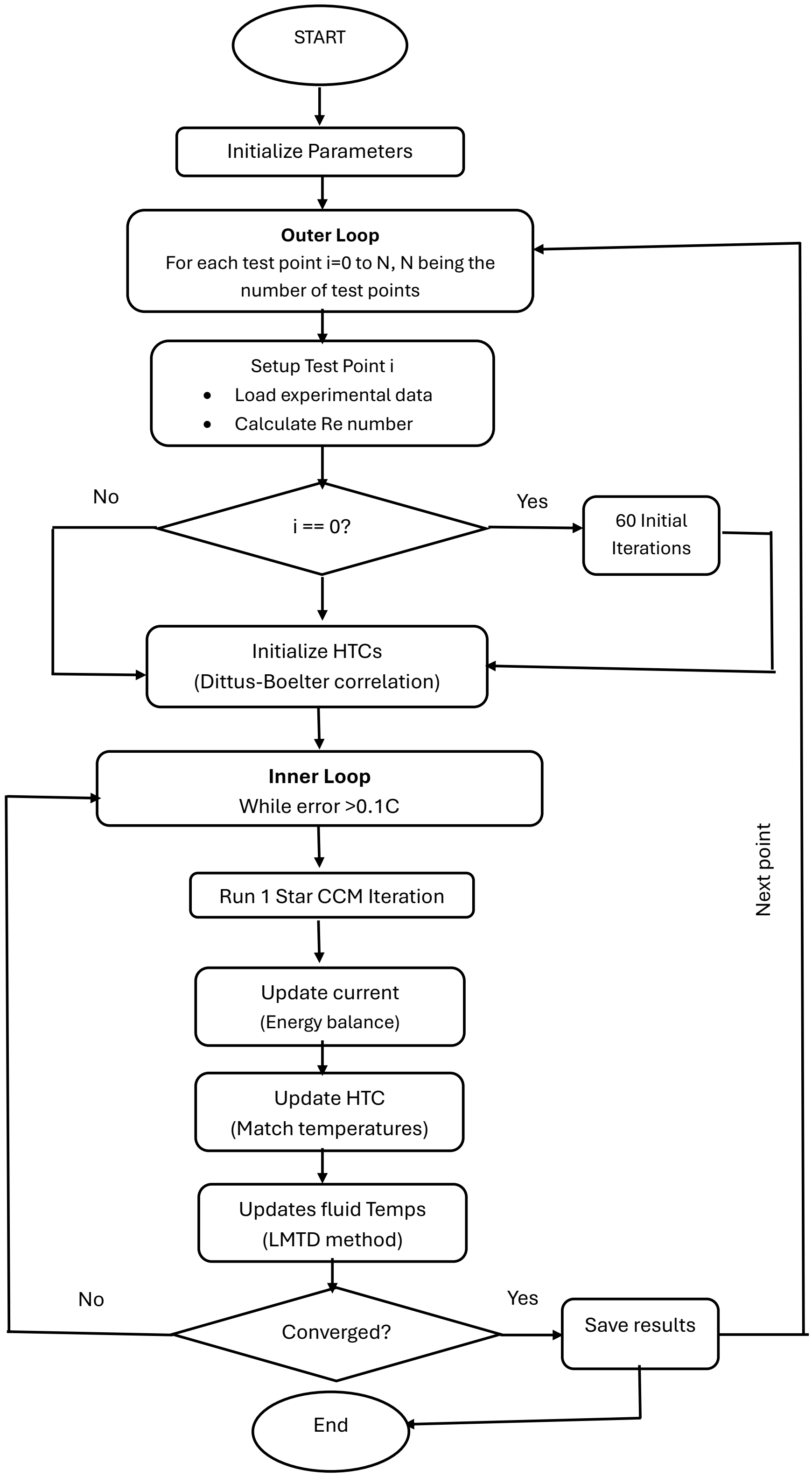

Figure 5.4: Flow chart of the solver.

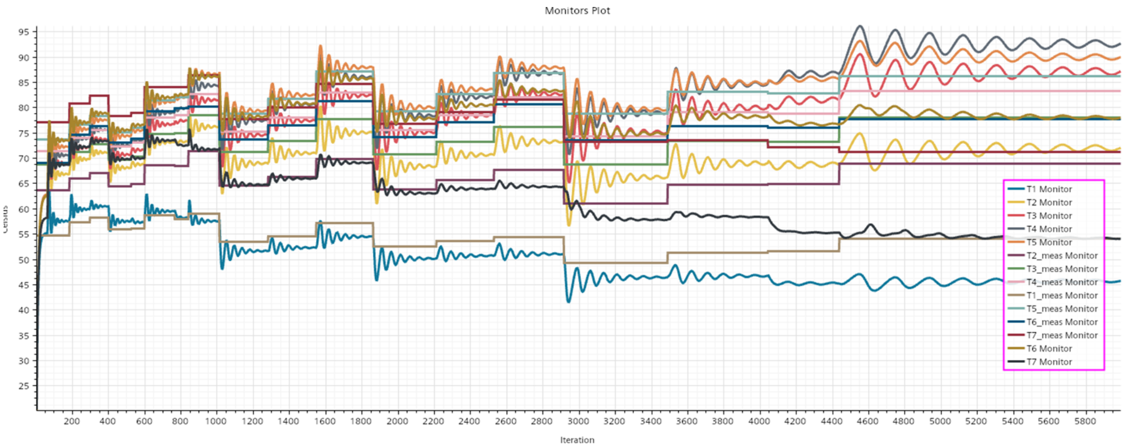

Figure 5.5: Star CCM plot.

5.2.1 Convergence Criteria

The inverse numerical method used in this work is equipped with two independent convergence criteria: an electrical power balance and a thermal energy balance. Only one of these criteria is selected and enforced during the simulation, but the availability of both provides a built-in redundancy that strengthens the validation of the computed Nusselt numbers.

The two possible criteria are:

- **Electrical power balance** The Joule heat generated inside the solid (including contact losses) must match the electrical power measured experimentally:

$$P_{\text{el,sim}} = \int_{\Omega_{\text{solid}}} q_{\text{gen}}\, \mathrm{d}V + P_{\text{contact}} \qquad \text{vs.} \qquad P_{\text{el,meas}} = UI. \tag{5.10}$$

  This criterion is particularly sensitive to the temperature-dependent electrical conductivity and to the accuracy of the measured voltage and current.

- **Thermal energy balance** The heat transferred from the solid to the fluid in the simulation must equal the enthalpy rise measured experimentally:

$$\dot{Q}_{\text{conv,sim}} = \sum_x q_x'' A_x \qquad \text{vs.} \qquad \dot{Q}_{\text{conv,exp}} = \dot{m}\, c_p \left(T_{f,\text{out}} - T_{f,\text{in}}\right). \tag{5.11}$$

  This criterion is mainly sensitive to the accuracy of the airflow temperature and mass-flow measurements.

In the numerical solver, only one of these criteria is enforced at a time to define convergence. However, as shown in Section 7.2, a sensitivity analysis demonstrates that both criteria lead to nearly identical HTC distributions and Nusselt numbers, with differences within the uncertainty of the experiment. This confirms that the inverse method is robust and that its results do not depend on which convergence criterion is selected.

5.3 Computation of Nusselt Number and Friction Factor

The final Nusselt numbers for each channel segment are extracted directly from the converged solution in STAR-CCM+, using the local heat flux, wall temperature and bulk-fluid temperature. The definition used is consistent with Eq. (2.17). For each axial segment x, the Nusselt number may be computed either from the heat-transfer coefficient:

$$\mathrm{Nu}_x = \frac{h_x\, d_h}{\lambda}, \tag{5.12}$$

or equivalently from the local heat flux:

$$\mathrm{Nu}_x = \frac{q''_x\, d_h}{\lambda\,(T_{\mathrm{w},x} - T_{b,x})}. \tag{5.13}$$

Here, q''_x is the area-averaged wall heat flux on segment x, $T_{\mathrm{w},x}$ is the corresponding average wall temperature, $T_{b,x}$ is the bulk-fluid temperature obtained from the 1D energy balance inside the inverse method, and λ is the thermal conductivity of air evaluated at $T_{b,x}$.

Friction factor. The Darcy friction factor is not computed inside STAR-CCM+, since the numerical model solves only the solid-domain conjugate heat-transfer problem. Instead, f_D is obtained from the experimental pressure-drop measurements using the Python post-processing script described in Section 3.1.1.1. Although that section was originally developed for a previous version of the qSSHT rig, exactly the same methodology is applied here.

Importantly, despite geometric differences between rigs, the inlet and outlet area transitions have identical cross-sectional ratios. Therefore, the inlet and outlet loss coefficients (c_{in}, c_{out}) remain the same as those listed in Table 3.1.

This separation of responsibilities ensures that:

- the Nusselt number is a purely **numerical quantity**, derived from the resolved heat-flux distribution in the conjugate simulation;
- the Darcy friction factor is a purely **experimental quantity**, based exclusively on pressure measurements and independent of any modelled flow field.

This guarantees that both hydraulic and thermal characteristics are evaluated without cross-contamination between numerical modelling and experimental post-processing.

5.4 Differences to the previous evaluation method

Two different methodologies have been employed to evaluate the Nusselt number in forced convection through the internal cooling channel. This subsection presents a critical comparison between the inverse-problem approach implemented in STAR-CCM+, described in this chapter, and the semi-analytical discretization method described in Section 3.1.1.2.

- **Treatment of the Energy Balance**

  The STAR-CCM+ methodology explicitly enforces global energy balance at every iteration. The electrical current is continuously updated according to Eq. (5.7), ensuring that the electrical input power equals the sum of the heat convected to the fluid and all external thermal losses. At each iteration, the model monitors the residual imbalance as an internal validation metric. This guarantees that the identified HTC distribution is thermodynamically consistent.

  In contrast, the discretization method adjusts the HTC solely to match the measured outlet temperature, without explicitly verifying the global energy balance. As a result, it may converge to an HTC that reproduces T_{out} but does not necessarily satisfy the first law of thermodynamics if unmodelled losses or simplifying assumptions are present.

- **Validation Strategy and Spatial Resolution**

  The STAR-CCM+ approach uses all surface-temperature measurements as independent constraints. Each PT100 probe provides a local target wall temperature, enabling the identification of a spatially varying HTC along the channel. This allows the method to resolve entrance effects, axial gradients, and local variations in heat generation.

  The discretization method, however, validates against a single global quantity: the outlet temperature. With only one constraint, it can determine only a single effective HTC for the entire channel length, yielding a spatially averaged Nusselt number and masking local thermal behaviour.

- **Geometric Fidelity and Physics Coupling**

  In STAR-CCM+, the full three-dimensional geometry of the test object and busbar assembly is represented—including non-uniform cross-sections, inlet and outlet fittings, and the metallic structure where electromagnetic fields are distributed. All physics (electric potential, Joule heating, solid conduction and boundary convection) are solved in a single fully coupled 3D domain.

  The discretization method adopts a hybrid strategy: conduction in non-cylindrical geometries is computed with a 3D finite-element solver (C3D), while convection is still treated as a one-dimensional model with a uniform HTC. This separation of thermal phenomena, although computationally efficient, cannot reproduce the fully coupled 3D interactions captured by the STAR-CCM+ inverse method.

In summary, the STAR-CCM+ methodology provides a thermodynamically robust HTC identification framework because:

- it enforces the global energy balance at every iteration,
- it uses multiple local temperature measurements rather than a single global constraint,

- it resolves the full 3D conjugate heat-transfer problem with electromagnetic coupling.

Even with the C3D enhancement for conduction, the discretization method cannot capture these coupled multidimensional effects and lacks a complete energy-balance verification. Therefore, for the present busbar configuration—characterised by complex geometry, electromagnetic heating and multiple available temperature measurements—the STAR-CCM+ inverse method was selected as the primary and more physically reliable evaluation approach.

Chapter 6

Results and Discussion

6.1 Rig Validation

Since this work required the development of both a new experimental rig and a new numerical inverse solver, a full validation campaign was performed to ensure that the system provides reliable hydraulic and thermal measurements. The validation was carried out using smooth test objects (TOs), allowing direct comparison with well-established theoretical correlations. Two complementary validation tests were conducted: (i) a flow-performance validation based on the Darcy friction factor, and (ii) a thermal-performance validation based on the Nusselt number.

6.1.1 Flow Performance

For the Darcy–friction-factor validation, a smooth aluminium test object (TO) with a hydraulic diameter of 2.12 mm and a length of 90 mm was used. The resulting friction factors as a function of Reynolds number are shown in Figure 6.1. The experimental data closely follows the trend expected from the Moody diagram for hydraulically smooth tubes, confirming that the rig and post-processing procedure accurately predict the Darcy friction factor.

At the highest Reynolds numbers, the curve exhibits a slight flattening. This behaviour is attributed to the residual microscopic roughness of the aluminium TO: although manufactured as "smooth", small roughness becomes relevant in the fully turbulent regime and causes the friction factor to deviate from the ideal hydraulically smooth asymptote. Nevertheless, the global agreement with the Colebrook–White prediction confirms the validity of the friction-factor measurement.

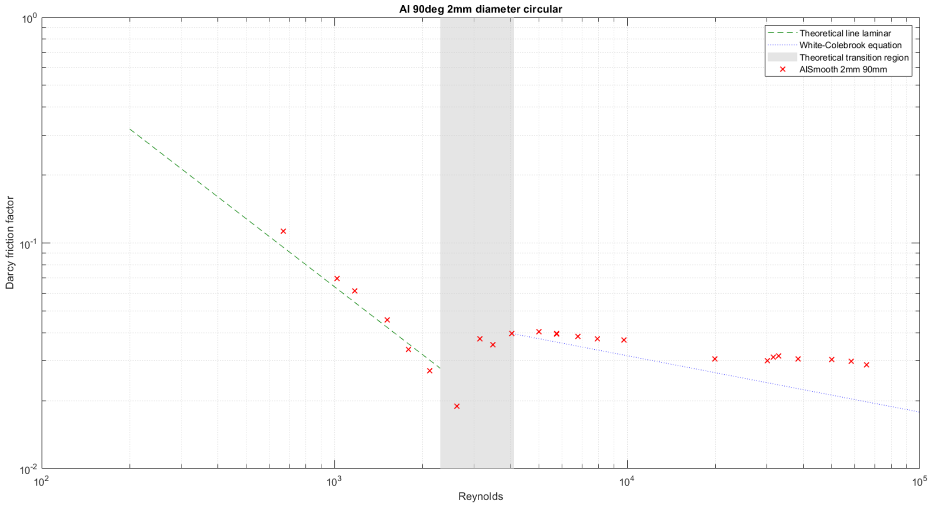

Figure 6.1: Friction-factor validation results using a smooth aluminium TO.

6.1.2 Thermal Performance

For the thermal validation, a smooth stainless-steel circular pipe with a hydraulic diameter of 7.86 mm and a length of 200 mm was employed. The experimentally determined Nusselt numbers were compared with the Gnielinski correlation, which is valid for $3000 < \mathrm{Re} < 10^6$. As shown in Figure 6.2, the experimental results fall within a $\pm 20\%$ band around the theoretical prediction, which is the typical uncertainty associated with correlations of this class. This demonstrates that the thermal behaviour measured with the qSSHT rig is consistent with established forced-convection theory.

Figure 6.3 presents the Nusselt-enhancement ratio ($\mathrm{Nu}_{\mathrm{exp}}/\mathrm{Nu}_{\mathrm{corr}}$), which quantifies the relative deviation from the correlation. The average enhancement value of 1.09 lies comfortably within the expected uncertainty range, providing an additional validation metric for the rig.

The results were also compared with the Dittus–Boelter correlation, valid for $\mathrm{Re} > 10^4$, as shown in Figure 6.4. Again, the experimental values remain within the typical $\pm 20\%$ correlation uncertainty.

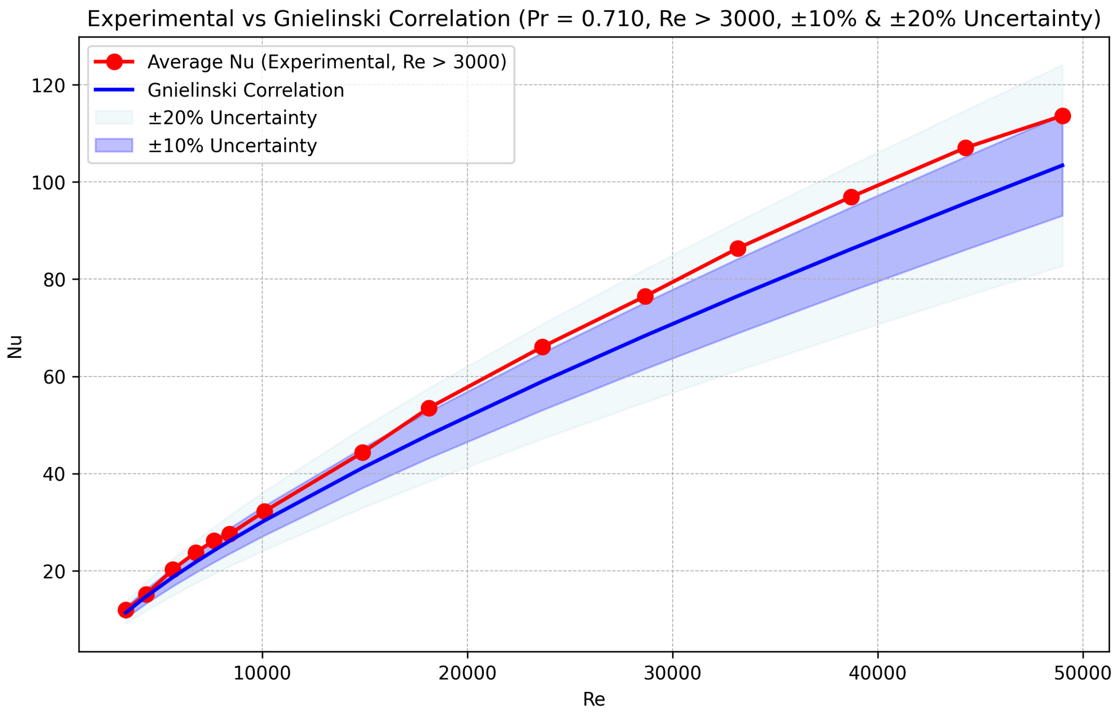

Figure 6.2: Thermal-performance validation against the Gnielinski correlation.

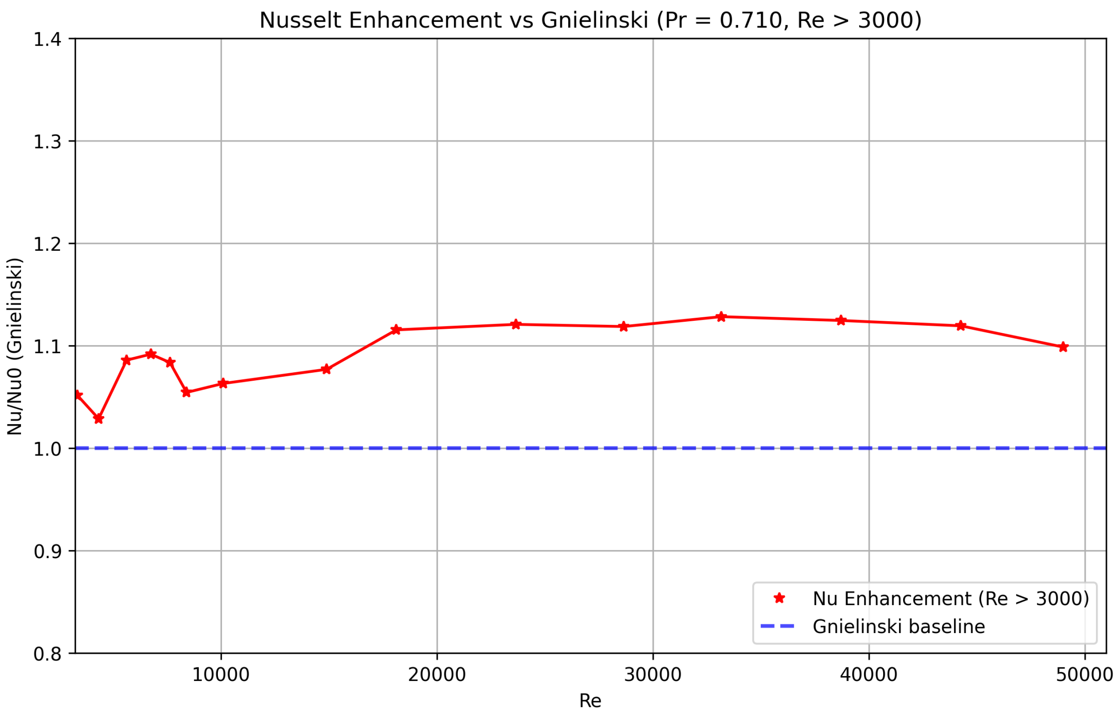

Figure 6.3: Nusselt-enhancement ratio for the smooth stainless-steel TO.

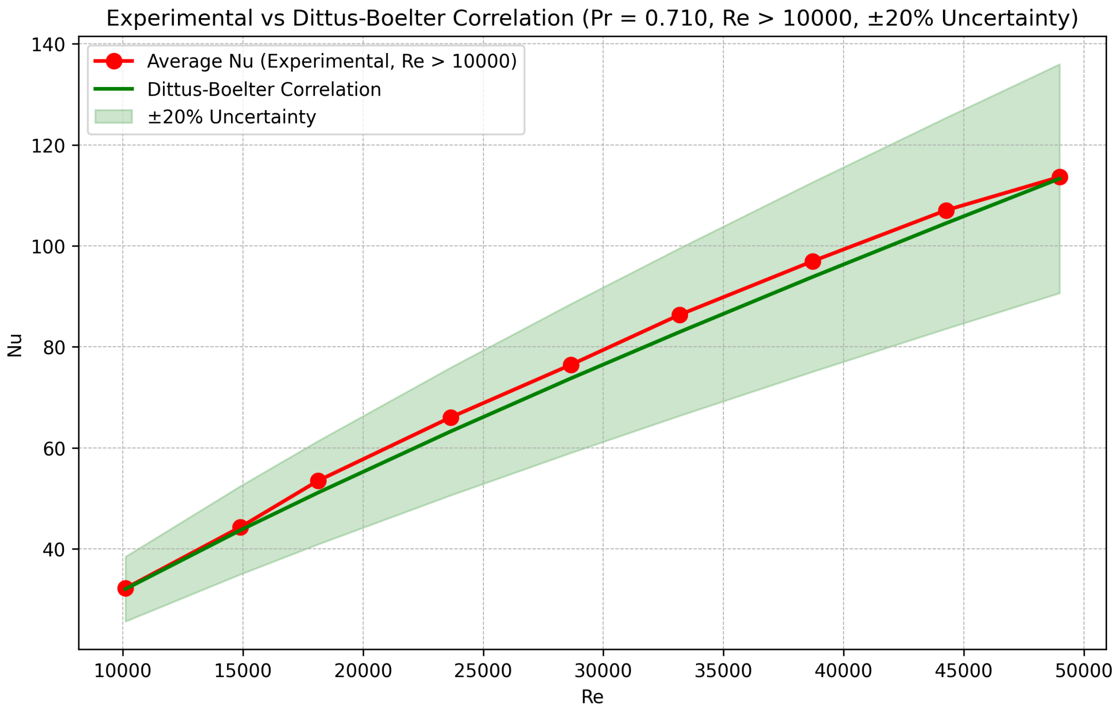

Figure 6.4: Thermal-performance validation against the Dittus–Boelter correlation.

6.2 Stainless Steel Printed Test Object

This section presents and discusses the hydraulic and thermal performance of the additively manufactured stainless-steel test objects (TOs). Their geometric characteristics and material properties were previously described in Section 4.1.4.

6.2.1 Friction Factor

The Darcy friction factor for the Haynes $2{\times}2$ mm square channel was computed directly from the measured pressure drop across the test object. The results are shown in Figure 6.5, together with smooth-tube theoretical predictions and previously acquired experimental data.

In the *laminar regime*, the experimental trend follows the theoretical Poiseuille solution, as expected when viscous forces dominate and the influence of surface roughness is minimal. A small but systematic offset is observed between the measurements and the theoretical curve. This behaviour is typically indicative of uncertainty in the estimated hydraulic diameter. Because $f \propto 1/D_h^4$ in laminar flow, even small geometric imperfections—such as slight deviations from perfect squareness or roughness-induced area reduction—can significantly affect the resulting friction factor.

In the *turbulent regime*, the friction factors exceed the smooth Colebrook–White prediction, reflecting the influence of the printed surface roughness. This deviation becomes stronger with increasing Reynolds number, in agreement with classical rough-pipe behaviour. The nearly horizontal trend at the highest Reynolds numbers suggests the early onset of a fully rough regime, where the friction factor becomes largely independent of Reynolds number and primarily governed by the relative roughness.

The good agreement between the newly acquired results and the previous dataset demonstrates the repeatability of the method and confirms that the rig is able to accurately resolve the friction-factor behaviour of rough additively manufactured channels.

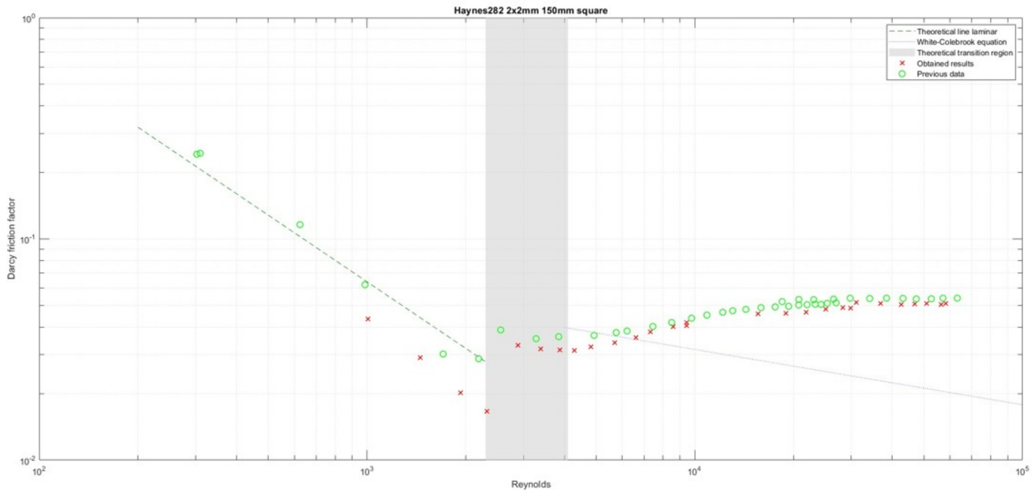

Figure 6.5: Darcy friction factor for the Haynes 2×2 mm square channel.

6.2.2 Nusselt Number

The experimentally determined Nusselt numbers for both additively manufactured test objects are presented in Figure 6.6, together with the Gnielinski correlation and its uncertainty bounds. This enables a direct comparison between the measured heat-transfer performance and the theoretical prediction for hydraulically smooth channels.

The behaviour of the two TOs differs markedly due to their relative roughness values (see Table 4.2). Although both are fabricated by additive manufacturing, the Haynes 2×2 mm square channel exhibits almost twice the relative roughness of the 4 mm circular channel. This difference is directly reflected in the heat-transfer behaviour.

For the Haynes square channel, the Nusselt number displays a strong and monotonically increasing deviation from the Gnielinski prediction. This is fully consistent with roughness-induced turbulence augmentation: rough surfaces enhance turbulent mixing, increase radial momentum transport, and thin the thermal boundary layer, leading to higher heat-transfer coefficients relative to smooth conditions.

In contrast, the 4 mm circular channel exhibits a more modest deviation, following the theoretical trend more closely. This behaviour is consistent with its significantly lower relative roughness, which results in weaker turbulence augmentation.

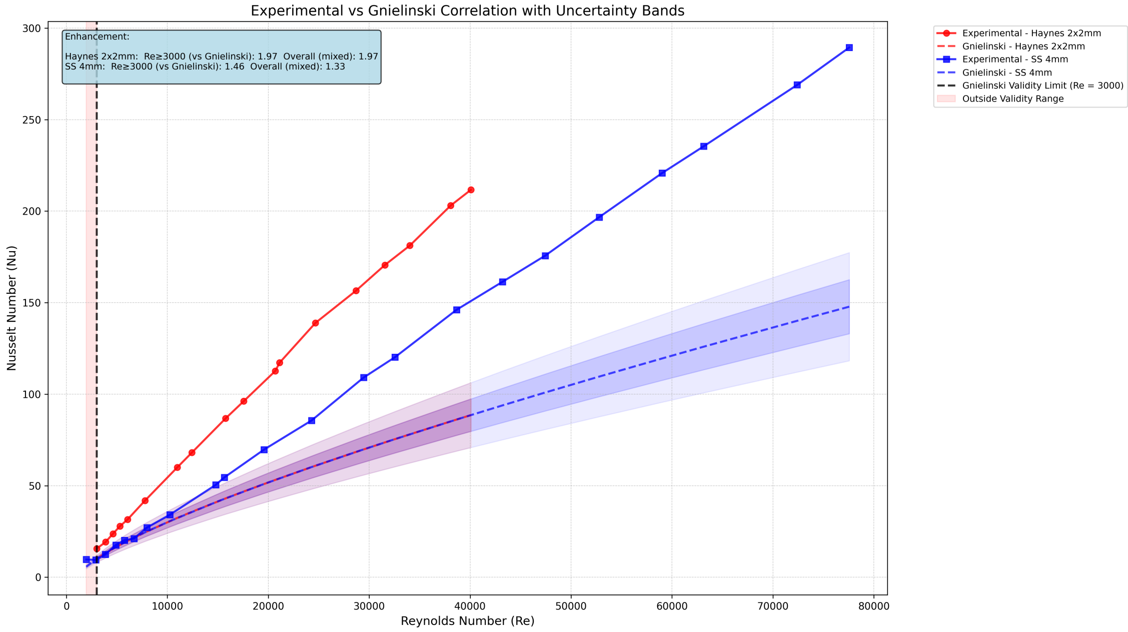

Figure 6.6: Experimental Nusselt numbers compared with the Gnielinski correlation.

A clearer illustration of the roughness influence is provided in Figure 6.7, where the Nusselt enhancement factor, $Nu_{\text{exp}}/Nu_{\text{Gnielinski}}$, is plotted for all points within the valid Reynolds-number range of the correlation ($Re \geq 3000$). For the Haynes TO, the enhancement remains consistently high, with an average of approximately 1.97, which is characteristic of additively manufactured channels with $\varepsilon \approx 0.03$. The results suggest that the flow approaches the fully rough thermal regime, in which the heat-transfer coefficient becomes only weakly dependent on Reynolds number.

The 4 mm circular channel shows a more moderate enhancement, ranging from approximately 1.0 to 1.95, with an average around 1.46. This is consistent with its lower relative roughness and the weaker disturbance it induces in the boundary layer.

Overall, both figures confirm that roughness is the dominant mechanism driving heat-transfer enhancement in these printed channels, and the measured enhancement levels align well with published behaviour for surfaces produced via laser powder bed fusion.

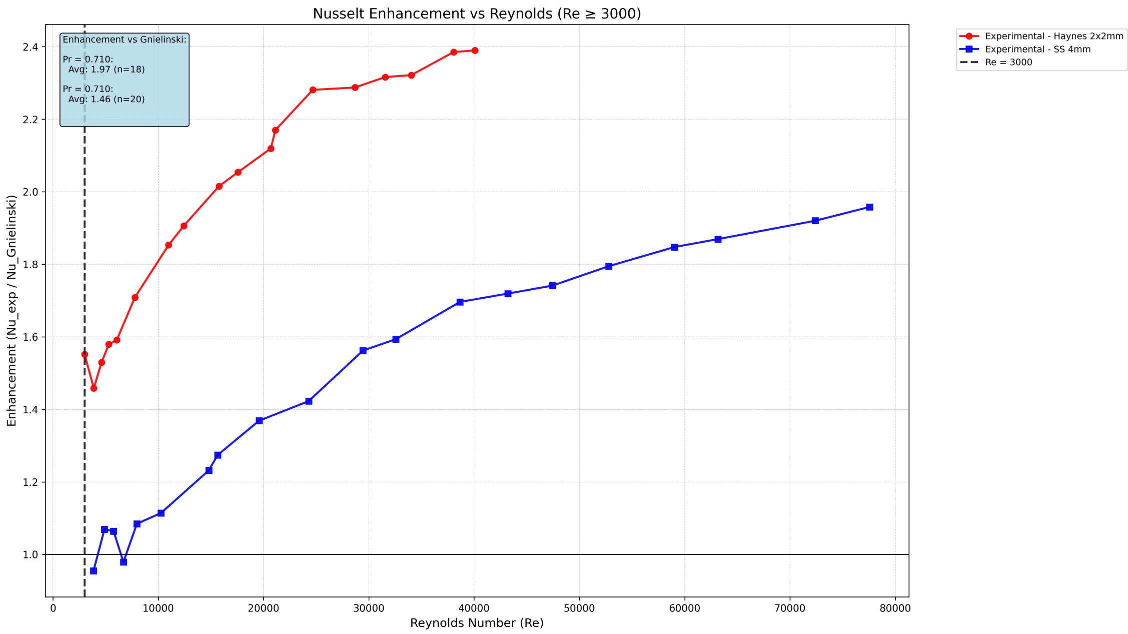

Figure 6.7: Nusselt-number enhancement for both stainless-steel printed test objects.

6.3 Local Heat Transfer Coefficient Distribution Analysis

One advantage of the new solver is its ability to resolve the local heat transfer behavior along the channel walls.

Both the smooth stainless-steel validation tube (Figure 6.8) and the 4 mm printed channel (Figure 6.9) exhibit a remarkably similar axial heat-transfer behavior, despite differences in geometry, manufacturing method, and surface roughness. The local heat-transfer coefficient (HTC) profiles of both geometries show the same three-stage trend, characteristic of internal convection in short channels with sharp-edged inlets:

- **A strong local HTC peak near the inlet**: At x/$D_h = 0$, both datasets display an elevated heat-transfer coefficient. This peak is attributed to the thermal-notch effect, amplified by the 90° sharp inlet edge in both test objects. As described in Section 2.1.7, a sudden contraction forces the flow into a vena-contracta-like acceleration, thinning the thermal boundary layer and generating HTC values substantially higher than those predicted by classical entrance-region theory. The presence of a strong notch peak in both geometries confirms that inlet geometry dominates the near-entry heat-transfer characteristics, even when surface roughness differs.
- **A region of developed behaviour**: After the initial peak, both the smooth tube and the 4 mm printed channel exhibit a region where the HTC varies more gradually with x/D_h, indicating that the flow approaches a thermally developing or quasi-fully-developed regime. In the smooth tube this region is flatter, consistent with minimal roughness and a circular hydraulic geometry. In the printed 4 mm square channel the HTC oscillations are slightly

larger, consistent with geometrical deviations and secondary flows typical of AM channels. Nonetheless, the overall behavior remains analogous: a stabilization of HTC after the inlet spike.

- **A decline in HTC at the last axial point**: In both datasets, the final measurement location shows a drop in HTC. This does not correspond to a physical decay in convective performance; instead, it is caused by outlet-side thermal losses at the copper–test-object interface, which reduce the effective wall-to-fluid temperature difference used by the inverse solver. The fact that the magnitude of this drop is similar in both geometries confirms that the phenomenon arises from boundary conditions external to the channel rather than from its internal structure.

Influence of sensor positioning at the outlet: A secondary contributor to the behaviour at the last segment is the steep temperature gradient near the outlet, discussed in detail in Section 4.2. Because the PT100 sensors have a sensing area of approximately 2 mm and must be positioned manually, a small axial misalignment during mounting (1–2 mm) may place the sensor in a region with a significantly different temperature. Since the solver enforces the measured wall temperature in each segment, any such displacement translates into an artificial adjustment of the reconstructed HTC. For this reason, the HTC at the first and last points must be interpreted with caution, while the central segments (Points 2–4) remain the most reliable and physically representative.

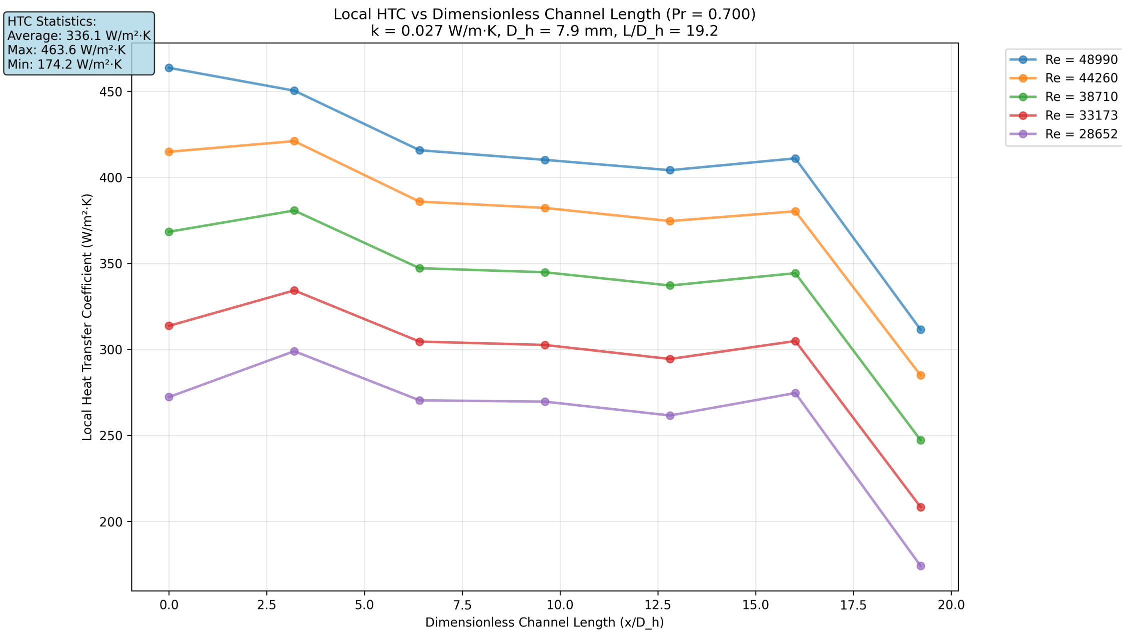

Figure 6.8: Local HTC distribution for the smooth test object.

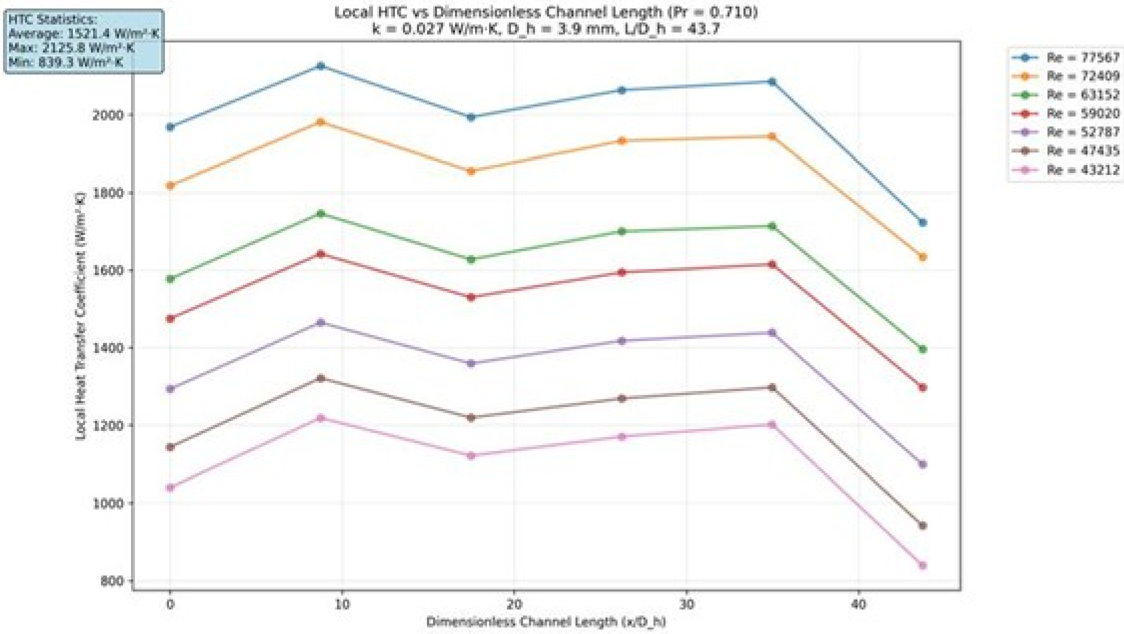

Figure 6.9: Local HTC distribution for the 4 mm circular channel.

Chapter 7

Error and Sensitivity Analysis

7.1 Error and Uncertainty Analysis

7.1.1 Darcy Friction Factor Total Error Analysis

To quantify the uncertainty of the Darcy friction factor, a theoretical uncertainty propagation approach was adopted using the Taylor series expansion method.

The friction factor is computed using Eq. 3.1, and the relative uncertainty ε_f is obtained by propagating the individual measurement uncertainties through:

$$\varepsilon_f = \sqrt{\left(\frac{\partial f}{\partial u}\varepsilon_u\right)^2 + \left(\frac{\partial f}{\partial L}\varepsilon_L\right)^2 + \left(\frac{\partial f}{\partial D_h}\varepsilon_{D_h}\right)^2 + \left(\frac{\partial f}{\partial \Delta P}\varepsilon_{\Delta P}\right)^2}. \tag{7.1}$$

The required partial derivatives are:

$$\frac{\partial f}{\partial u} = -\frac{4D_h\Delta P}{\rho u^3 L}, \tag{7.2}$$

$$\frac{\partial f}{\partial L} = -\frac{2D_h\Delta P}{\rho u^2 L^2}, \tag{7.3}$$

$$\frac{\partial f}{\partial D_h} = \frac{2\Delta P}{\rho u^2 L}, \tag{7.4}$$

$$\frac{\partial f}{\partial \Delta P} = \frac{2D_h}{\rho u^2 L}. \tag{7.5}$$

The instrument uncertainties used in this evaluation are listed in Table 4.1.

7.1.2 Nusselt Number Total Error Analysis

The uncertainty in the Nusselt number is obtained from standard propagation of uncertainties, treating h, D_h, and k as independent variables:

$$\sigma_{Nu}^2 = \left(\frac{\partial Nu}{\partial h}\sigma_h\right)^2 + \left(\frac{\partial Nu}{\partial D_h}\sigma_{D_h}\right)^2 + \left(\frac{\partial Nu}{\partial k}\sigma_k\right)^2. \tag{7.6}$$

Using the relations $\partial Nu/\partial h = D_h/k$, $\partial Nu/\partial D_h = h/k$, $\partial Nu/\partial k = -hD_h/k^2$, the uncertainty simplifies in relative form to:

$$\varepsilon_{Nu} = \sqrt{\varepsilon_h^2 + \varepsilon_{D_h}^2 + \varepsilon_k^2}. \tag{7.7}$$

The relative uncertainty in the heat-transfer coefficient is:

$$\varepsilon_h = \sqrt{\varepsilon_{\dot{m}}^2 + (w_f\,\varepsilon_{T_f})^2 + (w_w\,\varepsilon_{T_w})^2 + (w_c\,\varepsilon_{T_{cu}})^2}, \tag{7.8}$$

where the weighting factors $w_f, w_w, w_c \approx 0.5$ account for partial correlations between temperature measurements and the LMTD formulation used in the inverse solver.

Darcy Test: The average relative uncertainty obtained for the friction factor for the smooth TO was $\varepsilon_{f_{\text{Darcy}}} = 8.1\%$, with 75% of the data below 10%. The uncertainty is dominated by the hydraulic diameter estimation, which contributes approximately 90% of the total error.

The highest uncertainty $\varepsilon_{f_{\text{Darcy}}} = 21.2\%$ occurs at Re ≈ 2625, within the transition regime, where the pressure drop is moderate ($\Delta P \approx 696$ Pa). In the laminar region (Re < 2300), the uncertainty increases to an average of 11.3%, again driven primarily by diameter uncertainty—since pressure measurement uncertainty remains negligible ($< 0.1\%$) across all flow regimes.

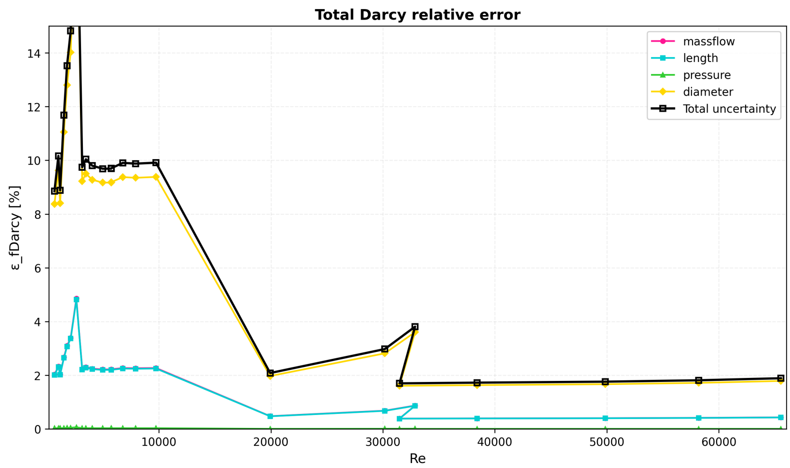

Figure 7.1: Relative uncertainty contributions to the Darcy friction factor across Reynolds number for the smooth TO.

Nusselt Test: The relative uncertainty of the Nusselt number for the smooth TO is $\varepsilon_{\text{Nusselt}} < 15\%$.

The dominant contribution arises from the outlet-air temperature measurement. Because the Nusselt number depends on the difference $T_{out} - T_{in}$, even small deviations in T_{out} at high Reynolds numbers change the inferred heat flux significantly. This motivated a dedicated sensitivity analysis on temperature-sensor placement, presented in Section 7.3.

Figure 7.2 shows a representative uncertainty distribution for a typical Nusselt test.

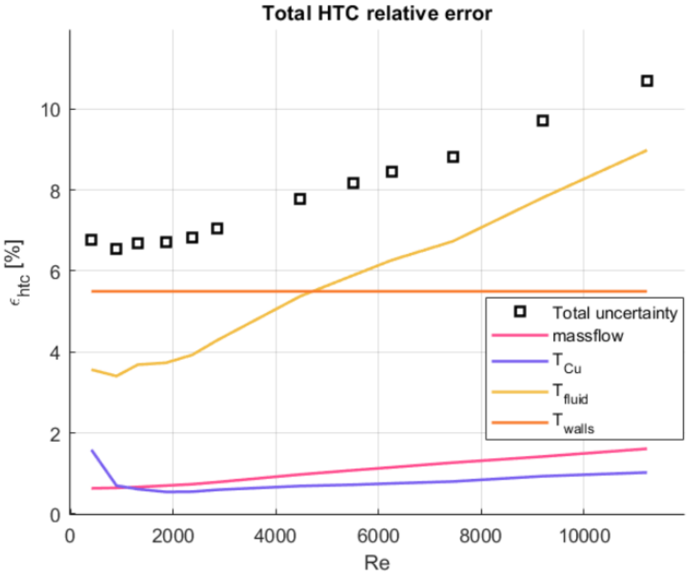

Figure 7.2: Example of uncertainty analysis for a Nusselt test.

7.2 Sensitivity Analysis Convergence Method

The comparison between the electrical heating and thermal input methods shows excellent consistency, as illustrated in Figure 7.3, with both following the same trend across the full Reynolds-number range and differing typically by only 5–10%. This small deviation derives from how uncertainties propagate through each calculation path: the electrical method derives heat input from the measured V×I and subtracts estimated losses, meaning any under-estimation of conduction, radiation, or contact-resistance effects slightly over-estimates the resulting Nusselt number; the thermal method instead relies directly on the measured outlet temperature, so uncertainties are mainly linked to temperature, mass-flow rate, and specific-heat measurements, without the possibility of artificially increasing the inferred heat transfer.

The close agreement between methods bellow <10% deviation validates both convergence approaches and confirms the robustness of the conjugate heat transfer model. The choice between methods becomes a matter of measurement confidence rather than fundamental methodology, with both providing reliable Nusselt number predictions.

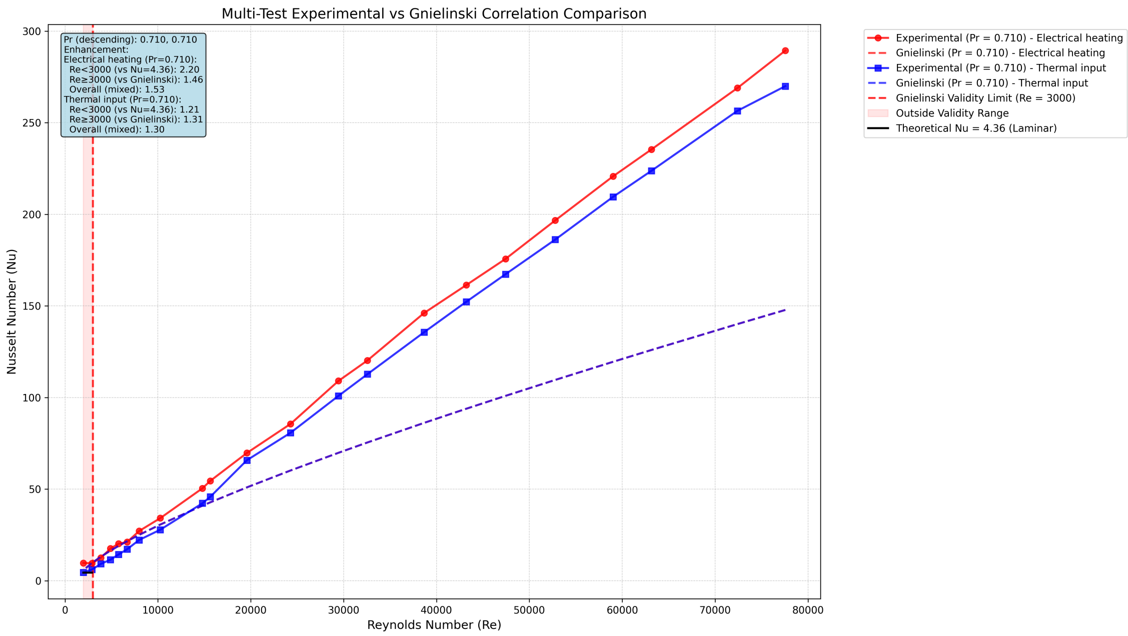

Figure 7.3: Nusselt results SS 4 mm.

7.3 Sensitivity Analysis Outlet Temperature Sensor Placement

To determine the optimal position for the PT100 sensor to measure the outlet temperature of the flow, a test was conducted while keeping all conditions constant, except for the position of the PT100. It was observed that even a slight change in position by just 1 cm resulted in significant temperature fluctuations. This phenomenon can be attributed to the temperature profile at the outlet not being fully developed and exhibiting turbulence due to the sudden expansion as the flow exits the temperature outlet (TO).

To achieve a more uniform temperature distribution, a flow mixer was employed, Figure 7.4. Tests were conducted under the same conditions, both with and without the flow mixer. The results of these tests are illustrated in the graph 7.5.

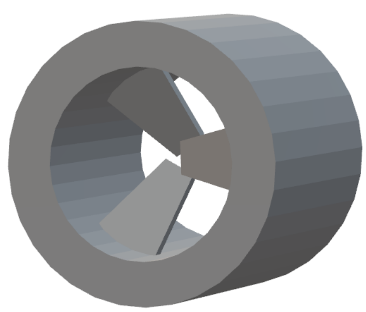

(a) CAD design of the flow mixer.

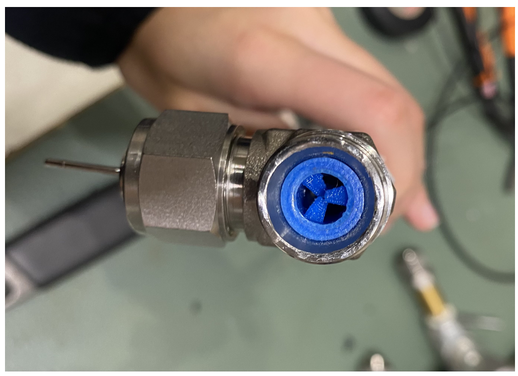

(b) Flow mixer in the rig.

Figure 7.4: Flow mixer design.

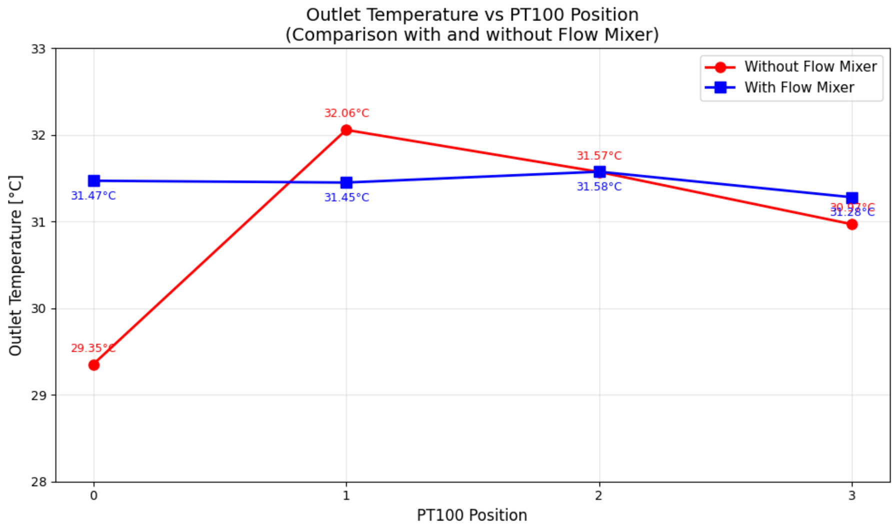

Figure 7.5: Joule heating rig with isulation.

The use of a flow mixer significantly enhances the uniformity of temperature, leading to improved heat retention. This results in a consistent outlet temperature across all measurement points, making the temperature less dependent on the position of the PT100 sensor. As shown in Table 7.1, the metrics indicate notable improvements when the flow mixer is utilized. It is important to note that all tests were conducted with the PT100 positioned 2 cm from the outlet, which recorded the highest temperature.

Table 7.1: Comparison of Metrics with and without Mixer

Metric	Without Mixer	With Mixer	Improvement
Average Temperature (°C)	30.988	31.444	+0.456°C
Standard Deviation (°C)	1.020	0.118	88.4% better
Temperature Range (°C)	2.705	0.295	89.1% better
Coefficient of Variation	3.29%	0.38%	88.4% better

7.4 Sensitivity Analysis HTC contact

A sensitivity analysis was performed to evaluate the robustness of the calculated Nusselt numbers in response to fluctuations in this boundary condition. The inverse problem methodology was applied for four distinct values of the contact heat transfer coefficient: 6000, 8000, 10000, and 12000 W/m²K. This range includes the usual values found in the literature for metal-to-metal contacts with moderate clamping pressure [45], encompassing a 100% variation around the nominal value.

Figure 7.6 presents the resulting Nusselt number versus Reynolds number relationships for all four contact HTC values. The curves are almost the same across the whole range of Reynolds numbers, which means that this boundary condition parameter has extremely low sensitivity.

Quantitative analysis reveals that doubling the contact HTC from 6000 to 12000 W/m²K produces maximum deviations in Nusselt number of only 1.15% at the lowest Reynolds number (Re $\approx$ 3000), 0.98% at intermediate Reynolds numbers (Re $\approx$ 15800), and 0.80% at the highest Reynolds number (Re $\approx$ 40000). The mean variation across all test points is merely 0.94%, which is well below the typical measurement uncertainty associated with experimental heat transfer characterization.

The insensitivity to contact HTC also validates the use of a nominal value in the simulations without requiring detailed contact mechanics characterization, simplifying the inverse problem methodology while maintaining accuracy.

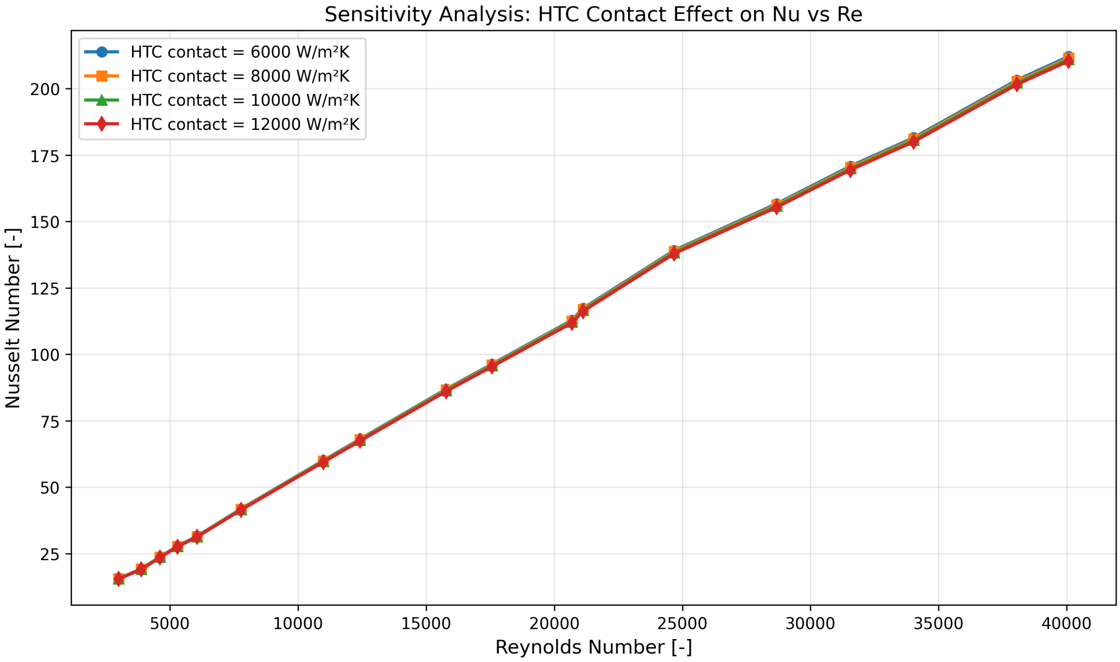

Figure 7.6: Sensitivity analysis of Nusselt number to contact heat transfer coefficient variations.

7.5 Sensitivity Analysis HTC fittings

The heat transfer coefficient at the inlet and outlet fittings represents another boundary condition uncertainty in the simulations. To assess its influence on the determined Nusselt numbers, the inverse problem methodology was executed for two different HTC fittings values: 200 and 400 W/m²K.

Figure 7.7 presents the sensitivity analysis for the SS 4 mm test section. The results demonstrate negligible sensitivity to the fittings boundary condition, with a mean difference of only 0.13% between the two HTC values and a maximum deviation of 4.5%. The determined Nusselt numbers are essentially identical for both cases, confirming that the heat transfer characterization is robust and insensitive to uncertainties in this boundary condition parameter.

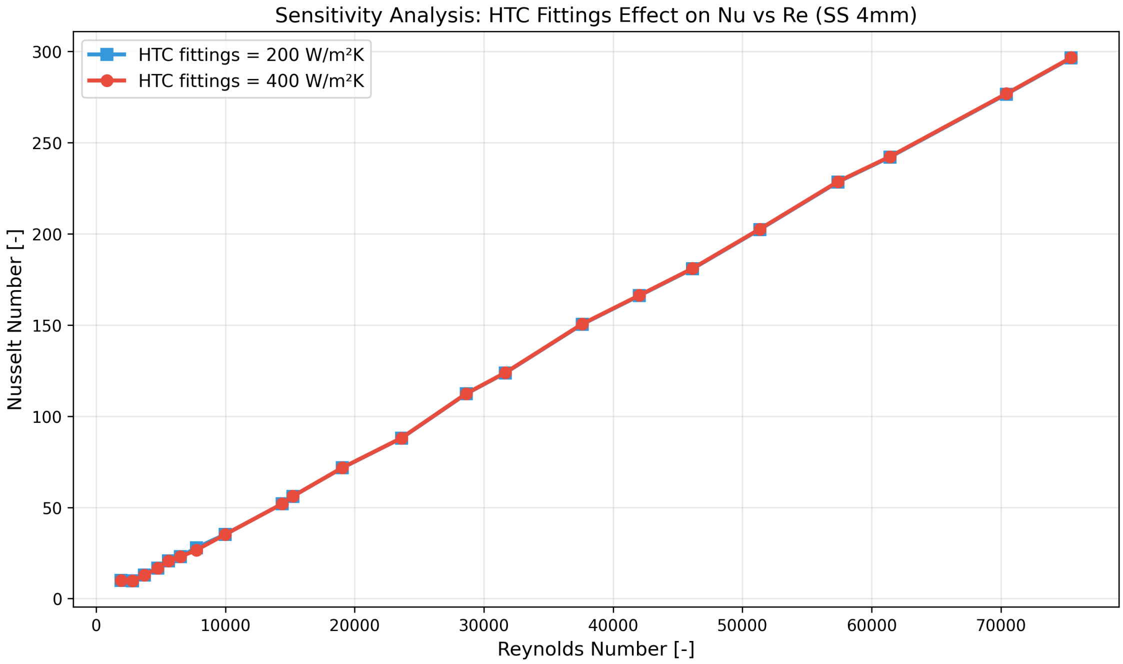

Figure 7.7: Sensitivity analysis of Nusselt number to fittings heat transfer coefficient variations.

7.6 Sensitivity Analysis Soldered versus Machined Solution

To assess the influence of the test-object–copper interface on the determined heat-transfer coefficients, two assembly configurations were compared. In the *machined solution*, the Haynes 282 test object is mechanically clamped between the copper bars after its outer surface has been machined. In the *soldered solution*, the test object is permanently bonded to the copper using a silver-based solder, and its outer surface is left unmachined. This comparison isolates the effect of the interfacial thermal resistance between the copper and the TO.

Figure 7.8 presents the Nusselt number as a function of Reynolds number for both configurations. The results exhibit excellent agreement, with an average difference of only 2.68% over the overlapping Reynolds-number range (Re $\approx$ 7000–40000) and a standard deviation of 3.59%. This close correspondence indicates that the thermal contact resistance at the interface has negligible influence on the extracted heat-transfer characteristics.

Consequently, the inverse heat-transfer methodology is shown to be robust with respect to the assembly approach, and the use of the machined solution is fully justified from both a practical and thermal-performance perspective.

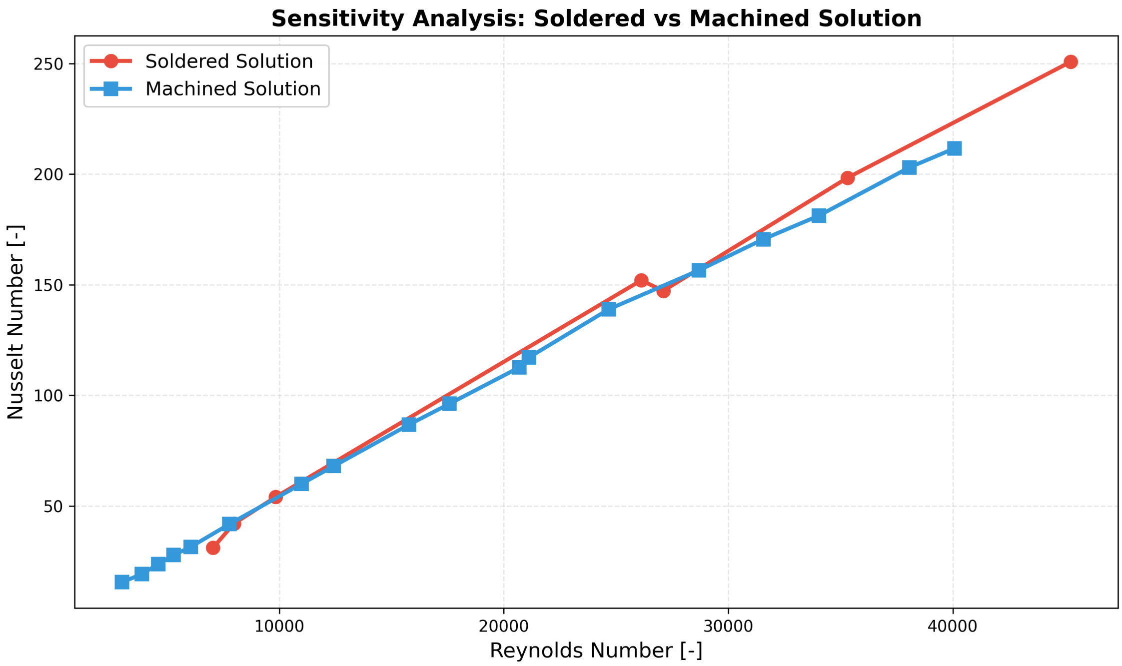

Figure 7.8: Comparison of soldered and machined configurations: Nusselt vs. Reynolds.

Chapter 8

Conclusions and Future Works

This dissertation presented the development, validation, and application of an improved evaluation methodology for the quasi-Steady State Heat Transfer (qSSHT) rig, enabling accurate thermal and hydraulic characterization of additively manufactured (AM) mini-channels using air as the working fluid. The methodological upgrades introduced throughout the work—spanning the experimental procedure, instrumentation, and numerical post-processing—allowed the qSSHT rig to overcome several limitations of previous approaches and to deliver reliable measurements of both the Nusselt number and the Darcy friction factor.

Two AM stainless sterl test objects were experimentally investigated: a 2×2 mm square Haynes channel and a 4 mm circular channel, both exhibiting the characteristic surface roughness inherent to laser powder-bed fusion manufacturing. The results clearly demonstrated the influence of AM-induced roughness on pressure-loss behaviour and heat-transfer performance. The Haynes channel, with a relative roughness approximately twice that of the 4 mm tube, showed significantly higher friction factors than predicted by smooth-wall correlations and presented an average Nusselt enhancement close to a factor of two for Reynolds numbers above 3000. The stainless-steel tube displayed more moderate increases, consistent with its lower roughness level. These findings provide experimental evidence of the coupled hydraulic and thermal influence of AM roughness, which remains insufficiently documented in the current literature.

A key contribution of this work is the implementation of a refined inverse heat-transfer solver capable of resolving local HTC variations along the channel length. For the first time in this rig, spatially varying heat-transfer distributions were obtained with high fidelity, capturing entrance effects, developing-flow behaviour, and roughness-induced non-uniformities. The close agreement (typically within 5–10%) between the electrical-heating evaluation method and the thermal-input method further confirmed the robustness of the updated methodology and its suitability for high-precision heat-transfer assessment.

Overall, the improved qSSHT methodology demonstrated the ability to produce accurate, repeatable, and physically consistent measurements of friction factor and Nusselt number for AM cooling channels. The results establish a solid experimental basis for correlating heat-transfer performance and pressure losses with AM-induced roughness, providing valuable guidance for the design and optimization of internal cooling systems in industrial applications such as turbine-blade cooling.

8.1 Future works

1. **Expand the experimental database.** Testing additional AM channels with different geometries, dimensions, and materials would allow the development of more general heat-transfer and friction correlations applicable to a wider range of turbine-cooling components.

2. **Characterize roughness more comprehensively.** A comprehensive characterization of the internal surface roughness, based on profilometry or other suitable measurement techniques, would improve the ability to correlate roughness parameters with the resulting heat-transfer performance.

3. **Improve sensor placement and measurement accuracy.** Optimizing the positioning and number of wall-temperature sensors could reduce the uncertainty associated with outlet-temperature measurements, currently the dominant source of error in the Nusselt evaluation.

4. **Develop empirical design correlations.** Using the expanded dataset, empirical correlations for Nusselt number and Darcy friction factor tailored to AM surfaces could be proposed for industrial use, supporting predictive tools for turbine-blade internal cooling.

References

[1] Hannah Ritchie, Pablo Rosado, and Max Roser. *Energy production and consumption*. Our World in Data. Accessed on: 2025-07-20. 2020.

[2] T. Xu et al. "The implementation limitation of variable renewable energies and its impacts on the public power grid". In: *Energy* 239 (2021), p. 121992. DOI: 10.1016/j.energy.2021.121992. URL: https://www.sciencedirect.com/science/article/pii/S0360544221022404.

[3] Energy Institute. *Statistical Review of World Energy 2024*. Technical Report. Second edition under EI custodianship. London, UK: Energy Institute, Nov. 2024. URL: https://www.energyinst.org/statistical-review.

[4] Siemens Energy. *SGT-750 gas turbines – Flexible, reliable with best-in-class performance*. https://www.siemens-energy.com/global/en/home/products-services/product/sgt-750.html#/. Accessed: 2025-11-26.

[5] H. I. H. Saravanamuttoo. *Gas Turbine Theory*. Pearson Education Limited, 2001.

[6] Changhe Du et al. "Rotational influences on aerodynamic and heat transfer behavior of gas turbine blade vortex cooling with bleed holes". In: *Applied Thermal Engineering* 121 (2017), pp. 302–313.

[7] P. M. Ligrani, M. M. Oliveira, and T. Blaskovich. "Comparison of heat transfer augmentation techniques". In: *AIAA Journal* 41.3 (Mar. 2003), pp. 337–362.

[8] C. K. Stimpson et al. "Scaling roughness effects on pressure loss and heat transfer of additively manufactured channels". In: *Journal of Turbomachinery* 139.2 (Feb. 2017), p. 10.

[9] S. A. Weaver, M. D. Barringer, and K. A. Thole. "Micro channels with manufacturing roughness levels". In: *Journal of Turbomachinery* 133.4 (Oct. 2011), p. 10.

[10] J.C. Han. "Recent studies in Turbine Blade Cooling". In: *International Journal of Rotating Machinery* 10.6 (2004), pp. 443–457.

[11] C. K. Stimpson et al. "Roughness effects on flow and heat transfer for additively manufactured channels". In: *Journal of Turbomachinery* 138.5 (2016), p. 10. ISSN: 0889-504X. DOI: 10.1115/1.4032167.

[12] Yunus A. Cengel and John M. Cimbala. *Fluid Mechanics: Fundamentals and Applications*. 3rd ed. McGraw-Hill, 2014.

[13] A. L. Braslow. *A Review of Factors Affecting Boundary-Layer Transition*. Tech. Rep. Washington, D.C.: NASA Technical Note (TN), 1966.

[14] Wade W. Huebsch Bruce R. Munson Theodore H. Okiishi and Alric P. Rothmayer. *Fundamentals of Fluid Mechanics*. 8th ed. Wiley & Sons, Inc., 2018.

[15] David Weyburne. *Aspects of Boundary Layer Theory*. 3rd ed. BasicScience, 2025. ISBN: 979-8-218-40650-9.

[16] Hermann Schlichting and Klaus Gersten. *Boundary-Layer Theory*. 9th. Berlin: Springer, 2017.

[17] John D. Anderson Jr. *Fundamentals of Aerodynamics*. 5th ed. McGraw-Hill, 2010.

[18] Frank M. White. *Fluid Mechanics*. 6th. New York: McGraw-Hill, 2006.

[19] Theodore L. Bergman and Asrienne S. Lavine. *Fundamentals of Heat and Mass Transfer*. Eighth. John Wiley & Sons, Inc, 2011. ISBN: 978-1-119-32042-5.

[20] Satish G. Kandlikar. "High flux heat removal in microchannels and mini-channels". In: *Heat Transfer Engineering* 26.8 (2005), pp. 5–14.

[21] Tri D. Ngo et al. "Additive manufacturing (3D printing): A review of materials, methods, applications and challenges". In: *Composites Part B: Engineering* 143 (2018), pp. 172–196. DOI: 10.1016/j.compositesb.2018.02.012.

[22] Yunus A. Cengel. *Heat Transfer: A Practical Approach*. 2nd. New York: McGraw-Hill, 2002.

[23] I. E. Idel'chik. *Handbook of Hydraulic Resistance: Coefficients of Local Resistance and of Friction*. Israel Program for Scientific Translations, 1966. URL: https://www.nrc.gov/docs/ML1220/ML12209A041.pdf.

[24] G. O. Brown. "The History of the Darcy–Weisbach Equation for Pipe Flow Resistance". In: *Environmental and Water Resources History* (Oct. 2002).

[25] J. Nikuradse. *Laws of Flow in Rough Pipes (Strömungsgesetze in Rauhen Rohren)*. Tech. rep. Washington, D.C.: NACA Technical Memorandum 1292, Nov. 1950.

[26] L. F. Moody and N. J. Princeton. "Friction Factors for Pipe Flow". In: *Transactions of the ASME* 66 (Nov. 1944), pp. 671–684.

[27] A. F. Mills. "Experimental investigation of turbulent heat transfer in the entrance region of circular conduit". In: *Journal of Mechanical Engineering Science* 4.1 (Mar. 1962), pp. 63–77. DOI: 10.1243/JMES_JOUR_1962_004_010_02.

[28] W. Sutherland. "LII. The viscosity of gases and molecular force". In: *The London, Edinburgh, and Dublin Philosophical Magazine and Journal of Science* 36.223 (1893), pp. 507–531.

[29] A. Eucken. "Allgemeine Gesetzmäßigkeiten für das Wärmeleitvermögen verschiedener Stoffarten und Aggregatzustände". In: *Physikalische Zeitschrift* 14 (1913), pp. 324–332.

[30] Timothy J. Horn and Ola L. A. Harrysson. "Overview of Current Additive Manufacturing Technologies and Selected Applications". In: *Science Progress* 95.3 (2012), pp. 255–282.

[31] Abbas Razavykia et al. "An Overview of Additive Manufacturing Technologies—A Review to Technical Synthesis in Numerical Study of Selective Laser Melting". In: *Materials* 13.17 (2020), p. 3895. DOI: 10.3390/ma13173895.

[32] C. Y. Yap et al. "Review of selective laser melting: Materials and applications". In: *Applied Physics Reviews* 2 (Dec. 2015).

[33] Sara Sendino et al. "Surface Roughness Dependant Factors in Metal Powder Bed Fusion Processes". In: cit. on p. 11.

[34] S. M. H. Hojjatzadeh et al. "Spatter formation and dynamics during laser powder bed fusion of metals". In: *Additive Manufacturing* 47 (2021), p. 102279. DOI: 10.1016/j.addma.2021.102279.

[35] *ISO 4287: Geometrical Product Specifications (GPS) – Surface texture: Profile method – Terms, definitions and surface texture parameters*. Reconfirmed in 2009. Geneva, Switzerland: International Organization for Standardization, 1997.

[36] A. Townsend et al. "Surface Texture Metrology for Metal Additive Manufacturing: A Review". In: *Precision Engineering – Journal of the International Societies for Precision Engineering and Nanotechnology* 46 (2016), pp. 34–47. ISSN: 0141-6359. DOI: 10.1016/j.precisioneng.2016.06.001.

[37] D. J. Whitehouse. *Surfaces and Their Measurement*. 1st. Hermes Penton Science, 2002. ISBN: 1-9039-9601-5.

[38] Cora Venturi. "Investigation of Thermal Performance of AM Channels and the Influence of the Printing Angle". Master's Thesis, Corso di Laurea Magistrale in Ingegneria Aerospaziale. MA thesis. Turin, Italy: Politecnico di Torino, Dec. 2023.

[39] SimScale. *What Is Joule Heating (Joule Effect)?* Last updated: November 20, 2023. 2023. URL: https://www.simscale.com/docs/simwiki/heat-transfer-thermal-analysis/what-is-joule-heating/.

[40] C. Ribeiro. "Investigation of the Effect of Additively Manufactured Induced Roughness on the Heat Transfer and Pressure Loss with the Quasi Steady State Heat Transfer Method". MA thesis. Universidade do Porto, 2024.

[41] H. W. Coleman and W. G. Steele. *Experimentation, Validation, and Uncertainty Analysis for Engineers*. John Wiley & Sons, 2018.

[42] Jacob Sandahl. "Experimental and Computational Analysis of Heat and Momentum Transfer in Rough Additive Manufactured Internal Cooling Channels". Master's thesis. Linköping, Sweden: Department of Management, Engineering, Division of Applied Thermodynamics, and Fluid Mechanics, 2025.

[43] Shruti Aaher. "Experimental Investigation on Forced Convective Heat Transfer in Additively Manufactured Cooling Channels". Master's Thesis, Sustainable Energy Engineering. MA thesis. Stockholm, Sweden: Kungliga Tekniska Hogskolan, Nov. 2025.

[44] Aaron Brugnera. "Experimental investigation of heat transfer in additive manufactured channels with different Prandtl". MA thesis. Politecnico di Torino, 2024.

[45] L. S. Fletcher. "Heat Transfer Between Surfaces in Contact: Thermal Contact Conductance Correlations for Metals". In: *Journal of Heat Transfer* 93.3 (1971), pp. 321–327.

Appendix A

Individual results

A.1 Results for Haynes 2x2mm

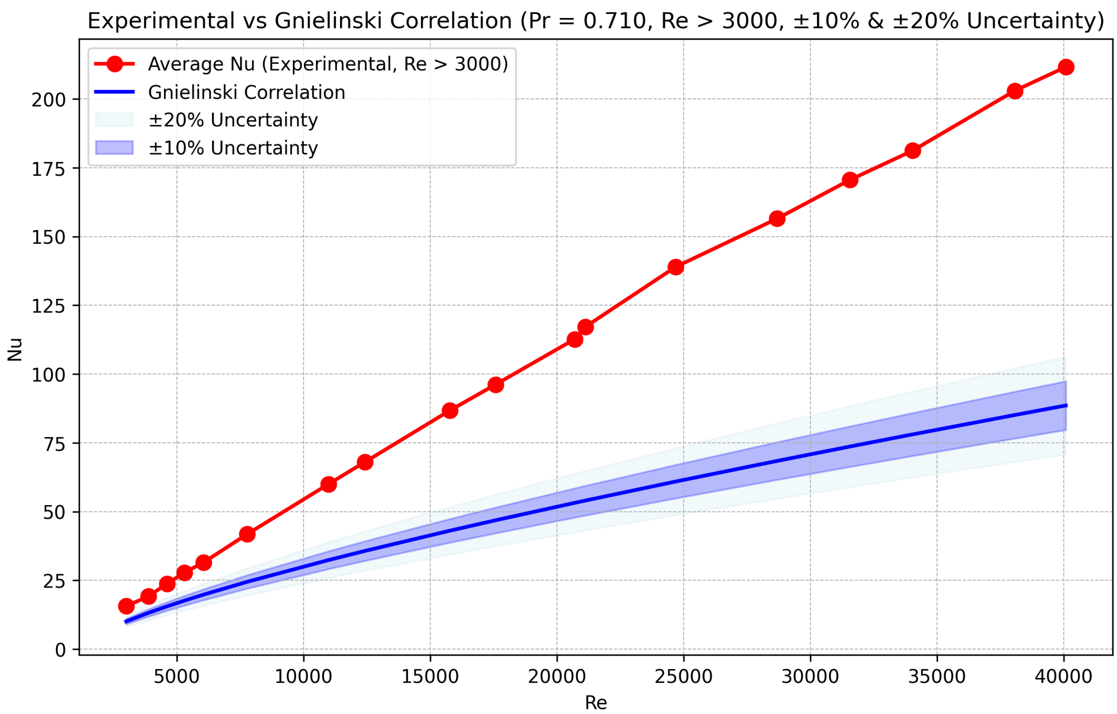

Figure A.1: Experimental vs. Gnielinski Nusselt number results Haynes 2x2mm.

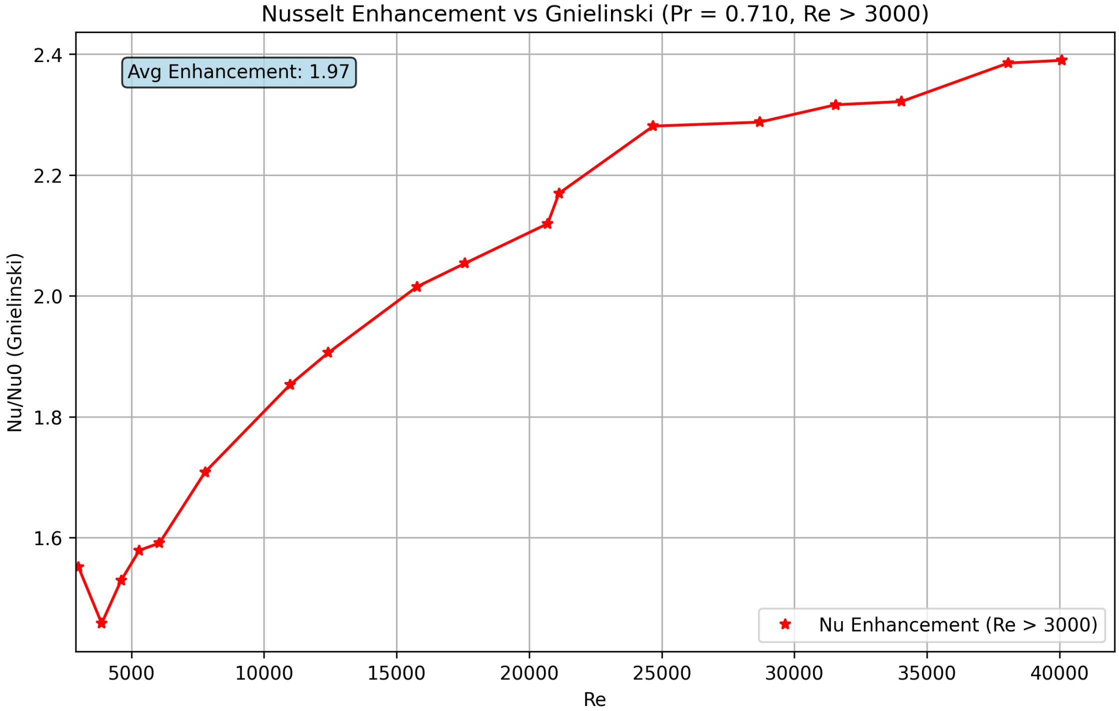

Figure A.2: Nusselt Enhancement Haynes 2x2mm.

A.2 Results for SS 4mm

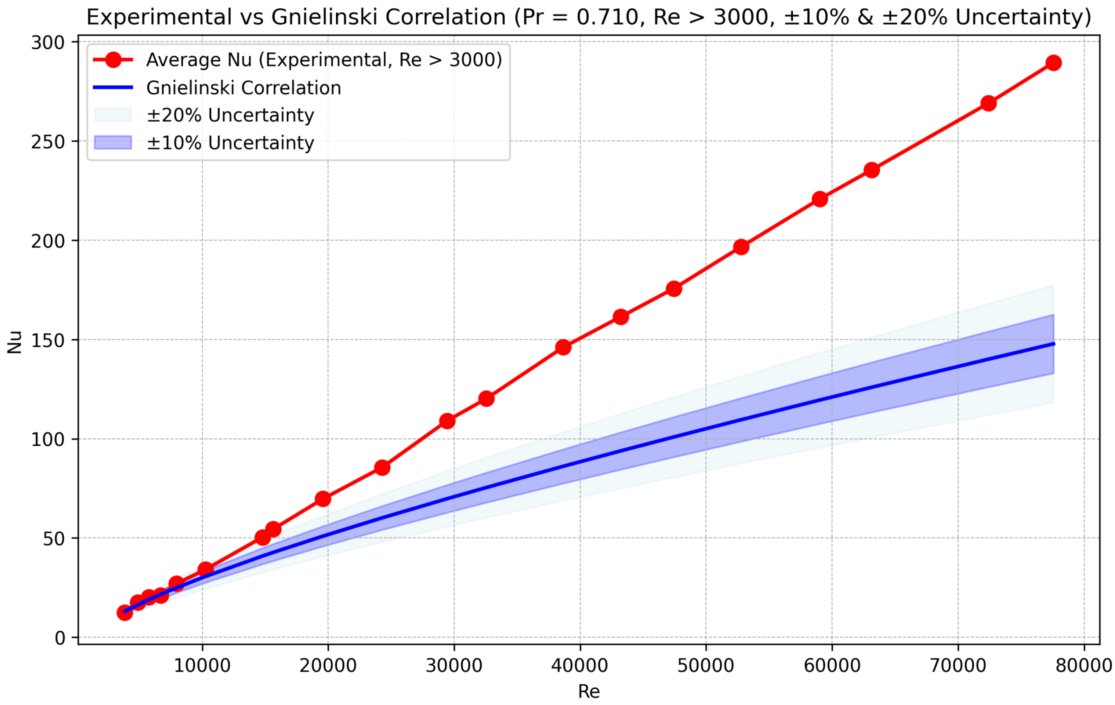

Figure A.3: Experimental vs. Gnielinski Nusselt number results.

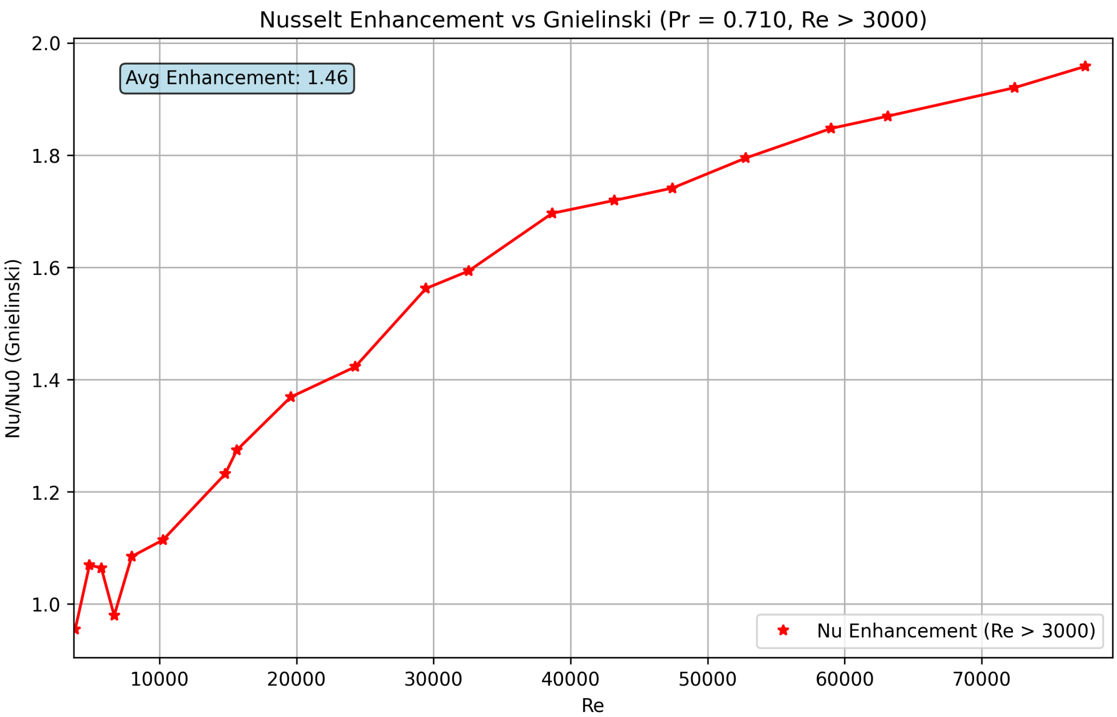

Figure A.4: Experimental vs. Gnielinski Nusselt number results.